Characterizing Dust Storms and Modeling Diffusion in Viscous Atmospheric Aerosol Particles

by

Ali Moridnejad

A THESIS SUBMITTED IN PARTIAL FULFILLMENT
OF THE REQUIREMENTS FOR THE DEGREE OF

Doctor of Philosophy

in

THE FACULTY OF SCIENCE
(Department of Atmospheric and Oceanic Sciences)

McGill University
(Montreal)

August 2017

Abstract

This thesis includes separate research studies on atmospheric dust particles and viscous aerosol particles. In Chapters 2 and 3, the major source points of atmospheric dust particles in the Middle East are studied. We analyze daily images from a moderate resolution imaging spectroradiometer (MODIS) sensor as well as deep blue aerosol products to select dust events occurred between 2000-2012. Then, source point identification is performed on the images of dust events using an improved version of Middle East dust index (MEDI). Later, we classify the identified sources based on their intensity and frequency to better understand the contribution of each dust source point in generating dust storms. The findings show that Iraq and Syria have the highest active dust sites among all studied countries in the region. Furthermore, we investigate whether the observed intense and frequent dust activities are linked to desertification occurred over the past three decades. Analyzing Landsat TM images (1984 and 2012), it is found that 39% of identified sources in Iraq and its surrounding areas are located in newly desertified regions. Finally, these results are compared with other studies and the implication of the findings are discussed.

In Chapter 4, we describe a mathematical formulation of the water exchange diffusion problem and present analytical solutions for this problem for a spherical particle. Two different boundary conditions, constant and equilibrium concentration on the particle surface, are used to obtain solutions to the water exchange diffusion problem. Then, the effect of these boundary conditions is investigated in the context of isotope tracer experiments. Using dimensionless analysis, it is shown that the predicted sorption with fixed concentration on boundary is always greater than or equal to the model with the equilibrium boundary condition. These findings also suggest there are many physically relevant cases where the difference between these two solutions is inconsequential. We further explore these results using three physical examples of binary solution droplets: aqueous sucrose, aqueous citric acid, and aqueous shikimic acid droplets. Using the two derived analytical models, we study the water exchange lifetime. It is observed that the type of boundary condition becomes very significant when RH is very high in all cases. We conclude by discussing the observed discrepancy in the reported diffusion coefficient between isotopic water exchange and water sorption experiments.

In Chapter 5, the nonlinear diffusion of water in highly viscous and glassy aerosol particles is modeled and we discuss tracking the associated diffusion front. This tracking is accomplished by analyzing the optical behavior of spherical particle exposed to electromagnetic radiation during the diffusion process. Currently, the numerical multilayer Mie models require a concentration profile as an input. Obtaining this profile requires solving the nonlinear diffusion problem, which is very time consuming. We present an analytical model to simulate the position of morphology dependent resonances (MDRs) of a core-shell aerosol particle. Then, we compare the core-shell model with the previously developed multilayer Mie model. Results demonstrate that the derived characteristic equation can accurately calculate the positions of MDRs in a much faster way compared to the existing multilayer model. From simulation data, the most sensitive region to the gradient of refractive index is found to be very close to the particle surface. This sensitivity becomes insignificant at low relative humidities and limits the application of this work. Our model eliminates the complexity associated with using traditional numerical calculations based on water transport models to analyze single particle measurements.

Résumé

Cette thèse comprend des études de recherche distinctes sur les particules de poussière atmosphérique et les particules d'aérosol visqueuses. Dans les chapitres 2 et 3, les principales sources de particules de poussière atmosphérique au Moyen-Orient sont étudiées. Nous analysons les images quotidiennes du capteur moderate resolution imaging spectroradiometer (MODIS) ainsi que des produits aérosols de Deep Blue pour sélectionner les événements de poussière survenus entre 2000 et 2012. Ensuite, l'identification de la source est effectuée sur les images des événements de poussière en utilisant une version améliorée de l'indice de poussière du Moyen-Orient (MEDI). Par la suite, nous classons les sources identifiées en fonction de leur intensité et de leur fréquence pour mieux comprendre la contribution de chaque source dans la génération des tempêtes de poussière. Les résultats montrent que l'Irak et la Syrie ont les sites de poussière très actifs les plus élevés parmi tous les pays étudiés dans la région. En outre, on étudie si les événements de poussière intenses et fréquentes observées sont liés à la désertification au cours des trois dernières décennies. En analysant les images Landsat TM (1984 et 2012), on constate que 39% des sources identifiées en Irak et dans ses régions environnantes se trouvent dans des régions nouvellement désertes. Enfin, ces résultats sont comparés à d'autres études et l'implication des résultats est discutée.

Dans le chapitre 4, nous décrivons une formulation mathématique du problème de diffusion de l'échange d'eau et présentons des solutions analytiques pour ce problème dans le cas d'une particule sphérique. Deux conditions de limites différentes, 1) concentration à constante et 2) concentration à l'équilibrée à la surface de la particule, sont utilisées pour obtenir des solutions au problème de diffusion de l'échange d'eau. Ensuite, l'effet de ces conditions aux limites est étudié dans le cadre d'expériences de traceurs isotopiques. En utilisant une analyse sans

dimension, il est démontré que la sorption prédite avec une concentration fixée sur la surface est toujours supérieure ou égale au modèle avec la condition de limite d'équilibre. Ces résultats suggèrent également qu'il existe de nombreux cas physiquement pertinents où la différence entre ces deux solutions est sans conséquence. Nous explorons davantage ces résultats en utilisant trois exemples physiques de gouttelettes de solution binaire: sucrose aqueux, acide citrique aqueux et gouttelettes d'acide shikimique aqueux. En utilisant les deux modèles analytiques dérivés, nous étudions la durée de vie de l'échange d'eau. On constate que le type de condition limite devient très significatif lorsque l'humidité relative est très élevé dans tous les cas. Nous concluons en discutant le décalage observé dans le coefficient de diffusion signalé entre les expériences isotopiques d'échange d'eau et de sorption d'eau.

Dans le chapitre 5, la diffusion non linéaire de l'eau dans les particules d'aérosol très visqueuses et vitreuses est modélisée et nous discutons du déplacement du front de diffusion associé. Ce suivi est réalisé en analysant le comportement optique de la particule sphérique exposée au rayonnement électromagnétique pendant le processus de diffusion. Présentement, les modèles Mie multicouches numériques nécessitent un profil de concentration en tant qu'entrée. L'obtention de ce profil a besoin de la résolution du problème de diffusion non linéaire, qui prend beaucoup de temps. Nous présentons un modèle analytique pour simuler la position des résonances dépendantes de la morphologie (MDR) d'une particule d'aérosol à noyau-coquille. Ensuite, nous comparons le modèle noyau-coquille avec le modèle Mie multicouches précédemment développé. Les résultats démontrent que l'équation caractéristique dérivée peut calculer avec précision les positions des MDR de manière beaucoup plus rapide par rapport au modèle multicouche existant. À partir des données de simulation, la région la plus sensible au gradient de l'indice de réfraction se trouve très près de la surface de la particule. Cette sensibilité devient insignifiante à de faibles valeurs de humidité relative et limite l'application de ce travail. Notre modèle élimine la complexité associée à l'utilisation de calculs numériques traditionnels basés sur des modèles de transport d'eau à analyser les mesures de particule unique.

Contribution of Authors

Chapter 2 was published as: Moridnejad, A.; Karimi, N.; Ariya, P. A. A new inventory for middle east dust source points. *Springer, Environ. Monit. Assess.* **2015**, *187*, 582. The research program for this chapter was designed by A. Moridnejad, N. Karimi, and P. A. Ariya. Data acquisition, interpretation and modeling were performed by A. Moridnejad and N. Karimi. Preparation of the manuscript was performed by all three authors.

Chapter 3 was published as: Moridnejad, A.; Karimi, N.; Ariya, P. A. Newly desertified regions in Iraq and its surrounding areas: Significant novel sources of global dust particles. *Elsevier, J. Arid. Environ.*, **2015** *116*, 1-10. The research program for this chapter was designed by A. Moridnejad, N. Karimi, and P. A. Ariya. Data acquisition, interpretation and modeling were performed by A. Moridnejad and N. Karimi. Preparation of the manuscript was performed by all three authors.

Chapter 4 was published as: Moridnejad, A.; Preston, T. C. Models of isotopic water diffusion in spherical aerosol particles. *J. Phys. Chem. A* **2016**, *120*, 9759-9766. The research program for this chapter was designed by A. Moridnejad and T. C. Preston. Modeling, derivation of equations, interpretation of data, and preparation of the manuscript were performed by A. Moridnejad and T. C. Preston.

Chapters 5 has been submitted for publication as: Moridnejad, A.; Preston, T. C.; Krieger, U. K. Tracking water sorption in glassy aerosol particles using morphology-dependent resonances. *ACS,J. Phys. Chem. A* **2017**. The research program for this chapter was designed by A. Moridnejad, T. C. Preston, and U. K. Krieger. Data acquisition, derivation of equations, modeling, and interpretation of data were performed by A. Moridnejad and T. C. Preston. Preparation of the manuscript was performed by all three authors.

Statement of Originality

The following elements of the thesis show original scholarship and represent distinct contributions to knowledge:

- (1) Presenting significant novel atmospheric dust source points in the Middle East region using a newly developed Middle East dust index (MEDI), (2) identifying sensitive source points in terms of intensity and frequency, (3) presenting a new high resolution desertification map for Iraq and surrounding areas. We believe that the results are indeed of interest to the large community of geophysical scientists since not much is known about new dust source points and desertification patterns in the Middle East region and its local, regional and global impacts, whereby data is quite scarce, and unfortunately communication and scientific and environmental cooperation is not a tradition. This data is important in multiple disciplines of research as dust aerosols affect air quality, extreme weather, hydrological cycle, radiation, cloud physics and Earths biogeochemical cycles.
- Developing mathematical-physical models for the isotopic water diffusion in spherical aerosol particles. For the first time, an analytical solution for the isotopic diffusion involving equilibrium boundary condition on the particle surface is presented. We found that the choice of boundary condition can significantly affect the retrieved diffusion coefficient using isotopic water exchange experiment. These finding greatly contribute in better understanding the discrepancies in measured diffusion coefficient of secondary organic particles (SOA) reported by atmospheric aerosol community.
- Developing an optical model to quantify the radiation scattering by viscous particles that exhibit core-shell morphology. In this model, we present, for the first time, a full ana-

lytical expression that describes the resonance condition for a core-shell particle. This model eliminates the complexity associated with the current numerical multi-layer models. Furthermore, using measured optical spectra, the model performs well in predicting the particle size and composition if the refractive index profile can be accurately described by a step-function. The use of morphology dependent resonances (MDRs) in this model greatly contributes in understanding the non-linearity of water diffusion in high viscosity and glassy aerosols. The findings of this study provide an exciting new way for researchers, particularly who measure the light scattering by viscous particles over a wide range of spectrum, to identify the position of the diffusion front during sorption experiment.

Table of Contents

List of Tables

List of Figures

Acronyms

AI	Aerosol Index
AOD/AOT	Aerosol Optical Depth/Thickness
BTD	Brightness Temperature Difference
CCN	Cloud Condensation Nuclei
COAMPS	Coupled Ocean/Atmosphere Mesoscale Prediction System
DB	Deep Blue
DOD	Dust Optical Depth
EDB	Electrodynamic Balance
EOS	Earth Observing System
ERF	Effective Radiative Forcing
GHG	Greenhouse Gas
HTDMA	Hygroscopicity Tandem Differential Mobility Analyzer
HYSPLIT	HYbrid Single-Particle Lagrangian Integrated Trajectory
IDDI	Infrared Difference Dust Index
IN	Ice Nucleation
IPPC	Intergovernmental Panel on Climate Change
IR	InfraRed
M-DB2	MODIS Deep Blue level 2
MDR	Morphology Dependent Resonace
MEDI	Middle East Dust Index

MODIS	Moderate Resolution Imaging Spectro-radiometer
MSG	Meteosat Second Generation
NCAR	National Center for Atmospheric Research
NCEP	Centers for Environmental Prediction
NDDI	Normalized Difference Dust Index
OMI	Ozone Monitoring Instrument
RH	Relative Humidity
RI	Refractive Index
SEVIRI	Spinning Enhanced Visible and InfraRed Imager
SOA	Secondary Organic Aerosol
TE	Transverse Electric
TIR	Thermal Infrared
TM	Transverse Magnetic
TOMS	Total Ozone Mapping Spectrometer
UV	Ultraviolet
VFT	Vogel Fulcher Tammann
VIS	Visible
WGM	Whispering Gallery Mode

Acknowledgments

I would like to thank Professor Parisa A. Ariya and Professor Thomas C. Preston for being wonderful supervisors during all of my Ph.D. work. I am grateful to Prof. Ariya for providing me with the opportunity to grow here, both professionally and personally. I am also grateful to Prof. Preston for all the conference support. I extend my appreciation to Profs. Andreas Zuend, Patrick Hayes, Amy Blum, and David Straub for providing along invaluable comments.

I acknowledge the financial support of several Canadian funding agencies for making this research possible. Support for the first project of this thesis came from Natural Sciences and Engineering Research Council of Canada (NSERC) (223464), fonds de recherche du Québéc: Nature et technologies (FRQNT), and Canadian Foundation for Innovation (CFI) through PAA. The second and third projects of this thesis were supported by NSERC through TCP.

The performance of the first project of this thesis relied on numerous data sources and providers. Data were provided by NASA LANCE Rapid Response (for MODIS MYD04_L2 product), NASA GIOVANNI Data and Information Services Center (for Deep Blue and AOD products), USGS Earth Explorer (for SRTM data and Landsat TM images), NOAA Physical Science Division (NCEP/NCAR Reanalysis product for wind direction), NOAA Air Resource Laboratory (HYSPLIT back trajectory for source point evaluation), and Google Earth images over study area. Also, Iran Meteorological Organization is acknowledged for sharing data with AM and NK. We thank Dr. P. Ginoux from NOAA GFDL at Princeton who generously sent us the original data used for comparative work in this study. Finally, we thank Ms. Cavaliere for proofreading the two publications of this work.

I would like to thank my parents, Gholamreza and Mahnaz, my siblings, Elham and Milad, and amazing friends for their unconditional support and encouragement during these years.

Chapter 1

Introduction

1.1 The Earth's Atmosphere

1.1.1 Composition

The atmosphere of the Earth consists of a mixture of gases largely nitrogen (N_2, 78.08 %) and oxygen (O_2, 20.95 %). The small remaining fraction is argon (Ar), carbon dioxide (CO_2), water vapor (H_2O) and trace gases. Although the atmosphere is vertically stretched up to hundreds of kilometers, almost 99 % of its total mass falls below 30 km above the Earth's surface.[1] This is due to the increase in density and pressure close to the surface (stronger gravitational force).

The composition of the atmosphere is almost uniform up to an altitude of 85 km and is called the homosphere. However, the gaseous portion of the atmosphere starts to change significantly in heterosphere (above 85 km) due to the separation of chemical species by gravity and also due to dissociation by solar radiation.[2] Gaseous constituents of the atmosphere can be classified based on their residence time and fall into three main classes: (1) quasi-constant with residence times of thousand years or more (e.g. N_2, O_2, Ar, He, Ne, Kr, and Xe), (2) slow varying with residence times of few months to few years (e.g. CH_4, O_3, N_2O, CO, CO_2, and H_2), (3) fast varying with residence times of few days or less (e.g. SO_2, H_2S, NO_2, NH_3, and radicals such as OH, HO_2, NO, NO_3). The gases Ar, Ne, Kr, and Xe (called noble gases) do not have a significant source or sink in the atmosphere compared to others so they are permanent.[2] Figure 1.1 shows the vertical profile of the mixing ratios of selected species in

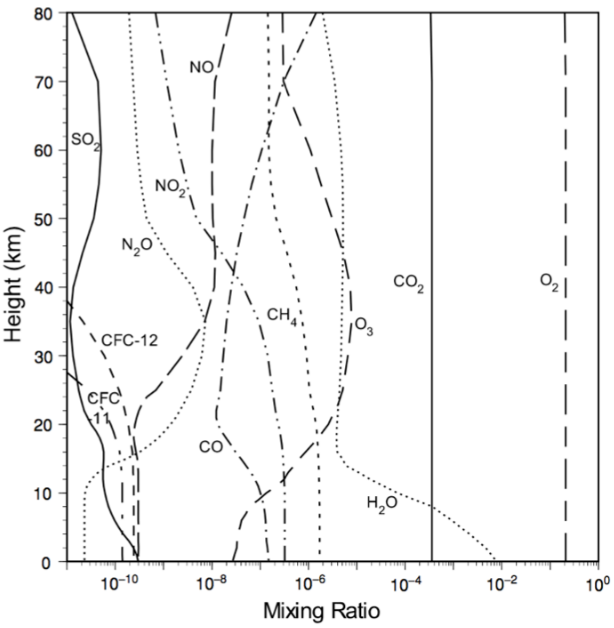

Figure 1.1: Vertical profiles of mixing ratios for selected species at mid-latitude conditions (from Ref. 3)

the atmosphere. It is evident that the mixing ratio of H_2O significantly decreases from 0.01 in troposphere to relatively constant at 3 ppm in stratosphere.

1.1.2 The Temperature Profile of the Atmosphere

Looking at the vertical profile of the temperature (Figure 1.2), we can divide the atmosphere into several layers. In the bottom layer, the troposphere, the temperature decreases with height up to 10-15 km altitude (the so called tropopause). The rate at which the temperature of the troposphere decreases with altitude is often called the lapse rate in atmospheric science. The troposphere is the most dense layer (with 80 % of the total mass of the atmosphere) and the vertical mixing is fast in this layer. The second layer, the stratosphere, starts right above the tropopause and extends up to 50 km altitude (the so called stratopause). Due to the absorption of ultra violet radiation energy by ozone, the temperature increases with height in the stratosphere and reaches -3° C at the stratopause. Compared to the troposphere, the stratosphere is dry and less dense and vertical mixing is slow.[4] The mesosphere and the thermosphere are the other top layers of the atmosphere (from 50 km to 100 km) where the temperature drops to 200 K.

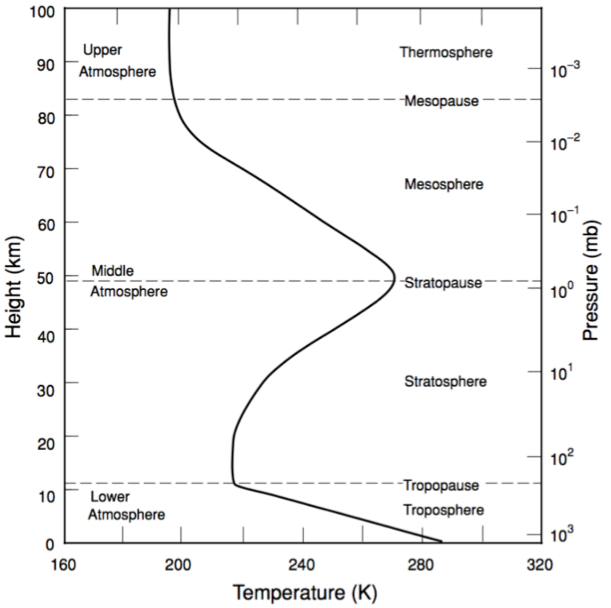

Figure 1.2: Classifying the atmosphere into layers based on the average profile of air temperature (from Refs. 1 and 3)

1.1.3 Water Vapor in the Atmosphere

The most variable component of the Earth's atmosphere is water vapor (0-4 % of mass) and it has a critical role in atmospheric processes. It is the most dominant greenhouse gas (GHG) with complex and uncertain feedback mechanisms.[5] Water vapor can be transformed into the form of liquid or solid particles. Large amounts of latent heat are released during condensation of water vapor and it gets absorbed during the evaporation or sublimation of condensate.[6] The phase change and the associated energy transfer can be key elements in (i) the vertical stability of the atmosphere and (ii) the balancing the Earth's meridional energy.[7] In addition, water vapor is a vital constituent in understanding atmospheric chemistry. Water vapor is central to cloud formation and precipitation in the troposphere. Thus, water vapor plays an extremely important role in dynamic and thermodynamic processes in our atmosphere.

To quantify the water vapor content in the atmosphere, a number of different methods have been presented. As a result, there are several definitions for the water vapor content. One can involve mass and volume. The ratio of the mass of water vapor to the volume of air is called the water vapor density. Another way is to involve only mass. Then, the ratio of mass of water vapor to mass of dry air is called mixing ratio and the ratio of mass of water vapor to mass of moist air is called specific humidity. Due to the small mass of water vapor, the mixing ratio and specific humidity can have very close numerical values.[8] The most common way to express moisture content in the atmosphere is by using the pressure exerted by the water vapor.[1] The ratio of actual water vapor pressure to the saturation vapor pressure (maximum capacity) is called the relative humidity (RH). From the definition, RH is a function of both the water content and the temperature of the air. For the same water content, RH increases when the temperature of the air decreases.

Understanding the effect of water vapor on the diffusion kinetics and light scattering by aerosol particles is the subject of the second half of this thesis. By introducing RH, we are able to build models that can take RH as an input parameter (as well as other variables).

1.2 Atmospheric Aerosol Particles

Particles in the atmosphere can be categorized on the basis of their size, composition, moisture content and terminal velocity into atmospheric aerosol particles, cloud particles, and hydrometeors (drizzle drops, raindrops, snow crystals, graupel and hail stones).[9] Atmospheric aerosol consists of liquid or solid particles suspended in air.

1.2.1 Aerosol Processes

A large fraction of atmospheric aerosols are formed through conversion of gas-phase species in the atmosphere into particles. This process is called atmospheric aerosol nucleation. The formation mechanism has been extensively reviewed by Zhang et al.[10] The formation process of new particles involves two major steps: (1) nucleation (creation of clusters before phase change) from vapor to create critical nucleus (through random collision and rearrangements of atoms and molecules), and (2) growth of the clusters to nanoparticles larger than 2-3 nm (mainly through condensation). These new nanoparticles can sometimes collide with pre-existing particles in the atmosphere and change the internal mixing of the particle. Overcoming the free energy of cluster formation as well as the high equilibrium vapor pressure upon cluster formation can potentially hinder the nucleation and growth of nanoparticles.[10] If the cluster is formed on pre-existing small particles or ions (heterogeneous formation), the free energy barrier will be much smaller compared to homogeneous cluster formation. Important properties for chemical species to act as nucleating precursor are abundance, volatility, and reactivity.[10]

Key contributors to cluster formation in the atmosphere are gaseous compounds of very low volatility (e.g., sulfuric acid and highly oxidized organic compounds) or compounds that can facilitate the formation of low-volatile compounds, such as gaseous ammonia or amines that form acid-base compounds with inorganic or organic acids, water molecules that cluster through hydrogen bonding, and potentially ions that can form clusters through electrostatic interactions.[11] Condensation of these vapors are the main drivers of aerosol particle growth.

The residence time of tropospheric aerosols is quite variable, ranging from a few days to a couple of weeks. The main sink processes are: (a) dry deposition, which depends on particle size and the characteristics of the Earth's surface, (b) wet deposition, nucleation or scavenging by cloud droplets and raindrops and (c) gravitational settling or sedimentation for coarse particles. According to the most recent IPCC report, one of the largest sources of uncertainty in aerosol modeling is the lack of comprehensive parameterization of wet deposition.[9]

1.2.2 Aerosol Modes

Atmospheric aerosols can be classified based on their size (Figure 1.3):[12]

(1) ultrafine particles (0.001-0.01 μm) are generated from clusters of gas molecules by nucleation. Some precursor gases are NH_3, HNO_3, H_2SO_4, and organic compounds. This category is also called Aitken mode.

(2) fine particles (0.01-1 μm) are produced from fast growth of ultrafine particles by condensation of precursor gases and from collision of particles (coagulation). Sulfuric acid (H_2SO_4), the oxidation product of sulfuric dioxide (SO_2), is one major precursor gas and can produce aqueous sulfate particles in the atmosphere. Condensation of hydrocarbons can generate organic carbon which is the large fragment of fine aerosols. Soot is another fine particle from condensation of gases during incomplete combustion. Since particles that are formed by condensation of gases will accumulate in this size range, this size domain is called the accumulation mode.

(3) coarse particles (1-10 μm) are mechanically generated by the action of wind on the surface of the Earth. The rate of random collision between particles is very slow in this category.

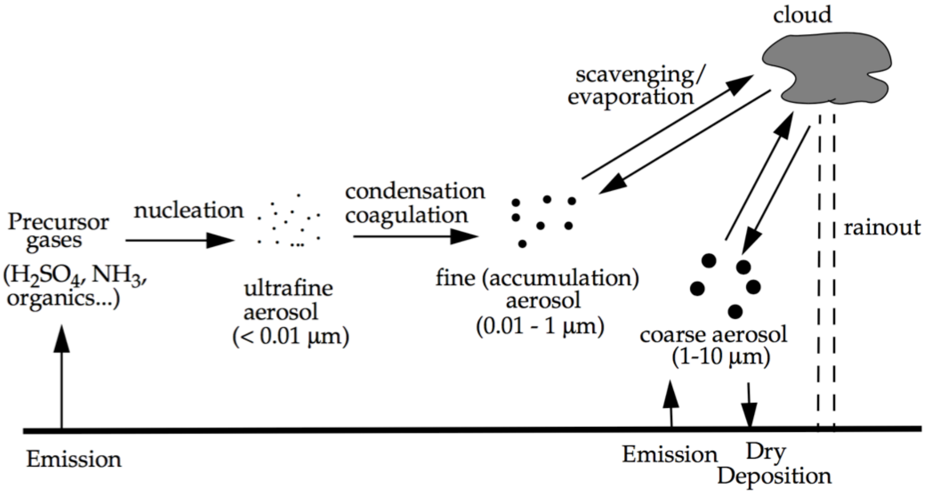

Figure 1.3: Atmospheric aerosol particle size classification (from Ref. 12).

Examples of coarse particles are sea salt (from ocean spray), mineral dust (mainly from deserts), bacteria, pollen, spores, fungi, volcanic dust, and biological debris.[12]

The concentration of coarse particles is around 1 cm^{-3}. For the accumulation mode, the number density of particles varies between 10-1000 cm^{-3} which is comparable to the concentration of cloud droplets. For a typical atmosphere, ultrafine particles dominate the aerosol number density from 100 cm^{-3} in clean air to 10^5 cm^{-3} in the polluted air. However, due to the very small mass and also the surface area, these particles have little direct impact on climate as opposed to the accumulation mode particles. Air mass concentration in the atmosphere even in heavily polluted air does not exceed 1000 μg m^{-3}.

1.2.3 Aerosol Composition

The composition of the atmospheric aerosol primarily consists of inorganic species (e.g. sulfate, nitrate, ammonium, sea salt), organic materials, elemental carbon (also known as black carbon), minerals (such as dust from dried surfaces), and biological species. There are over 40 trace elements typically found in atmospheric aerosol particles. The mass of these elements greatly varies in time and space due to different sources on the Earth's surface. Crustal elements (Si, Ca, Mg, Al, Fe, and Ti) oxides fall in the course mode while metals like Pb, Cd, V, Ni, Cu, Zn, and Mn are found in fine mode. Most of coarse mode aerosols are non-hygroscopic.[4]

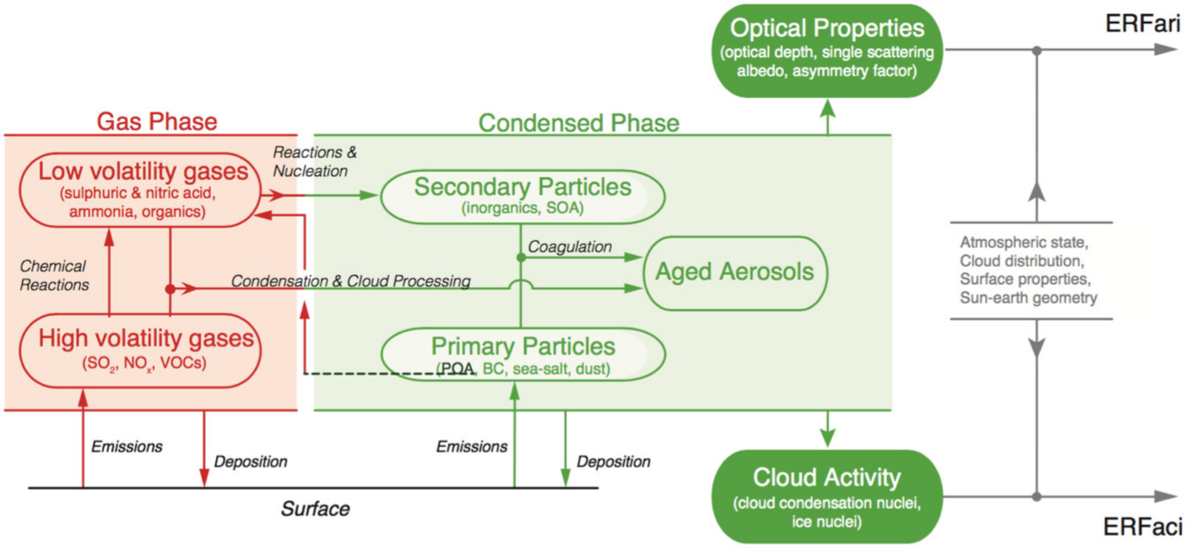

Figure 1.4: General aerosol gas phase and condensed phase variables and processes in the atmosphere (from Ref. 9).

1.2.4 Aerosol Sources

Another way to classify the atmospheric aerosol particles is by their origin. They can have natural and anthropogenic sources. Each of these main sources can also be divided into primary (directly emitted from the Earth's surface) and secondary (formed in the gas phase in the atmosphere) sources (Figure 1.4). With these definitions, we can now differentiate major atmospheric aerosols into the following groups:[4]

- Natural aerosols
  - Primary: mineral dust, sea salt, volcanic dust, biological debries
  - Secondary: sulfates from dymethilsulphide, sulfates from volcanic SO_2, organic aerosol from biogenic volatile organic compounds
- Anthropogenic aerosols
  - Primary: industrial dust, black carbon, organic aerosol
  - Secondary: sulfates from SO_2, nitrites from NO_x, organic aerosol

1.3 Climate Relevant Aerosol Properties

The impact of atmospheric aerosol particles on climate is controlled by their spatial distribution, hygroscopicity, optical properties, and their contribution in serving as cloud condensation nuclei (CCN) and ice nuclei (IN). The optical and CCN properties of aerosol particles are determined by aerosol size distribution, chemical composition and mixing state, and morphology.[9] The climate impact of inorganic aerosols have been well investigated and understood while there are huge uncertainties associated with the role of organic aerosols in affecting climate.

1.3.1 Aerosol Hygroscopicity

Particle hygroscopicity can influence aerosol chemical reactivity, radiation interactions, and droplet activation and cloud formation. The ability of atmospheric aerosol particles to take up water at a given RH in the atmosphere is called hygroscopicity. Based on their affinity to water, aerosol particles can be hydrophilic, neutral, or hydrophobic. Hydrophobic particles are water resistant and hydrophilic particles have a great affinity to water. Most known hydrophilic aerosol particles contain inorganic species such as ammonium nitrate (NH_4NO_3), ammonium sulphate ($(NH_4)_2SO_4$) and sodium chloride (NaCl).[13] The hygroscopic behavior of organic particles, however, requires more research work to reduce current associated uncertainties.

There are various methods to measure the hygroscopicity of an aerosol. The size dependance of aerosol hygroscopicity allows one to define the growth factor (GF),

$$\mathrm{GF} = \frac{D_{wet}}{D_{dry}} \tag{1.1}$$

where D_{wet} and D_{dry} are the particle diameter for wet and dry conditions.

Experimental measurement of aerosol growth factor has been done through measuring the change of aerosol size as a function of RH using hygroscopicity tandem differential mobility analyzer (HTDMA)[14] or by single particle techniques such as the electrodynamic balance (EDB)[15] or optical tweezers.[16] All of these techniques provide very accurate measurements of aerosol hygroscopicity with some limitations and conditions. For instance, HTDMA is slow as it uses a secondary DMA to measure size distribution of the grown particles. It cannot also measure the D_{dry} larger than 0.5 μm. The relative humidity-moderated differential mobility optical particle size spectrometer (RH-DMOPSS)[17] has overcome to these limitations and can perform faster over wider range of particle sizes. However, it can measure growth factor at only one RH every time. Aerosol hydration spectrometer (AHS)[18] is another instrument that is used to measure in situ aerosol hygroscopicity for D_{dry} between 0.25-3.5 μm. In addition, the differential aerosol sizing and hygroscopicity spectrometer probe (DASH-SP)[19] combines multiple systems of growth factor measurements and provide the growth factors of particles at any selected size in few seconds. Using an aerosol mass spectrometer (AMS) and DASH-SP data, a volume-weighted mixing rule is utilized to calculate the total hygroscopic growth factor in a multi-component aerosol particle based on the GF of each individual species:

$$\mathrm{GF}_{\mathrm{mixed}}(a_w) = \left(\sum_i \epsilon_i \mathrm{GF}_i(a_w)^3 \right)^{1/3} \tag{1.2}$$

where $\mathrm{GF}_{\mathrm{mixed}}$ is total hygroscopic growth factor, a˙w is activity of water, GF_i is the hygroscopic growth factor for pure species i, and ϵ_i is the volume fraction of species i.[19]

Since hygroscopicity impacts the optical properties of an aerosol particle, these two parameters have been measured as a function of RH at the same time. To measure light scattering as a function of RH, a nephelometer is used as the typical instrument.[20] Then, the measured scattering coefficient at each RH and wavelength is divided by a reference scattering coefficient. This fraction is called light scattering growth factor[21] or scattering enhancement parameter[22]:

$$f(\mathrm{RH}, \lambda) = \frac{\sigma_{sp}(\mathrm{RH}, \lambda)}{\sigma_{sp}(\mathrm{RH}_{\mathrm{dry}}, \lambda)} \tag{1.3}$$

where $\sigma_{sp}(\mathrm{RH}, \lambda)$ is the scattering coefficient at a given RH and wavelength λ and $\sigma_{sp}(\mathrm{RH}_{\mathrm{dry}}, \lambda)$ is the associated scattering coefficient. This parameter is used to interpret the impact of hygroscopicity on scattering.

1.3.2 Aerosol Size Distribution

Aerosol size distribution is the key parameter in aerosol activation parameterizations. Summarized by Ghan et al.,[23] the aerosol size distribution is estimated by a power law[24]

$$\frac{dN}{dr_d} = ar_d^{-b}, \tag{1.4}$$

multiple sections[25–27]

$$\frac{dN}{dr_d} = \frac{N_i}{r_i - r_{i-1}}, \tag{1.5}$$

or multiple lognormal distribution[25,28]

$$\frac{dN}{d\ln r_d} = \sum_m \frac{N_m}{\sqrt{2\pi}\ln\sigma_m} exp\bigg(- \frac{\ln^2(r_d/r_m)}{2\ln^2\sigma_m}\bigg), \tag{1.6}$$

where a and b are the size distribution constants, N_i and r_i are the number concentration and dry radius in section i, and N_m, r_m, and σ_m are number concentration, radius and geometric standard deviation in mode m, respectively.

Feingold[29] in 2003 assessed the relative importance of size and composition of aerosol particles on the cloud drop size. Later in 2006, McFiggans et al.[30] explored this further and assessed the sensitivity of drop number concentration as well. Both studies report higher sensitivity of activation to aerosol size than aerosol composition. This finding was recognized as a primary pre-requisite and it has become the fundamental assumption for the measurements of aerosol number size distribution in Europe in 2008-2009.[31] In that project, they measured submicron particles (30-500 nm) over two years of harmonized aerosol number size distribution data from 24 European field monitoring sites. It is necessary to perform more such field measurements in other geographical locations to help the modeling community to test and validate their schemes.

1.3.3 Aerosol Effect on CNN

The size and composition of aerosol particles control their hygroscopicity as well as their CCN activity at supersaturation. The typical constituents of atmospheric CCNs are sea salt, sulphates ($SO_4{}^{-2}$), sulphuric acid, nitrate ($NO_3{}^{-}$), and nitric acid (HNO_3). Efficiency of an aerosol to act as CCN is quantified by hygroscopicity factor in the framework of Köhler theory (κ-theory) introduced by Petters and Kreidenweis[32] for soluble particles or by adsorption activation theory based on the multilayer Frenkel-Halsey-Hill (FHH) adsorption isotherm model presented by Kumar et al.[33] for insoluble particles (e.g., dust, black carbon, volcanic ash).

The first attempts to link the aerosol and cloud droplet and represent it in climate models were based on the empirical relationships between CCN and aerosol species.[34] These relationships limit their applicability to the broader range of conditions. Also, they do not include the dependency of nucleation on size distribution, composition, or updraft velocity.[23] Therefore, more physically based aerosol activation schemes have been developed towards precise modeling of CCN concentration.

To quantify CCN concentration and to understand the formation of clouds by aerosol particles, it is essential to describe the droplet nucleation theory (or theory of activation of aerosol particles). This theory was first introduced by Köhler in 1926.[35] He found the equilibrium size of particles as a function of their dry radius and relative humidity. It can be derived from a modified version of Clausius-Clapeyron equation which explains the equilibrium condition for a thermodynamic system made of bulk water and its vapor. The modification is required because for small droplets, the phase transition does not happen due to the free energy barrier. The embryonic droplet tends to become stable after reaching a critical size. Typically, droplets larger than the critical size will grow spontaneously. The critical size depends on the balance between the rates of condensation and evaporation. Homogeneous (by random collisions of molecules) or heterogeneous (by contact with another type) formation of droplet determines the growth and decay rates. In homogeneous process, the growth rate depends on the partial pressure of water vapor and decay rate depends on the droplet temperature and surface tension.[36] At equilibrium, the vapor pressure is equal to the equilibrium vapor pressure over the surface of particle and is expressed by Kelvin's equation:[37]

$$e_s(r) = e_s(\infty) \exp\left(\frac{2\sigma}{rR_v\rho_L T}\right) \tag{1.7}$$

where $e_s(r)$ and $e_s(\infty)$ are the saturation vapor pressures at the surface of spherical droplet with radius r and over bulk water respectively, σ is surface tension, ρ_L is droplet density, T is the temperature and R_v is the gas constant for water vapor. The difference between the actual ambient vapor pressure (e) and saturation vapor pressure over the droplet surface ($e_s(r)$) determines the decay or growth of droplet. The critical radius is reached when these two quantities are equal ($e = e_s(r_c)$). Therefore

$$r_c = \frac{2\sigma}{R_v \rho_L T \ln S} \tag{1.8}$$

where $S = e/e_s(\infty)$ is saturation ratio at this radius (also called critical saturation ratio). Homogeneous nucleation of pure water needs several hundred percent RH which is quite rare in the real atmosphere. In fact, the supersaturation does not exceed 1 or 2 percent. Therefore, homogeneous nucleation is less feasible under atmospheric conditions.

Instead, the hydrophilic atmospheric aerosol particles can decrease the equilibrium pressure of a liquid. When adding a solute to a liquid, some of the solute molecules will replace the liquid molecules at the surface. As a result, the required supersaturation becomes quite small compared to the pure liquid droplet. The equilibrium vapor pressure over a solution (e') consist of u_0 molecules of water and u molecules of solute is expressed according to the Raoult's Law:

$$e' = e_s(\infty)\left(\frac{u_0}{u + u_0}\right) \tag{1.9}$$

The combination of Kelvin and Raoult equations can help to derive an expression for Köhler theory:

$$S = \frac{e'_s(r)}{e_s(\infty)} \approx 1 + \frac{a}{r} - \frac{b}{r^3} \tag{1.10}$$

where $a = 2\sigma/rR_v\rho_L T$ and $b = 3ig_vM/4\pi\rho_L g_s$, and where i is degree or ionic dissociation (van's Hoff factor), M is mass of solute, g_s and g_v are molecular weight of the solute and water vapor. a/r is curvature effect or kelvin term and b/r^3 is solute effect or Raoult term. From the signs of these terms in this approximation, it is evident that curvature term increases the saturation ratio while it gets reduced by the solute term. Figure 1.5 shows a Köhler curve, the result of combing two Kelvin and Raoult effects. As illustrated, at very small radius, the solute effect dominates. Below maximum supersaturation, called the critical supersaturation S_c, the solution droplet will grow or decay to its equilibrium size upon an increases or decrease in RH. The droplets are called haze particles in this region. If relative humidity goes beyond 100 % and reaches the critical supersaturation (peak on Köhler curve), the droplet reaches the critical radius and the condensation nuclei is activated.[36] After this point, the droplet will spontaneously grow without increase in RH. However, due to the presence of other droplets in the cloud, this spontaneous growth will not last indefinitely. The critical radius and critical supersaturation then become:

$$r_c = \sqrt{\frac{3b}{a}} \tag{1.11}$$

$$S_c = 1 + \sqrt{\frac{4a^3}{27b}} \tag{1.12}$$

The parameter b can also be expressed as $b = Kr_d^3$, where r_d is the dry radius and K is the hygroscopicity parameter,

$$K = \frac{V_w}{V_s}\Big(\frac{1}{a_w} - 1\Big) \tag{1.13}$$

where V_w and V_s are the volume of the water and solute respectively. The hygroscopicity parameter links the water activity to the volume ratio of water to solute. For the particles consisting of multi-constituents, it can be defined as the volume mean of hygroscopicity of each component. The κ-Köhler theory, introduced by Petters and Kreidenweis[32], can be applied to the multi-component aerosol particles:

$$S = \frac{D_{wet}^3 - D_{dry}^3}{D_{wet}^3 - D_{dry}^3(1-K)} \exp\Big(\frac{4\sigma V_w}{RTD_{wet}}\Big) \tag{1.14}$$

Here K is the hygroscopicity parameter of multi-component particle and is $K = \sum_i \kappa_i \epsilon_i$, where κ_i and ϵ_i are the hygroscopicity parameter and volume fraction of each constituent.

The number of nucleus is estimated to be $N = CS_c^a$, where N is number of nuclei per unit volume activated at S_c and C and a depend on airmass type (maritime or continental).[36]

1.3.4 Aerosol Effect on IN

Aerosol particles can also act as IN. In a recent study, Hoose and Mohler[38] analyzed the results from six decades of laboratory work of heterogeneous ice nucleation. Figure 1.6 (taken from their work) shows different nucleation modes over a wide range of temperature and su-

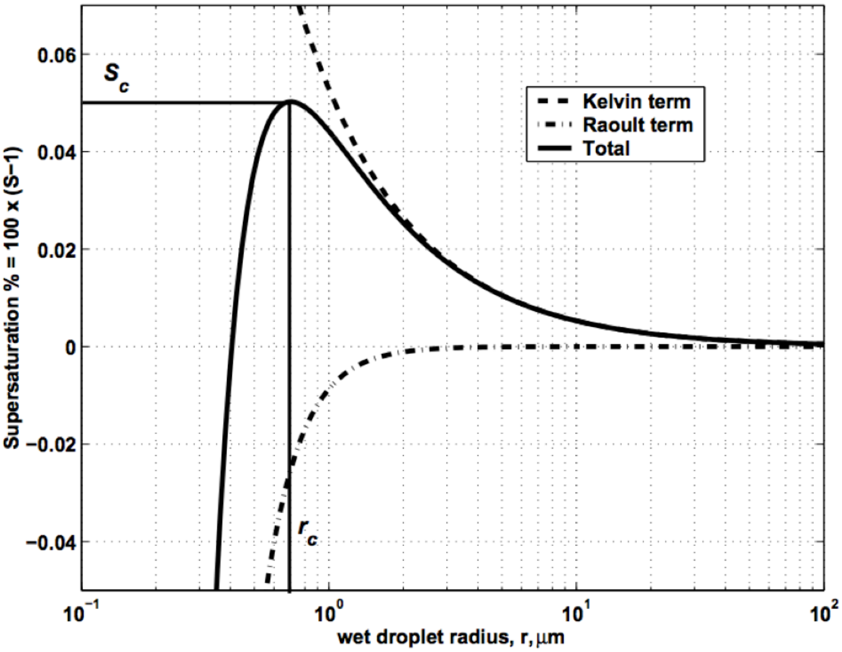

Figure 1.5: Competition between the curvature and solute terms in Köhler equation (from Ref. 30)

persaturation with respect to ice. As shown, the homogeneous nucleation of droplets occurs at temperature below -38° C and quite high supersaturation (above 400 %). The main heterogeneous ice-nucleation modes by aerosol particles are contact freezing (from collision with an IN), immersion freezing (from an IN inside the droplet), deposition (vapor deposition directly on IN), and condensation nucleation (freezing while droplet is forming). INs are typically solid and insoluble. The common atmospheric IN are mineral dust, volcanic ash, and primary biological aerosol particles (e.g. bacteria, fungal spores, pollen).[9]

The classical nucleation theory explains the rate at which the new phase nucleates from a metastable phase. This theory has been widely used to describe two ice nucleation processes: (i) homogeneous ice nucleation from supercooled water or supersaturated water vapor and (ii) heterogeneous ice nucleation from ice nuclei substance. Clusters of larger than a critical size can contribute in ice formation. The corresponding Gibbs energy of critical cluster formation is:[39]

$$\Delta G^* = \frac{16\pi\gamma^3 V^2}{3k^3 T^3 (\ln S)^2} \tag{1.15}$$

where V is the molecular volume of the condensed phase, γ is the interfacial energy between

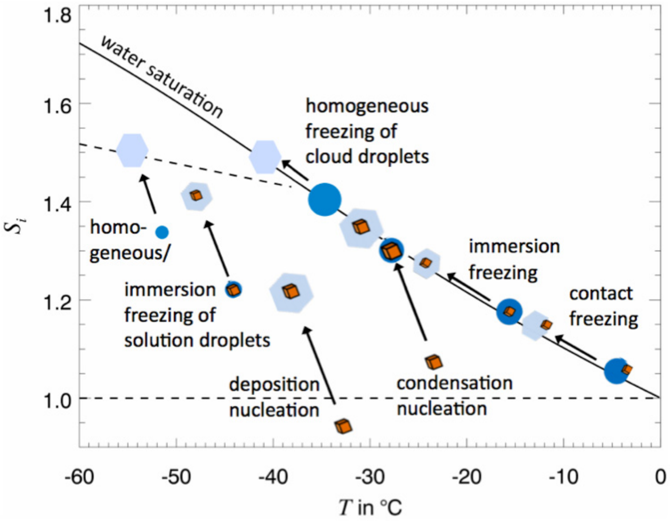

Figure 1.6: Various nucleation modes as a function of supersaturation and temperature (from Ref. 38)

the new and metastable phases, S is the saturation ratio with respect to ice (P_{water}/P_{ice}), T is the temperature, and k is the Boltzman constant. The ice nucleation rate per unit volume per unit time can be described using the following equations:

$$J = A \exp\Big(-\frac{\Delta G^{*}\phi}{kT}\Big) \tag{1.16}$$

where A is a pre-exponential factor in units of cm^2 s^{-1} and ϕ is the factor that describes how solute decreases the height of the energy barrier relative to homogeneous nucleation. For homogeneous ice nucleation $\phi = 1$ and for heterogeneous ice nucleation it is stated based on the ice nucleation efficiency parameter.[39]

1.3.5 Aerosol Optics

Particles consist of discrete electrical charges. When a particle is exposed to oscillating electromagnetic radiation field, these charges in the particle become excited into oscillatory motion. The particle may reradiate the light in all directions and form a secondary scattering field. It can also convert the incident plane wave into thermal energy which is called absorption. Conventionally, radiation waves are expressed in terms of wavelength (λ, nm) in visible, wave number ($\bar{\nu} = 1/\lambda$, cm^{-1}) in infrared, or frequency ($\nu = c/\lambda = c\bar{\nu}$, GHz) in microwave/radio portion of energy spectrum.

The energy scattered (W_{sca}) or absorbed (W_{abs}) by a particle is proportional to the intensity of the original incident energy (I_0). The proportional factor is called cross section and is expressed in the unit of area (m^2). The single particle scattering cross section is then:

$$\sigma_{sca} = \frac{W_{sca}}{I_0} \tag{1.17}$$

The single particle absorption cross section (σ_{abs}) is defined analogously. From conservation of energy, the combination of scattering and absorption effects gives extinction cross section:

$$\sigma_{ext} = \sigma_{sca} + \sigma_{abs} \tag{1.18}$$

It is noted that all of these cross sections are per unit mass. Also, the extinction cross section considers an effective area of the particle in the eye of incident light. Therefore, the dimensionless extinction efficiency (Q_{ext}) is obtained when the particle geometric cross section ($\sigma_{geom} = \pi r^2$) is also considered:

$$Q_{ext} = \frac{\sigma_{ext}}{\sigma_{geom}} = Q_{sca} + Q_{abs} \tag{1.19}$$

where Q_{sca} and Q_{abs} are scattering and absorbtion efficiencies and are defined in the similar way. The fraction of the energy extinction that is scattered by particle is called the single scattering albedo:

$$w = \frac{Q_{sca}}{Q_{ext}} = \frac{\sigma_{sca}}{\sigma_{ext}} \tag{1.20}$$

and $1 - w$ the fraction that is absorbed. Figure 1.7 shows the different optical processes for an illuminated spherical particle. The mechanism of particle light scattering can be categorized into two main classes:

- Elastic scattering (refraction, reflection, diffraction) in which the momentum of the light changes but the energy of the light remains the same. This means the wavelength or frequency of the scattering wave is equal to that of incident light (λ_0 in Figure 1.7).

- Inelastic scattering (absorption, fluorescence, Raman) in which the energy of the light

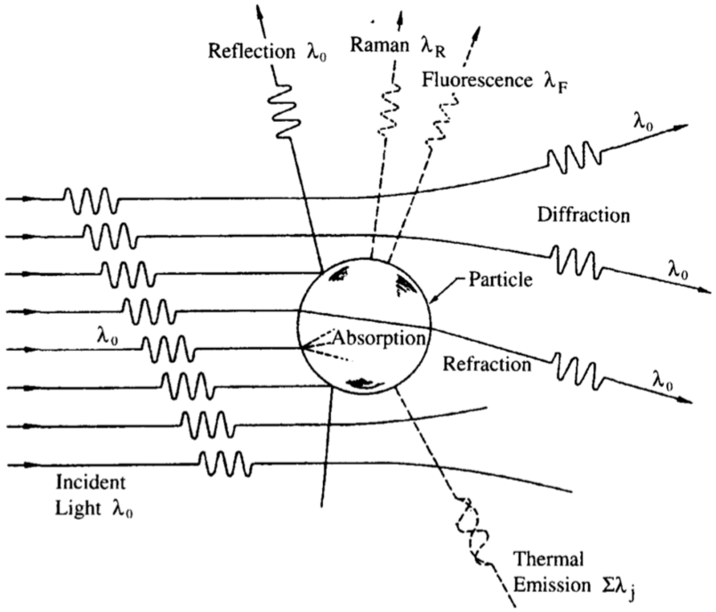

Figure 1.7: Optical processes for an illuminated particle (from Ref. 4)

changes and the wavelength of emitted radiation is different of that of incident light.

In the field of atmospheric science where the interaction of solar radiation with the atmospheric aerosol particles is taken place, the elastic and inelastic scattering are of interest.[4] Figure 1.7 only shows the interaction of light with a spherical homogeneous particle. Identifying these processes is much more difficult for a non-spherical and non-homogeneous particle.

The scattering and absorption by particle are problems in electromagnetic theory. In this theory, the most important variables in determining the particle absorption and scattering are (a) the wavelength of incident wave (λ), (b) the particle size that is typically expressed by dimensionless particle size parameter ($x = 2\pi r N_0/\lambda$) and (c) particle composition that is described by particle complex refractive index ($N = n + ik$) which is the optical property of particle relative to the surrounding medium. Here, n and k are the real (scattering) part and imaginary (absorption) part of the complex refractive index respectively and both depend on λ. It is common to normalize N by the refractive index of surrounding medium N_0, stated by $m = N/N_0$. Since the air in the atmosphere is the typical medium of interest and its refractive index is 1, it is a good assumption to say $m = n + ik$. With this consideration, the size parameter is then $x = 2\pi r/\lambda$.

Light scattering by particles can be classified based on the size parameter into three regimes:

(1) Rayleigh scattering ($x \ll 1$) when particle size is smaller than the wavelength of the incident light. In this case, the scattering depends strongly on the wavelength and the refractive index becomes insignificant. Thus, $Q_{sca} \propto \lambda^{-4}$, which means the shorter wavelength the stronger the intensity of scattering. An example of this is air molecules that scatter the blue wavelength more effective and sky appears to have blue color. In general, the scattering of sunlight by molecules is known as Rayleigh scattering. The Rayleigh theory assumes that molecules are homogeneous and isotropic spheres.

(2) Mie scattering ($x \simeq 1$) when particle size is comparable to the wavelength of the incident light. Mie regime is also called aerosol particle scattering and is the most interest for the last two chapters of the present work. Mie-Lorenz theory explains the scattering and absorption of the spherical homogeneous particles in this range. Typical aerosol particle exhibits a maximum diffraction in the 150°-170° scattering field.[3] (0° starts at right side on horizontal direction and 180° is going counterclockwise from 0° to the left).

(3) Geometric scattering ($x \gg 1$) when particle size is much larger than the wavelength of incident radiation. In this case, the scattering depends strongly on the particle shape and orientation relative to the incident wave. The asymptotic approximations of electromagnetic theory is the principle of geometric optics.[3] The incident radiation beam is considered a group of multiple separate parallel rays (localization principle). The combination of geometrical optics of refraction, reflection, and diffraction make up the total scattering field. These particles have usually a strong forward scattering. An example of this is cloud droplet ($\sim$10μm) that is characterized by a large forward diffraction at $\sim$138° scattering angle (famous rainbow phenomenon).

In the light scattering problem, the electromagnetic field is assumed to be time-harmonic and it satisfies the wave equation in a linear, isotropic, homogeneous medium.[40] The electric field (E) and magnetic field (H) are expressed in terms of superposition of spherical wave functions (M and N) and make up the incident electromagnetic field (E_i,H_i)

$$E_i = E_0 \sum_{n=1}^{\infty} i^n \frac{2n+1}{n(n+1)} \left(M_{o1n}^{(1)} - i N_{e1n}^{(1)} \right) \tag{1.21}$$

$$H_i = \frac{-k}{\omega\mu} E_0 \sum_{n=1}^{\infty} i^n \frac{2n+1}{n(n+1)} \left(M_{e1n}^{(1)} + i N_{o1n}^{(1)} \right) \tag{1.22}$$

as well as electromagnetic field inside (E_1,H_1) using expression coefficients c_n and d_n

$$E_1 = E_0 \sum_{n=1}^{\infty} i^n \frac{2n+1}{n(n+1)} \left(c_n M_{o1n}^{(1)} - i d_n N_{e1n}^{(1)} \right) \tag{1.23}$$

$$H_1 = \frac{-k_1}{\omega\mu_1} E_0 \sum_{n=1}^{\infty} i^n \frac{2n+1}{n(n+1)} \left(d_n M_{e1n}^{(1)} - i c_n N_{o1n}^{(1)} \right) \tag{1.24}$$

and outside scattered electromagnetic field (E_2,H_2) using scattering coefficients a_n and b_n

$$E_2 = E_0 \sum_{n=1}^{\infty} i^n \frac{2n+1}{n(n+1)} \left(i a_n N_{e1n}^{(3)} - b_n M_{o1n}^{(3)} \right) \tag{1.25}$$

$$H_2 = \frac{-k}{\omega\mu} E_0 \sum_{n=1}^{\infty} i^n \frac{2n+1}{n(n+1)} \left(i b_n N_{o1n}^{(3)} - a_n M_{e1n}^{(3)} \right) \tag{1.26}$$

where k is the wavenumber in surrounding medium, μ is the permeability of the medium, ω is the angular frequency of light, E_0 is the intensity of incident field. The $M^{(j)}$ and $N^{(j)}$ ($j = 1, 3$) are the spherical Bessel ($j = 1$) and spherical Hankel ($j = 3$) functions (discussed in literature elsewhere). The scattering coefficients are:

$$a_n = \frac{m\psi_n(mx)\psi_n'(x) - \psi_n(x)\psi_n'(mx)}{m\psi_n(mx)\xi_n'(x) - \xi_n(x)\psi_n'(mx)} \tag{1.27}$$

$$b_n = \frac{\psi_n(mx)\psi_n'(x) - m\psi_n(x)\psi_n'(mx)}{\psi_n(mx)\xi_n'(x) - m\xi_n(x)\psi_n'(mx)} \tag{1.28}$$

where ψ_n and ξ_n are Riccati-Bessel functions. Knowing the scattering coefficients, we can calculate the cross sections of a spherical particle using following expressions:[40]

$$Q_{sca}(m,x) = \frac{2}{x^2} \sum_{n=1}^{\infty} (2n+1)(|a_n^2|+|b_n^2|) \tag{1.29}$$

$$Q_{ext}(m,x) = \frac{2}{x^2}\sum_{n=1}^{\infty}(2n+1)\mathrm{Re}(a_n + b_n) \tag{1.30}$$

where Re is the real part of the scattering coefficients.

Figure 1.8 shows Q_{ext} of a spherical non-homogeneous particle while it takes up water at chosen time steps. Q_{ext} changes as the particle size and composition evolve in time. Each spectrum has number of sharp spikes that are sometimes called the ripple structure. These optical resonances of spherical dielectric particles are called morphology dependent resonance (MDRs) or whispering gallery modes (WGMs). WGMs in elastic light scattering can be utilized to perform measurements of particle size, composition (refractive index), shape distortion, and temperature of spherical particles with high accuracy.[41] Also, the WGMs can create a unique pattern in fluorescence and Raman spectroscopy. The WGMs are seen as light waves inside the particle that hit repeatedly the interface and circulate just underneath the particle surface.

To calculate wavelengths commensurate with the WGMs inside the particle, three important property of particle need to be considered: size parameter, shape, and refractive index. The WGMs that form the internal field are function of angle and radius. A WGM wave can have n wavelengths that explains the angular dependence of a WGM. Each n is called a mode number. In addition, the radial dependence of a WGM is characterized by the mode order l. Figure 1.9 shows the of distribution of mode intensity for a WGM with $n = 60$ (Figure 1.9a) and $l = 2$ (Figure 1.9b). As shown, the field intensity becomes weaker towards the center of particles and at $\sim r/N$ becomes insignificant. For the first order resonance ($l = 1$), the mode number is roughly calculated using the product of size parameter and refractive index.

Each set of n and l, there are a transverse electric (TE) mode with no radial electric field component, and a transverse magnetic (TM) mode with no radial magnetic field component.[41]

1.3.6 Aerosol-Radiation-Cloud Interactions

Radiative forcing (RF) has been defined and utilized as a metric to quantify the impacts of aerosols on climate. RF is expressed in watts per meter square and it is averaged and referred to a preindustrial year. It estimates the net change in radiation balance as a result of imposed agents. We note that the terminology used to describe the complex interactions of aerosols with radiation energy and clouds has changed in the recent IPCC report. To be consistent, we briefly go over this change in the following paragraph.

In general, the influence of anthropogenic aerosols on the shortwave and longwave radiative fluxes with excluding the could adjustments to the aerosol is called radiative forcing (RF). As a result, the direct influence of aerosols on climate, so called RF aerosol-radiation interactions (RFari), was previously considered only through scattering and absorption of radiation. Cloud adjustments to the scattering and absorption were referred to as the aerosol semi-direct effect. In addition, the indirect impact of aerosol on climate, the so called RF aerosol-cloud interactions (RFaci), was previously determined only through the number of droplet and ice crystal. This was also called the cloud-albedo effect. This definition excludes the mass concentration of liquid water and ice (previously called the cloud-lifetime effect). Two new terms ERFari (effective RFari) and ERFaci (effective RFaci) make up the total effective radiative forcing (ERF). ERFari incorporates the aerosol direct and semi-direct effects. Also, ERFaci involves the aerosol indirect effects including effects on the cloud microphysical processes and properties.[9,42]

The aerosol RF can be positive (warming) or negative (cooling) perturbations to the radiation energy balance. According to recent the IPCC report, ERF due to aerosol-radiation and aerosol-cloud interactions (excluding BC on snow and ice) is estimated to be about -0.9 W m^{-2} (medium confidence). This value can be divided almost equally between EFari and EFaci (each -0.45 W m^{-2}).

We mentioned earlier that the water vapor is the major GHG in the atmosphere and the number one contributor in the natural GHG effect. Natural evaporation is the dominant source of water vapor flux into the atmosphere. Therefore, water vapor is not considered an anthropogenic gas, although its GHG effect is two to three times larger than CO_2. Some anthropogenic emissions such as CH_4 can lead to more water vapor by oxidation and warming. However, this impact is not comparable to that of CH_4 and CO_2. Of course, the amount of water vapor in the atmosphere is mainly determined by air temperature rather than emissions.[9]

Aerosol-radiation interactions depend on the type of aerosol. Some particles such as pure sulfates, nitrates, and salt can reflect almost all incident radiation yielding a cooling effect. Some particles such as dust can exhibit different absorption and scattering properties if they

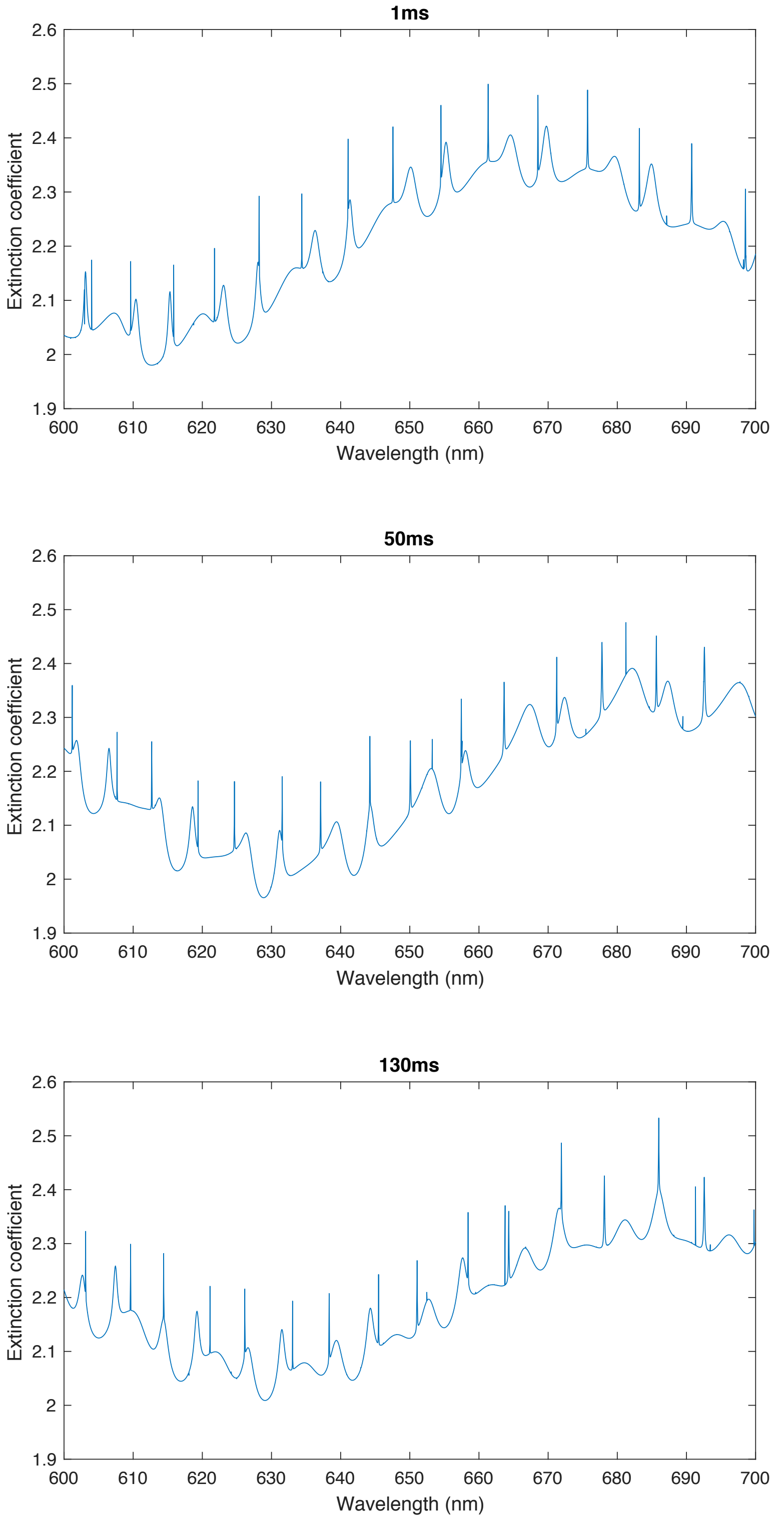

Figure 1.8: Extinction efficiency as a function of wavelength for a particle water sorption at RH= 0.65 at selected time steps.

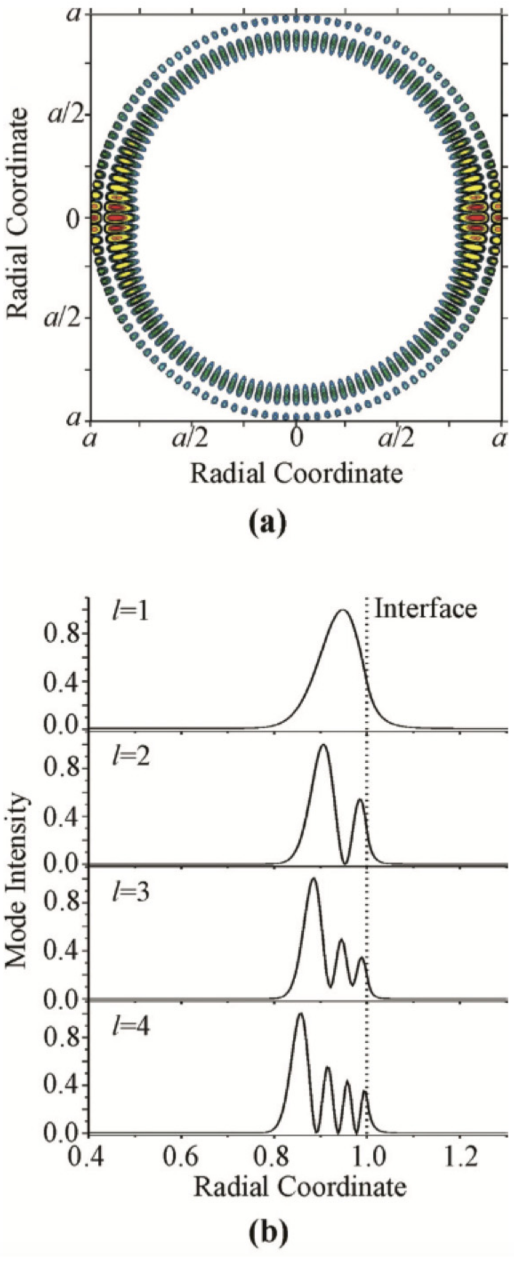

(a)

(b)

Figure 1.9: Illustration of (a) internal intensity distribution for a WGM with n=60 and l=2, calculated for a droplet of size parameter 53.3130188. (b) Influence of mode order on radial field (from Ref. 41)

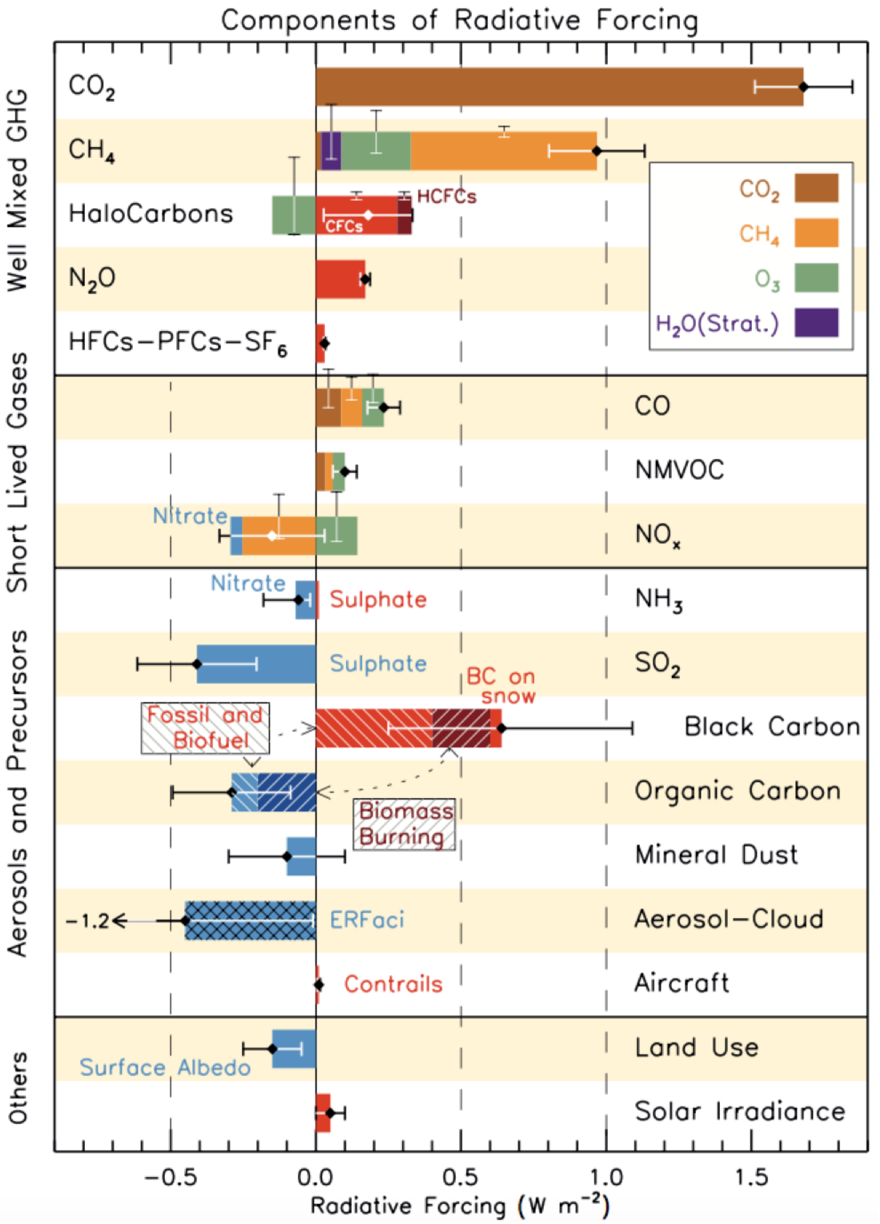

Figure 1.10: RF of the driving emitted compounds during 1750-2011 period (from Ref. 9)

are coated by darker materials like black or organic carbon. Deposition of dark aerosol particles such as soot or wildfire aerosols on bright surfaces like snow and glacier covers can drastically expedite the rate of snow and ice melting. This is an enormous threat to the future of fresh water resources as well as the environment in general.

Aerosol-cloud interactions has been the subject of many recent studies. Cloud properties, precipitation, and cloud radiative effects are all functions of aerosols. What makes the problem complicated is that atmospheric dynamics and thermodynamics control the cloud type, and aerosol-cloud interactions can significantly change from one cloud type to another. For instance, deep convective clouds are much more complex than the shallow maritime clouds. In a recent review by Fan et al.,[43] the latest findings of aerosol-cloud interactions mechanisms have been discussed. For warm boundary clouds, adding aerosols can increase cloud albedo, suppress the warm rain through coalescence-collision suppression, increase cloud lifetime and cloud cover. For mixed-phased clouds (supercooled liquid droplets and ice crystals together), aerosol can impact the cloud phase and lifetime through changing the water transformation especially by acting as IN. For deep convective clouds (mostly with warm-cloud base), aerosol can increase the release of latent heat by freezing additional cloud water. Also in these clouds, by acting as CCN, aerosols can greatly increase ice particle number but reduce ice particle size and fall velocity. For cirrus clouds, aerosol composition is key in IN process.[43] The impact of aerosol on clouds and consequently on radiation is quite complex and poorly represented in current climate models.

1.4 Atmospheric Remote Sensing

Atmospheric remote sensing is the process of acquiring knowledge and information about trace constituents in the atmosphere by sensing their interactions with electromagnetic radiation. In fact, the aerosol particles, water vapor and trace gases can change electromagnetic radiation by absorption, scattering, or emission and this change is detectable by the ground-based and satellite-baed instruments. Tropospheric and stratospheric remote sensing have been significantly advanced in the past years. The global and regional satellite remote sensing observations have enabled the modeling community to better represent aerosol processes in air quality and climate models.

1.4.1 Atmospheric Windows

The presence of constituents in the atmosphere can block the field of a space observer by strong absorption of electromagnetic radiation. Figure 1.11 shows the atmospheric absorption/transmittance spectrum over a wide range of the electromagnetic spectrum. As shown, H_2O, CO_2, and O_3 are the dominant absorbers in near-infrared and thermal spectral ranges. In contrast, in the visible region, the atmosphere is quite transparent mainly because visible light does not have an energy that corresponds to either electronic or vibrational transitions. Therefore, the principle gases (N_2, O_2) do not absorb the light. The transparent regions depicted in Figure 1.11 are called atmospheric windows. These windows allow satellite sensors to operate via aerosol-solar radiation interactions.

1.4.2 Principles of Satellite Remote Sensing

The basic principles of aerosol remote sensing using satellites is briefly discussed here using Ref. 44. In general, remote sensing of aerosols is easier over the dark surfaces such as the oceans. Because, the radiance at the top of the atmosphere (TOA) L_{TOA} would be only aerosol backscattering. The atmospheric reflectance is defined as:

$$R_{\text{atm}}(\mu, \phi, \mu_0, \phi_0) = \frac{\pi L_{\text{TOA}}(\mu, \phi, \mu_0, \phi_0)}{\mu_0 f} \tag{1.31}$$

where f is the extraterrestrial irradiance, (μ_0, ϕ_0) and (μ, ϕ) denote the sun and observation directions using μ the cosine of the zenith angle and ϕ the azimuth angle. The radiance parameter $L(\tau; \mu, \phi)$ should satisfy the radiative transfer equation:

$$\mu \frac{dL(\tau; \mu, \phi)}{d\tau} = L(\tau; \mu, \phi) - \frac{\omega(\tau)}{4\pi} \int_0^{2\pi} \int_{-1}^{+1} p(\tau; \mu, \phi; \mu', \phi') L(\tau; \mu', \phi') \, d\mu' \, d\phi' \tag{1.32}$$

where τ is the optical depth above the altitude z, $p(\tau; \mu, \phi; \mu', \phi')$ is the phase function at τ and for the scattering angle between (μ, ϕ) and (μ', ϕ') directions. Solution to Eq. 1.32 will result in obtaining radiance as a function of z and (μ, ϕ), if the radiative properties of aerosol are known. This is called forward problem in remote sensing. For L_{TOA}, $\tau = 0$ and $\mu > 0$. In inverse problems in remote sensing, we look to find the aerosol characteristics based on measured atmospheric reflectance or TOA radiance. Some aerosol properties retrieved by remote sensing are optical depth, size distribution, refractive index, and particle shape.[44]

Aerosol remote sensing over land is more complicated due to the combined radiance from both land surface and aerosols. If we assume that the surface reflects the light uniformly according to Lambert's cosine law and its surface reflectance is R_{surf}, then the observed reflectance

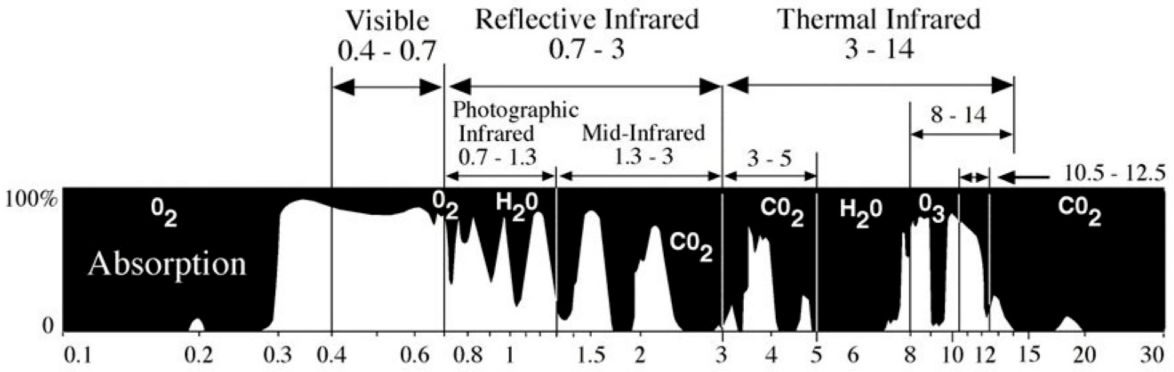

Figure 1.11: Atmospheric spectral signatures: The vertical axis is atmospheric transmittance and horizontal axis is the wavelength (μm).

is:

$$R_{\text{obs}}(\mu, \phi; \mu_0, \phi_0) = R_{\text{atm}}(\mu, \phi; \mu_0, \phi_0) + \frac{T_{\text{atm}}(\mu_0) T_{\text{atm}}(\mu) R_{\text{surf}}}{1 - R_{\text{surf}} R_{\text{atm}}} \tag{1.33}$$

where $T_{\text{atm}}(\mu_0)$ and $T_{\text{atm}}(\mu)$ are the total transmittance (direct and diffuse) of the atmosphere from the Sun to surface and from the surface to satellite respectively. T_{atm} is calculated using downward radiance (obtained from solution to Eq. 1.32) and R_{atm} is calculated by intergrating the atmospheric reflectance over both directions. For non-Lambertian surfaces, the surface bi-directional distribution function influences the surface-atmosphere interaction. It is important to do the atmospheric corrections to understand how much of TOA radiance is actually from the atmosphere or from the surface. The remote sensing aerosol products are validated using ground-based observation instruments such as sun-photometers or using airborne instruments.

1.4.3 Aerosol Remote Sensing

Historically, aerosol remote sensing has been done by active (lidars) or passive instruments. This classification is based on the radiation source to detect aerosol properties. In passive remote sensing, the source of energy is the sun or Earth's thermal emissions while in active remote sensing the source of energy is the instrument (e.g., laser). These remote sensing principles have been extended to satellite instruments with the aim of having a broader spatial coverage of atmospheric aerosols. The satellite platforms can be divided based on their orbit in two main groups: (i) low-orbit or sun-synchronous that cross the equator at the same local time and (ii) high-orbit or geo-stationary that rotate with the Earth to constantly look at the same geographic region. Satellite sensors can also operate at three angles: (a) nadir direction to analyze the vertical column of the atmosphere, (b) limb mode to analyze the light scattering by the Earth's rim, and (c) occultation mode to gain more information on vertical profile (Figure 1.12). In addition, some sensors are capable to scan with multi-view angles which can provide valuable aerosol retrievals such as aerosol phase function. The advantage of using multi-view instruments is that the land surface reflectance does not dominate the total reflectance in the image.[45]

The satellite remote sensing sensors can have different types of resolution to gather the data:

- spatial resolution that depends on the size of the field of view. It can vary from centimeters to thousand kilometers in grid space.
- spectral resolution that describes the number and width of spectral bands in spectrum that the sensor is capable of detecting. Airborne sensors can have hyper-spectral resolution (e.g. 224 bands in AVIRIS) while space-borne sensors are multi-spectral (e.g. 36 bands in MODIS).
- temporal resolution that states how often the sensor revisits the same geographical location and records the data. It can vary from few minutes to a couple of weeks.
- radiometric resolution that quantifies the sensitivity of sensor to subtle differences in electromagnetic radiation.

Current sensors with the ability to measure the aerosol properties are presented as follows:[45]

- AATSR (Advanced Along-Track Scanning Radiometer): Aerosol optical depth (AOD), angstrom exponent, aerosol mixing ratio
- AVHRR (Advanced Very High Resolution Radiometer): AOD
- CALIOP (Cloud-Aerosol Lidar with Orthogonal Polarization): AOD, profile of extinction cross-section
- GOME-2 (Global Ozone Monitoring Experiment-2): AOD, Absorbing Aerosol Index (AAI), species: O_3, NO_2, H_2O, BrO, OClO, SO_2

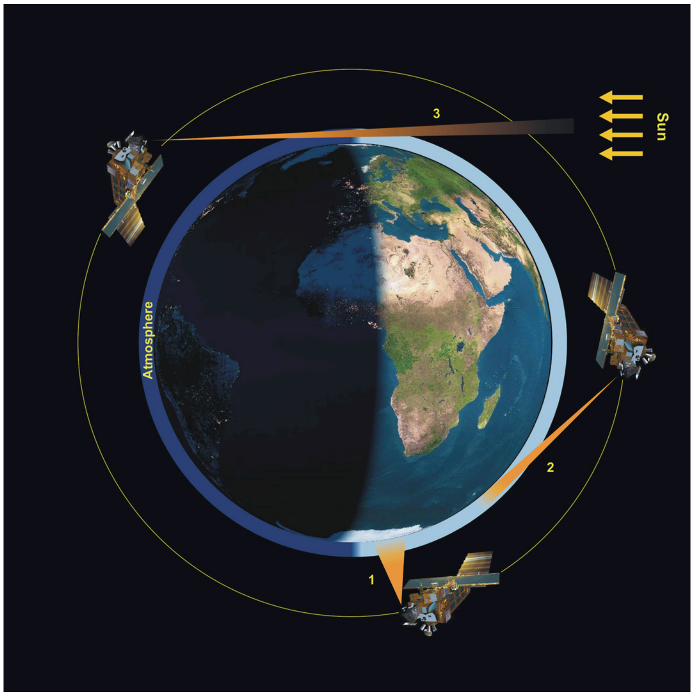

Figure 1.12: Observation modes for SCanning Imaging Absorption SpectroMeter for Atmospheric CHartographY (SCIAMACHY) sensor on ENVISAT platform: nadir (1), limb (2), occultation (3). The mission of this satellite ended in 2012 [http://atmos.caf.dlr.de/]

- MERIS (Medium Resolution Imaging Spectrometer for Passive Atmospheric Sounding): AOD, angstrom exponent, species: H_2O

- MODIS (Moderate Resolution Imaging Spectroradiometer): fine mode AOD, coarse mode AOD, single scattering albedo, angstrom exponent

- MISR (Multi-angle Imaging SpectroRadiometer): AOD 3-to-5 size bins, fraction non-spherical, qualitative single scattering albedo, plume top height

- OMI (Ozone Monitoring Instrument): AOD, AAI, species: O_3, NO_2, SO_2, BrO, OClO, HCHO, CHOCHO, O_4

- SEVIRI (Spinning Enhanced Visible and InfraRed Imager): AOD

- SeaWiFS (Sea-viewing Wide Field-of-View Sensor): Aerosol optical thickness (AOT)

- TOMS (Total Ozone Monitoring Spectrometer): AOD, species: O_3, SO_2,

In the present study, we use MODIS and MISR data. Both sensors are on Terra platform. MODIS sensor is also on Aqua satellite. The details about these two sensors discussed in chapter 2.

This thesis involves two main research themes in the field of atmospheric chemistry: (1) remote sensing of dust storms in the Middle East and (2) studying diffusion of water in viscous particles. Hence, background and motivation for each research track is presented in this chapter.

1.5 Dust Storms in the Middle East

Atmospheric aerosols can play a critical role in the Earth's biogeochemical cycles (e.g. conveying nutrients into marine ecosystems[9]) and global climate system (e.g. transferring radiation[46]) and have important social and economical impacts (e.g. on public health,[47] visibility[48]). Despite recent profound scientific advancements, their complexity, dynamics and many sophisticated interactions with other systems keep posing new questions and challenges to researchers today.

Dust aerosol can consist of different combinations of minerals. Major minerals in atmospheric dust are iron oxides and clays (mostly regulate radiation absorption in shortwave), quartz, calcite, gypsum, chlorite, feldspar (control radiation absorption in longwave).[49] The dust composition can be attributed to its source point. This has encouraged researchers to use bottom-up approaches and create high-resolution mineralogical databases of dust-productive soils for atmospheric dust modeling.[50] However, dust composition can change as it travels in the atmosphere. This makes it difficult to only rely on a bottom-up approach.

The morphology of dust aerosols is intricate. They can have variety of shapes and can absorb sunlight at wavelengths from ultraviolet to infrared.[44] Dust particles are typically hydrophobic and stay non-spherical in the atmosphere. Their unique optical properties has allowed us to probe the composition of these aerosols using top-down approach. In this method, the satellite signals from scattering light by dust are correlated to the mineral composition. Another application of this method is in mapping the potential dust source regions, for instance in Africa and Asia.[51]

Atmospheric dust can have various sources. The dominant source are semi-dry and dessert regions on Earth from where mesoscale and synoptically-driven dust storms can transport minerals to other locations. Depending on the dust composition and intensity of storm, dust storms

Figure 1.13: Dust storm occurred on Feb 18, 2017 over Persian Gulf. The left panel shows the dust plume spreading over several countries and its front that moves towards the southeast (http://eoimages.gsfc.nasa.gov). On the right side, photos show how this storm impacts people in Ahvaz, on the border of Iran and Iraq (source: Tehran Press and Mehr News).

can cause serious climatic, environmental, and heath issues (see chapters 2 and 3). Therefore, it is important to increase our understanding of atmospheric dust sources, magnitude, and evolution on regional and global scales.

Middle East has been hit by massive and more frequent dust storms in recent years. Figure 1.13 shows a very recent storm both from space and on the ground. As illustrated, these storms spread a thick blanket of mineral particles over several countries and can reach Himalayan Glaciers. Typically, the environmental agencies report an increase of the concentration of PM_{10} up to 10,000 $\mu g/m^3$, more than 65 times greater than standard daily average. With visibility less than 100 meters, lots of people die in accidents or just breathing the polluted air. There are uncertainties in what chemicals or bacteria these particle carry during their transport and how much Middle East dust storms contribute in global diffusion of pathogenic microorganisms. These extreme episodes of dust have raised key questions on the dust origins and on role of human on activity of these sources.

Despite research efforts and advances over the past years, we are still uncertain about the location of dust sources in the Middle East. Full background is presented in chapters 2 and 3. Another remaining question is how these sources can produce dust storms at unprecedented intensity and frequency in the region. These have been two main motivations for the first part of this thesis. Finding responses to the above questions will certainly help in better quantification and representation of Middle East dust in regional and global atmospheric models.

1.6 Water Diffusion in Viscous Aerosols

A significant fraction of the total mass of atmospheric aerosols in the troposphere is organic compounds.[52] Under sufficient oxidation of gaseous precursors in the atmosphere, these compounds can form a new generation of particles; so called secondary organic aerosol (SOA).[203] Researchers report that the formation and evolution of SOAs is not well understood[54] as they undergo chemical reactions, gas-phase and particle-phase mass transport, and transformation of matter.[55]

The hygroscopic growth of SOAs has recently gained a lot of attention as it can change the physical characteristics of an aerosol. One example is changes in SOA concentration and resulting optical properties. This can have important implications for the SOAs direct and indirect effects on the Earth's energy balance. The magnitude of SOAs influence on global radiative forcing can be comparable to other types of atmospheric aerosols.[9] This has lately encouraged researchers to investigate the relationships between the SOA hygroscopicity, compositional changes, and optical properties. For example, Denjean et al., 2015 studied the simultaneous evolution of hygroscopicity and optical properties of SOA generated from ozonolysis of α-pinene. In that work, SOA hygroscopicity is estimated by measuring the effect of relative humidity on the particle size (using a defined size growth factor) and on the scattering coefficient (using a defined scattering enhancement factor). Their results suggest glassy SOAs slows down changes in RI and size with RH.[56] The hygroscopic growth of SOAs can also involve multiphase reactions which can greatly enhance the light scattering and increase the direct radiative forcing by SOAs.[57]

As described before, the complex refractive index (RI) is an essential and inherent optical property of aerosol.[58] A review by Moise et al., 2015 concludes that almost all SOAs efficiently scatter the visible (400-700 nm) and near infrared (700-2500 nm) radiation, with a RI range of 1.35-1.60. Therefore, they are assumed to be only light-scattering constituents in the current global climate models.[59] This means that SOAs are weak absorbers so the imaginary part of refractive index can be negligible. It was also mentioned before that since the interaction of incident light with particles of the same shape and RI does not depend on scale, particle size is expressed by the dimensionless size parameter.[58] Change in particle size as a function of RH has enabled us to better discover the link between aerosol hygroscopicity and its optical properties.

Recent studies have shown that depending on the composition and ambient conditions, SOAs can be present in amorphous (non-crystalline) semi-solid or solid states.[60–65] This leads to the formation of glassy aerosols. This is due to the fact that the water-soluble organic component of SOAs can escape crystallization and form highly viscous liquids[66] when underging a fast cooling process.[67] In the metastable regime, called the supercooled phase, time scales jump up to several orders of magnitudes greater than microscopic time scales at the glass transition temperature (T_g).[68] The slow evolution of physical properties with time then occurs far out of equilibrium with the surroundings, known as the aging process.[69] Consequently, the glass transition is not a thermodynamic process since everything depends on time.[70] Figure 1.14 shows the diffusion lifetime of three different particle types: solid, semisolid, and liquid as a function of particle diffusion coefficient and size. In the middle of this panel, the light green arrow shows that the diffusion lifetime for the atmospheric aerosols in accumulation mode can greatly vary in time as the corresponding diffusion coefficient changes over orders of magnitudes in this region.

The existence of SOAs in a glassy state can result in significant kinetic limitation and change hygroscopic behavior of SOAs.[16,72,73] This can impact the single scattering albedo and optical depth of SOAs as two key factors in determining the the SOA direct effect.[74,75] In addition, a growing body of research indicates that heterogeneous ice nucleation of glassy SOAs in both form of deposition and immersion states can play a critical part in cirrus cloud

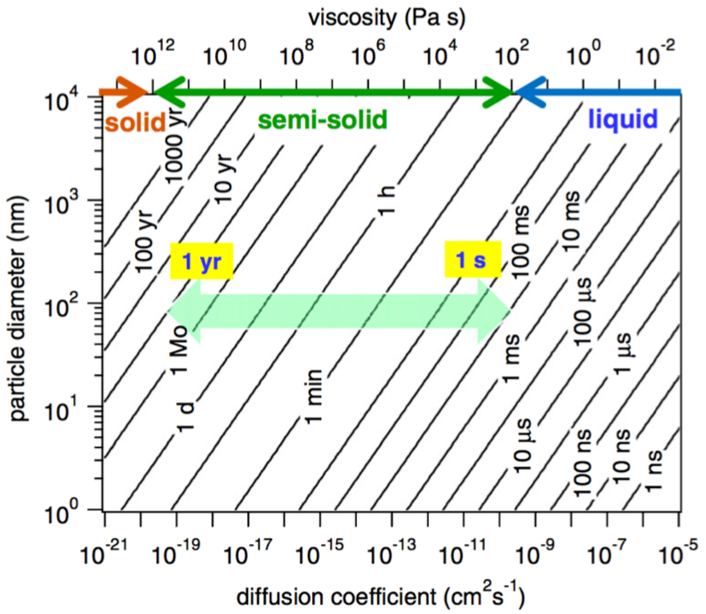

Figure 1.14: Diffusion lifetime in liquid, semisolid and solid particles as a function of particle diffusion coefficient and size (from Ref. 71).

formation.[76–78] This effect is important in formation of ice clouds in the tropopause layer (altitude 1-12 km, temperature 180-200 K) and can provide clarification for the low ice crystal numbers and high in-cloud humidity in this part of the atmosphere.[77] Thus, the glassy state can potentially impact the indirect aerosol-cloud effects as well.

Different laboratory techniques have been used to measure the water diffusion coefficient (D_{H2O}) in humidifying and drying processes of glassy particles. The most common ones are the Stokes-Einstein relation at room temperatures,[61–64] and electrodynamic balance (EDB) at lower temperatures.[15,16,79–81] At temperatures near 1.2 T_g or higher, the diffusivity and viscosity decouples and hence D_{H2O} obtained from the Stokes-Einstein technique may deviate and have lower values by orders of magnitude compared to the observation.[62,82] Under these conditions, this technique will fail to distinguish the diffusion of different constituents in solution.[81] Due to experimental constraints, water diffusivity in SOA particles is derived from water diffusivity parameterizations of model compounds by applying a semi-empirical physico-chemical model of water diffusion in glass-forming aqueous organics.[73] The aqueous carbohydrate systems can serve as a model of the main components of atmospheric particles and water diffusion coefficients of a few of them such as the sucrose system have been experimentally estimated in the glassy state.[15] Up until now, direct parameterization of water diffusivity (as a function of temperature and composition) has been achieved for few aqueous systems including sucrose[73], citric acid[80], and shikimic acid[83].

Studying aerosols on the single-particle level is appealing to many researchers since it can provide physical parameters retrieved from measurements with a high degree of precision.[84–89] Measuring water sorption/desorption from single particle[15,80,81,83,90–92] as well as isotopic water exchange measurements[93–95] have helped to retrieve diffusion coefficients for water in glassy SOAs. Researchers have also developed kinetic flux models to couple the diffusion and reaction of multiple species in the aerosol particles.[96–98] However, solving the associated equations numerically is time consuming when varying parameters to fit experimental data.[99,100]

This has motivated us to focus on the mathematical physics of the diffusion problem in greater detail. We aim to derive exact solutions to the isotopic water exchange problem and compare the results with numerical schemes.

Additionally, it has been recently reported that viscous SOAs can adopt core-shell morphology that can influence resonance behavior in the elastic light scattering.[101] Figure 1.15 shows different possibilities in a water sorption/desorption process for an atmospheric aerosol. Panel (c) on this figure depicts formation of a core-shell morphology for an amorphous particle. If the SOA becomes non-homogeneous in composition, it does not allow us to directly apply Mie scattering theory to characterize the size and refractive index of the SOA. Therefore, a study of the light scattering by non-homogeneous SOAs on the single-particle level is needed to further explore the complex compositional dependence of SOA scattering efficiency. This is the motivation for the last part of this thesis. We simultaneously model the full non-linear diffusion and light scattering in spherical particles. The new knowledge will contribute to a better representation and parameterization of SOAs in atmospheric chemistry and climate models.[58]

1.7 Thesis Overview

As mentioned earlier, the focus of this thesis will be on regional-scaled studies of mineral dust aerosols (Chapters 2 and 3) and on water diffusion in viscous aerosols (Chapters 4 and 5).

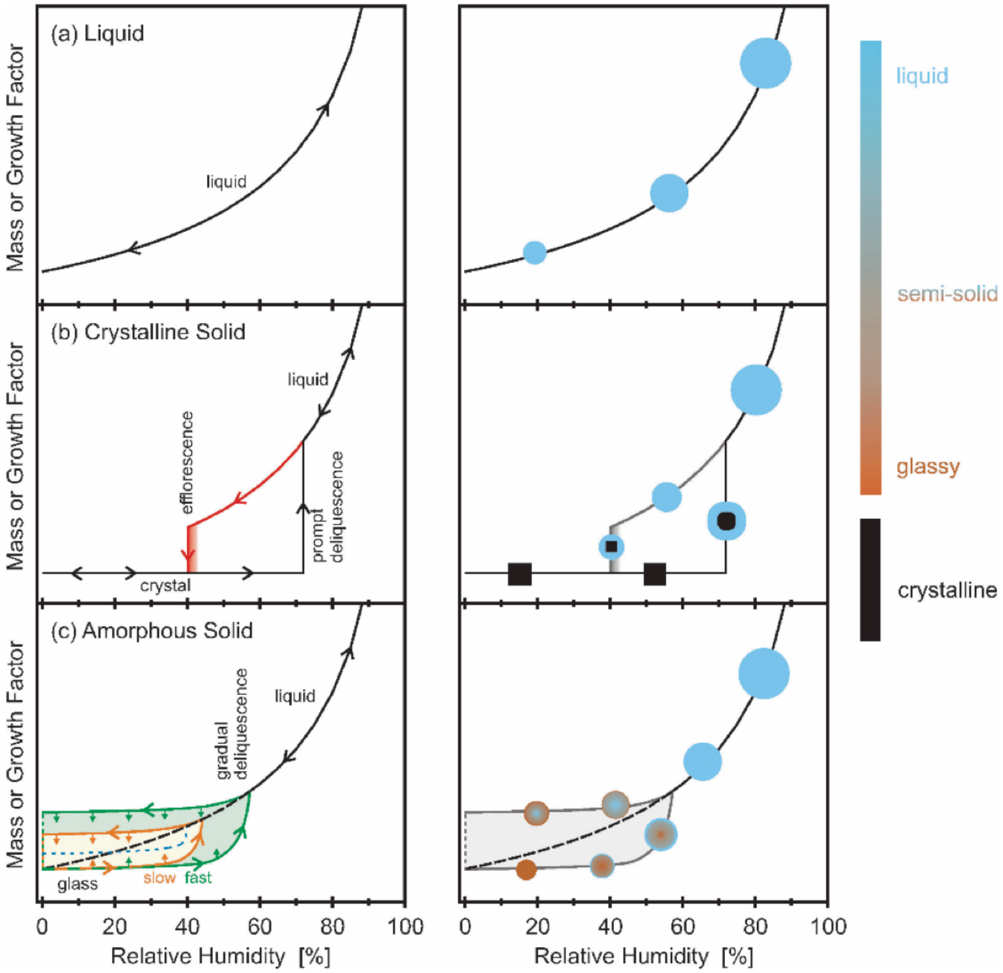

Figure 1.15: Water diffusion in atmospheric aerosol particles (a) liquid with negligible vapor pressure, (b) crystalline solid with deliquescence and efflorescence, (c) amorphous solid with humidity-induced glass transition (from Ref. 102)

In Chapter 2, a new high resolution mapping of major atmospheric dust source points in the Middle East region is studied. MODIS data are used to compare several dust retrieval algorithms. We apply a new approach to identify dust storms by a combination of the visible (VIS) and thermal infrared (TIR) bands, and to map and classify the source points in the study area. Chapter 2 also discusses the findings of this study and compare them to the previous literature.

The identified dust source points are discussed in much more detail in Chapter 3, with a major focus on dust sources that are located in Iraq and Syria. We attempt to understand the desertification and land use changes in the study area and its relationship to dust storms.

This is done through spectral mixture analysis of the Landsat TM images (1984 and 2012). The desertification map identified through change detection analysis is derived and discussed in details. Later, this map is overlaid on the identified atmospheric dust source points in the Middle East region found in the earlier chapter. The full result and discussion of this comparison is presented at the end of Chapter 3.

Chapter 4 describes a mathematical formulation of the water exchange diffusion problem and presents analytical solutions for this problem in a spherical particle. The goal is to provide insight into the role the surface boundary condition plays in modeling the isotopic exchange experiment. Two different boundary conditions are studied: (1) liquid and water in equilibrium at the surface and (2) constant surface concentration. We further explore these results using three physical examples of binary solution droplets: aqueous sucrose, aqueous citric acid, and aqueous shikimic acid droplets. Using the two derived analytical models, we study the water exchange lifetime as well. This study suggests assumptions regarding physical conditions can significantly impact the water exchange lifetime for a particle to achieve equilibrium with its surroundings at high RH.

Understanding nonlinear diffusion is the main subject of Chapter 5. Specifically, we investigate diffusion and light scattering of core-shell particles. We use aqueous sucrose droplets as the model system to test the particle hygroscopicity and optical behavior under different environmental conditions. The MDRs present in spectra of single spherical particle are discussed. Also, the numerical scheme describing the diffusion model as well as parameterization for the diffusivity, density, and water activity of aqueous sucrose are presented in detail. A new equation for the resonance condition of a spherical core-shell particle is described later in this chapter. We discuss the diffusion front and morphology of particle under varying RHs. Next, the effect of the morphology on scattering resonances is explained. We discuss this further by comparing the results of recent studies on single-particle light scattering modeling and measurements to findings of the current work. Finally, we evaluate and discuss tracking the diffusion front using optical spectra measured during water uptake.

Chapter 2

A New Inventory for Middle East Dust Source Points

Abstract

We use the Moderate Resolution Imaging Spectroradiometer (MODIS) sensor on both Terra and Aqua satellites to present new high-resolution mapping of major atmospheric dust source points in the Middle East region on the basis of the improved version of the recently developed Middle East Dust Index (MEDI) applied to 70 dust storms, which occurred during the period between 2001 and 2012. Results indicate that 247 different source points have participated in dust storm generation in the Middle East region in which Iraq and Syria are the most efficient regions for dust storm generation in this region, respectively. Using extracted indices for the Deep Blue algorithm, identified dust sources were classified into three levels of intensity. The frequency of occurrence approach, the relationship between high atmospheric dust content and its number of occurrences, is also used to identify sensitive source points. High-intensity dust storms are mainly located west of Iraq and near the border of Iraq and Syria. We will discuss the implications of our results in understanding the global dust cycle.

2.1 Introduction

One of the important areas of research in atmospheric dust is its source identification. In fact, knowledge of dust sources such as geographical locations, geomorphological features, emission rate, and the degree of activity are basic factors in understanding the influence of dust on human life, climate, hydrological cycle, ecosystem, and economy[103] Several studies, as reviewed by Xuan et al.,[104] have located the dust sources using (a) surface conditions (e.g., soil moisture, vegetation cover, soil texture, surface roughness, and topography) and/or (b) dust features (e.g., frequency based on visibility reduction, dust emission rate, and satellite image products).

Since dust source points are often immense and in distant areas where there is little or no human activity, various remotely operated methods have been employed in identifying dust source points. Schepanski et al.[103] categorized all source point identification methods into four general approaches; (1) mineralogy of dust samples, (2) satellite remote sensing techniques, (3) horizontal visibility, and (4) Lagrangian back-trajectory. Satellite observations provide near-daily global data with valuable retrievals on aerosol properties, implemented in dust source localization over arid and semi-arid regions.[105] Different approaches have been developed with regard to satellite sensor band identification. For instance, aerosol retrievals both over land and water from the Total Ozone Mapping Spectrometer (TOMS) sensor on the Nimbus 7 satellite are extracted using satellite radiance in the Ultraviolet (UV) spectral region. These products are based on a quantity known as the aerosol index (AI) derived by Herman et al.[106] Using TOMS AI, Prospero et al.[107] have shown that major atmospheric dust sources are located in topographical lows in arid and semi-arid regions with annual rainfall less than 200-250 mm in the so-called dust belt. In such areas, deep alluvial deposits were formed by intermittent flooding, through the Quaternary and into the Holocene.[107] These sources are located in arid or hyper-arid regions. The Ozone Monitoring Instrument (OMI) sensor on board the Aura sun-synchronous satellite provides UV high-resolution data compared to TOMS data, which makes it possible to detect of dust sources through UV bands.[108] Another characterization method is based on analysis within the infrared spectral region. In an example of the infrared method, Schepanski et al.[109] used the Spinning Enhanced Visible and InfraRed Imager (SEVIRI) on board the Meteosat Second Generation (MSG) geostationary satellite, which has 15 min. time resolution with a spatial resolution of 3 km × 3 km at nadir, and thereby developed a qualitative 15-minute MSG InfraRed (IR) dust index. The IR dust index using three different IR channels (8.7 μm, 10.8 μm, and 12 μm) was utilized to derive a new Saharan dust source map.[109] Brooks and Legards[110] have previously employed Infrared Difference Dust Index (IDDI), another dust product designed specifically for the remote sensing of dust in arid regions[111] from the IR imagery of Meteosat, and identified the Bodele depression (a major source of dust over north Africa), some parts of Mauritania, Mali, and southern Algeria, as dust source regions.

Using 5 years (2001-2005) of dust enhancement product imagery for southwest Asia and the Coupled Ocean/Atmosphere Mesoscale Prediction System (COAMPS), Walker et al.[112] were able to accurately model the evolution of individual dust plumes and better forecast the onset and end of dust storm occurrence.

Schepanski et al.[103] have compared common satellite remote sensing products for inferring dust source area identifications including MSG IR dust index, Aura OMI AI, and Moderate Resolution Imaging Spectroradiometer (MODIS) deep blue aerosol optical thickness (AOT) data over the Saharan desert. Furthermore, two different approaches of dust source identification, back-tracking individual dust plumes method applied to 15-min MSG IR dust index as well as the frequency of occurrence of high dust plumes, applied to daily OMI AI. Significant differences in the spatial distribution of inferred dust source regions have been observed. The temporal resolution of satellite dust products has been identified as an important factor used to decipher dust source regions.[103]

We herein aimed to evaluate the (a) location of dust source points and (b) frequencies of dust storms and their classification in terms of intensity and participation in dust storm generation. We applied Middle East Dust Index (MEDI),[113] which was developed based on the strengths and weaknesses of four existing dust source identification methods to provide a comprehensive picture of source points in the region.

2.2 Study Region

The Middle East, which consists mainly of the Arabian Plateau and the Tigris-Euphrates Basin, is an active wind erosion region in the world.[114] The area of desert, which stretches across Iraq, Iran, Afghanistan, Pakistan, and northwest India, has long been recognized as a source of atmospheric mineral dust.[115,116]

There are four dominant climate systems in the Middle East: (1) the Siberian anticyclone over central Asia in winter; (2) the Polar anticyclone over east of Europe and the Mediterranean Sea in the summer; (3) the monsoon cyclones over the Indian subcontinent, the south and southeast of Iran and the southeast of the Arabian peninsula, in the summer; (4) the depressions traveling from northern Africa and southern and east regions of the Mediterranean sea across the Middle East and southwestern Asia in the spring and winter.[117] Two winds in particular generate dust in the region: The Shamal wind, from mid-June to mid-September, creates severe summer Shamal dust storms and prefrontal and postfrontal winds which generate frontal dust storms in other seasons.[118]

Generally, in the Middle Eastern countries, the climate is typically dry, with very little annual rainfall. The southern part of this region has a desert climate with hot, dry summers and mild winters. In the mountainous Iranian and Turkish border, winters can be harsh with frost and heavy snowfall. Sudden hot spells are a unique winter feature in such countries. Although dust storms are common during the summer, few dust events can happen during the winter in the Middle East region, which have also been significantly increasing recently.[113]

Each year, dust storms force businesses to shutter several days to lessen their negative effects on peoples health. Determination of the location of dust storm sources affecting the countries could help decision makers take appropriate measures to lessen the severity of the effects of the dust storms. One of the important challenges, however, is to detect the dust plumes on the brilliant desert surfaces, where dust originates.

Due to the large extent of the Middle East, only the areas which affect the west, southwest and northwestern part of Iran were analyzed (this includes Iraq, Syria, Saudi Arabia, Jordan, and parts of the southwest and the western Iran). Therefore, dust sources identified are limited only to this part of the Middle East.

2.3 Methodology

2.3.1 Data Description

In the present study, the MODIS data were used to compare several dust retrieval algorithms, applying a new approach to identify dust storms by a combination of the visible (VIS) and thermal infrared (TIR) bands, and to map and classify the source points in the study area. This sensor makes observations using 36 bands with wavelengths ranging from 0.41 to 14.4 μm and nadir spatial resolution of 0.25, 0.5, and 1 km. MODIS is operating onboard the NASA Earth Observing System (EOS) Terra and Aqua satellites, launched in December 1999 and May 2002, respectively. In this study, MODIS data were obtained from the level 1 Atmosphere Archived and Distribution System (http://ladsweb.nascom.nasa.gov) and processed to convert the digital numbers into radiometrically calibrated and geo-located data products.

Daily MODIS Level 2 Aerosol data have also been used. These data are produced at spatial resolutions of about 10×10 km pixel array. There are two types of MODIS aerosol data files: MOD04_L2 (which contains data from the Terra platform) and MYD04_L2 (which contains data from the Aqua platform). Here, only the MYD04_L2 product was used as the latest Deep Blue retrievals are not yet available for the Terra platform and this restrictive parameter prompted us to utilize the Aqua images in this study.

As a first step in dust source identification, all the daily images of the study area from 2001 to 2012 were visually evaluated and only the images in which the dust events occurred were selected. In addition, daily Deep Blue products were used to increase the accuracy of the event identification. The Deep Blue algorithm employs different processes applied to MODIS data to retrieve aerosol over land. Indeed, Deep Blue uses the dark-target approach[119] and assumes that the ratio of surface reflectance between 0.47 μm and 2.1 μm is 0.25. For most vegetated land surfaces, this assumption is assumed to be valid.[120] Yet, over desert regions, this assumption is significantly flawed. The Deep Blue algorithm claims that it can alleviate these problems in detecting aerosol properties over bright surfaces by employing radiances from the blue channels of the MODIS sensor, where surface reflectance is low enough to make retrievals possible. The result of the Deep Blue algorithm over the bright surfaces of the Middle

East deserts was examined in this study. MODIS Deep Blue data within MYD04_L2 includes Aerosol Optical Thickness (AOT) (τ) determination at 0.412, 0.47, 0.55, and 0.66 μm - only the 0.412 μm data were used. The typical AOT for visible light in clear air is 0.1, and for very hazy situations it is AOT ≥ 0.3.

The result led to the identification of 70 major dust events in the 12-year period. Consequently, in the present study, 70 MODIS images corresponding to these events were acquired and analyzed from both Terra and Aqua satellites based on the start of the dust storms. The wind speed and direction for each event were retrieved from the National Centers for Environmental Prediction (NCEP)/National Center for Atmospheric Research (NCAR) which produces regular weather forecasts as well as reanalysis of older data to generate consistent meteorological information. The main properties of the reanalysis dataset used in this study are $2.5^\circ \times 2.5^\circ$ horizontal resolution, 0.995 sigma vertical levels, and 6-h temporal resolution.

2.3.2 Methods

This section has two parts: (a) the source identification algorithm based on the revised version of MEDI. The detailed information of MEDI is described elsewhere;[113] and (b) dust source classification and frequency of occurrence methods, by joining the Deep Blue algorithm to the revised version of MEDI.

2.3.2.1 Dust Source Detection Algorithm

A number of studies have used brightness temperature changes between mineral aerosols and land surfaces to distinguish them from each other.[121,122] The use of single TIR has had limited success due to the changes in surface emissivity.[123,124] Because of this limitation, as well as the emissive variability and the transmissive properties of mineral particles within multi-TIR ranges, several algorithms have been invented based on the brightness temperature difference (BTD), as bi-spectral split window techniques. BTD is based on temperature differences between the ground surface and cooler mineral aerosols while at the same time are largely unaffected by absorption from other atmospheric gases.[125]

The dust source identification method in this study is based on the new model called MEDI retrieved in the previous work by Karimi et al.[113] In MEDI, four major dust source identification models (Ackermans model, Roskovenesky and Liou algorithm, Normalized Difference Dust Index (NDDI), Deep Blue algorithm) were analyzed and compared within the study region, and the advantages and shortcomings were evaluated. To analyze the performance of different MODIS dust retrieval methods in identifying source points, three dust events, all originating in the Middle East region, were studied. Several factors, which can significantly affect dust plume and source identification, have also been included in MEDI, namely, single or multiple dust plumes and multi-mineralogical dust plumes. In addition to the satellite-based algorithms, the HYbrid Single-Particle Lagrangian Integrated Trajectory (HYSPLIT) model was used to recognize dust sources in each event separately.

2.3.2.2 Dust Source Classification Method

In the current study, in addition to the MEDI model, wind speed and direction and Deep Blue products were used in the dust source identification process. Deep Blue products were used since the majority of the individual Middle East dust storms selected consisted of several source points (multi-source dust storms) (Figure. 2.1a). Note that not all these sources equally participate in the generation of dust storms. Consequently, Deep Blue products were employed here to classify source points intensities. If the value of Deep Blue AOD varied between 0.6 and 0.75, the source point was categorized as low intensity. In the range was 0.75 to 0.85, it was characterized as medium intensity. For AOD values higher than 0.85, the dust source point is classified as high intensity. These thresholds were found based on the maximum area coverage by dust plume for each event and the mean, maximum, minimum, and standard deviation of AOD for each dust sources. Figure. 2.1, represents an example of this analysis for a severe storm that occurred on January 21, 2010 in the study region. Identified dust sources were classified into three levels, in terms of intensity: low, medium, and high. As illustrated in MODIS true color image (Figure. 2.1a), the major parts of central and eastern Iraq and western and southwestern Iran experience this type of storm. After implementing MEDI on this storm, it was found that this event is a result of combining 15 separate source points with different levels of intensity (Figure. 2.1b). Notably, there are 5 low-intensity points in eastern Syria, 4 high-intensity and 3 low-intensity sources in northern Iraq, and 1 high-intensity and 1 low-intensity source in the southeastern Iraq.

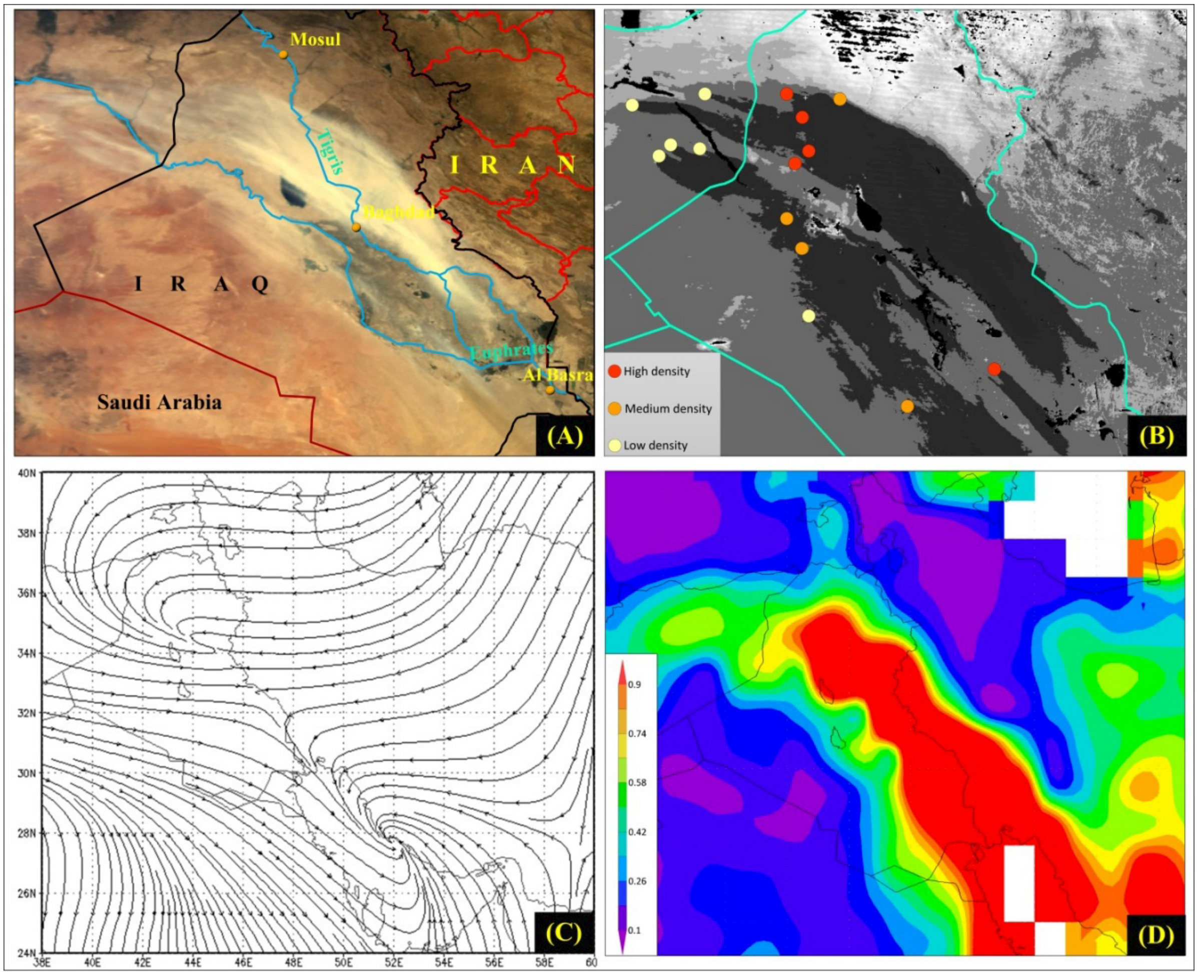

Figure 2.1: (a) MODIS true color image of 21 June 2010, (b) the result of MEDI algorithm and identified dust sources, (c) wind direction map, and (d) the result of AOD of Deep Blue algorithm with spatial resolution of about 0.1°×0.1°.

The frequency of occurrence approach was applied to classify the identified sources. In the frequency method, a relationship between high atmospheric dust content and the number of occurrence is presumed. Researchers have previously used this method to identify dust source regions[105,107] or to distinguish anthropogenic sources and natural sources[105] from daily (sun-synchronous) satellite products. In fact, it has been assumed that high dust column loads occurred over source regions more frequently than those in other areas.[103] Based on this method, frequency of AOD value was hence computed.

2.4 Results and Discussion

2.4.1 Spatial Patterns of Source Points

As described in the previous sections, dust source identification was carried out by applying the presented methodology on 70 dust storms, which occurred in the Middle East in the period between 2001 and 2012. Results indicate that 367 different source points have participated in dust storm generation in the region. Distribution of these sources is shown in Figure 2.2, which also depicts the highest concentration of dust source points, identified as occurring in central and western parts of Iraq and east of Syria. This area is called Neinava and is shown with a yellow circle in Figure. 2.2. On the contrary, the source points in Iran and Saudi Arabia do not follow a special pattern and are spread out.

Although the number of source points can be an indicator of sensitive areas for dust generation, it cannot be the sole factor in identifying the hot spots. In Syria, the source point surface area is significantly higher than the area of source points in Saudi Arabia. Iraq has the maximum surface area occupied by dust sources in the region. According to the spatial classification, it can be concluded that Neinava contains the largest portion of dust source area in the Middle East (yellow circle highlighted in Figure. 2.2). However, there is another important region in southern and southeastern parts of Iraq (green circle shown in Figure. 2.2), which includes a considerable area of all detected source points. Although the absolute number of source points in this region does not have a high frequency, it has a large area of dust sources.

Another index, which can be used in identifying sensitive source points, is dust event frequency of occurrence from each specific source point. One specific source point, which has a large area, may not necessarily have a significant role in dust storm emissions during the year. Therefore, all the identified dust source points during the 12-year period were also carefully analyzed on the basis of their frequency of occurrence. Results of this analysis are presented in Figure. 2.3a. By comparing Figure. 2.2 and Figure. 2.3a, it can be found that the area of a source point is directly related to its frequency of occurrence; hence, larger areas of source points also have a higher frequency of occurrence and vice versa. Source points located in

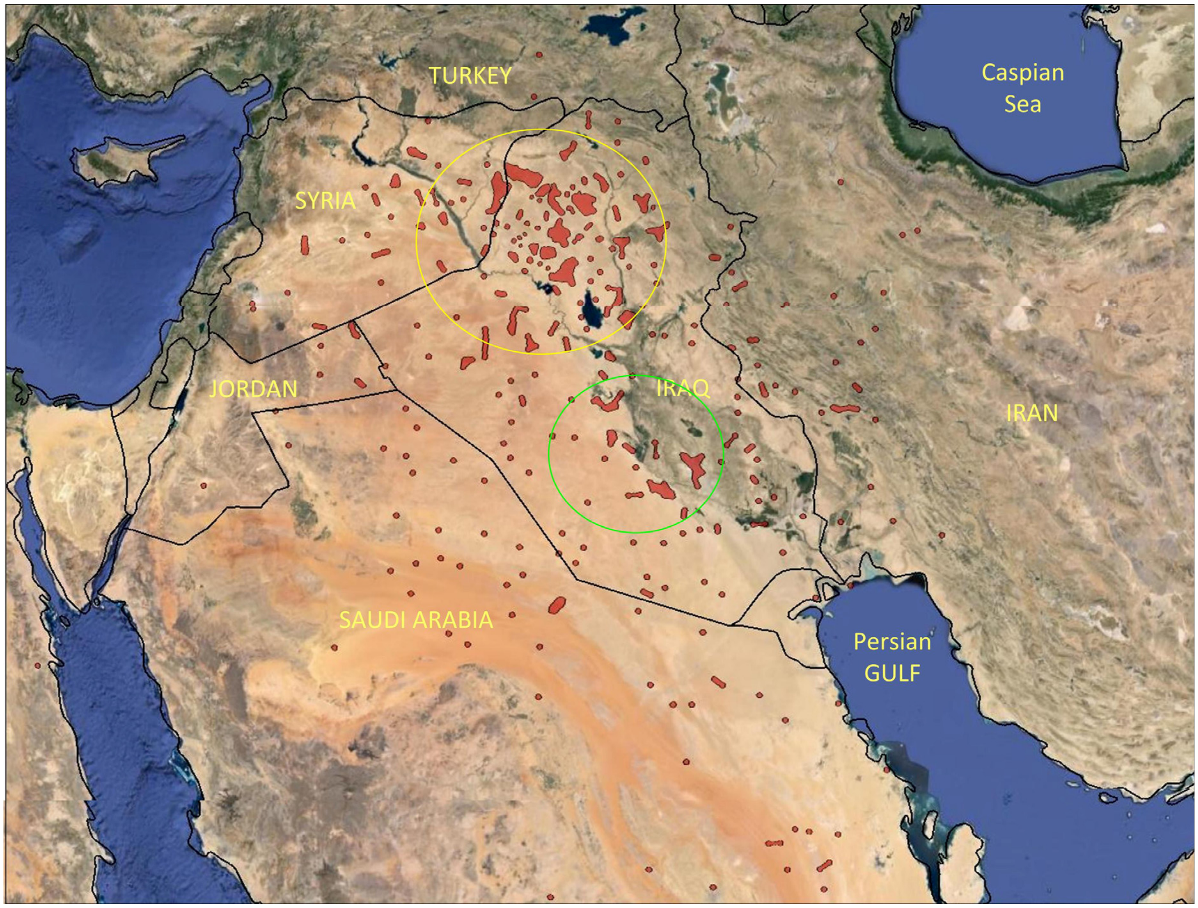

Figure 2.2: Spatial distribution of dust sources identified from MEDI algorithm over Middle East region.

the central and western parts of Iraq and in eastern parts of Syria have the highest frequency of occurrence. These regions were identified as having the highest number of source points and the maximum area occupied by dust sources. In addition, similar to the result of area categorization, there are some source points with a frequency of more than 13 times in the south and southwest of Iraq, which have a significant number of source points relative to other identified regions.

2.4.2 Dust Source Classification

As described in the Methodology section, intensity is one of the factors considered important in this study of dust source point classification. Using extracted indices for Deep Blue algorithm, identified dust sources were classified into three levels, in terms of intensity: low, medium, and high. Thus, source points can be interpreted in terms of their intensity. Frequency of occurrence approach was applied to classify the identified sources. In the frequency method, a relationship between high atmospheric dust content and its number of occurrences is presumed. Several researchers have previously used this method to identify dust source regions[105,107] or distinguish anthropogenic sources and natural sources[105] from daily (sun-synchronous) satellite products. In fact, it is deduced that high dust column loads occurred over source regions more frequently than those on the other areas.[103]

Of note is that a strong relationship between dust source intensity and source area or its frequency may not always be established. Many dust source points have a large area and high frequency of occurrence; however, they may not yet produce highly intense dust storms due to factors such as general atmospheric circulation, land topography and geomorphology, and meteorological conditions. Based on different climate and weather conditions, a specific source point can generate dust storms with varying intensity during various time periods. It can reasonably be assumed that a specific source can produce relatively similar intensity dust storms, providing that climate and weather conditions remain unchanged. One source may thus generate dust storms with similar intensity under fixed climate and weather conditions. Figure. 2.3 depicts the number of storms with low, medium and high intensities emitted from each source points. By comparing Figure. 2.3a and Figure. 2.3b, it can be concluded that spatial distribution of low-intensity dust storms and absolute frequency patterns of all storms from each source are seemingly similar. Regions with high absolute frequency have high frequency of low-intensity dust storms. There is likely a strong and direct relationship between absolute frequency of occurrence of dust storms and frequency of low-intensity dust storms.

Unlike low-intensity dust storms, the spatial distribution of medium-intensity dust storms does not exhibit a special pattern. As depicted in Figure. 2.3c, the majority of identified source points, frequency of medium-intensity dust storms fluctuates between 3 to 6 events. There are only a few locations, including the southern parts of Iraq, where the frequency of medium-intensity storms are higher in comparison to other similar types of storms elsewhere in the region.

Note that high-intensity dust storms are mainly located west of Iraq and near the border of Iraq and Syria, implying that this region is one of the critical areas in terms of dust storm intensity due to the high frequency of low-, medium-, and high-intensity dust emissions. Lower numbers of high-density dust storms in the southern and eastern parts of Iraq were observed, where the frequency of low and medium intensity is higher than any other studied regions. The importance of intensity categorization can be appreciated since this latter area was previously classified as "large" in terms of area and "high" in terms of absolute frequency of occurrence. As shown in Figure. 2.3d, the majority of dust storms from this region, in this study, is considered as low and medium intensity and, consequently, may not play a key role in dust storm generation in the Middle East.

Regarding the dust storm classification in terms of intensity, it should be mentioned that in almost all studied countries with dust storms, low-intensity dust storms have the highest frequency and medium and high intensity are second and third, respectively. Among these countries, Iraq is an exception, since the frequency of high-intensity dust storms is much higher than the other categories (about 34 % of all storms). This observation hints to Iraq's critical situation in regard to dust storms production. Jordan and Iran do not have a considerable number of high-intensity dust source points. Although the absolute frequency of dust storms in Syria is higher than Saudi Arabia, the frequency of low-intensity dust storms is much higher than other categories of dust events. Frequency of high intensity dust storms in Saudi Arabia and Syria are 10 and 11 per 12 years, respectively, which indicates that Saudi Arabia significantly participates in high-intensity dust storms. Due to atmospheric circulation regardless of the source of dust storms, these emissions will have local, regional, and possibly global effects.

2.4.3 Comparison with Previous Literature

Over a 13-year period (1980-1992), Prospero et al.[107] performed one of the most comprehensive and detailed dust source identification studies using TOMS AI. In comparison to the algorithm used in our work, the TOMS AI method has two principal restrictions in dust source identification. Firstly, as mentioned above, the spatial resolution of the TOMS sensor is about 50 × 50 km^2 (1000 × 1000 m^2 in MEDI algorithm). The TOMS data only identifies sources greater than the 2500 km^2. Thus, this method may be unable to identify source points smaller

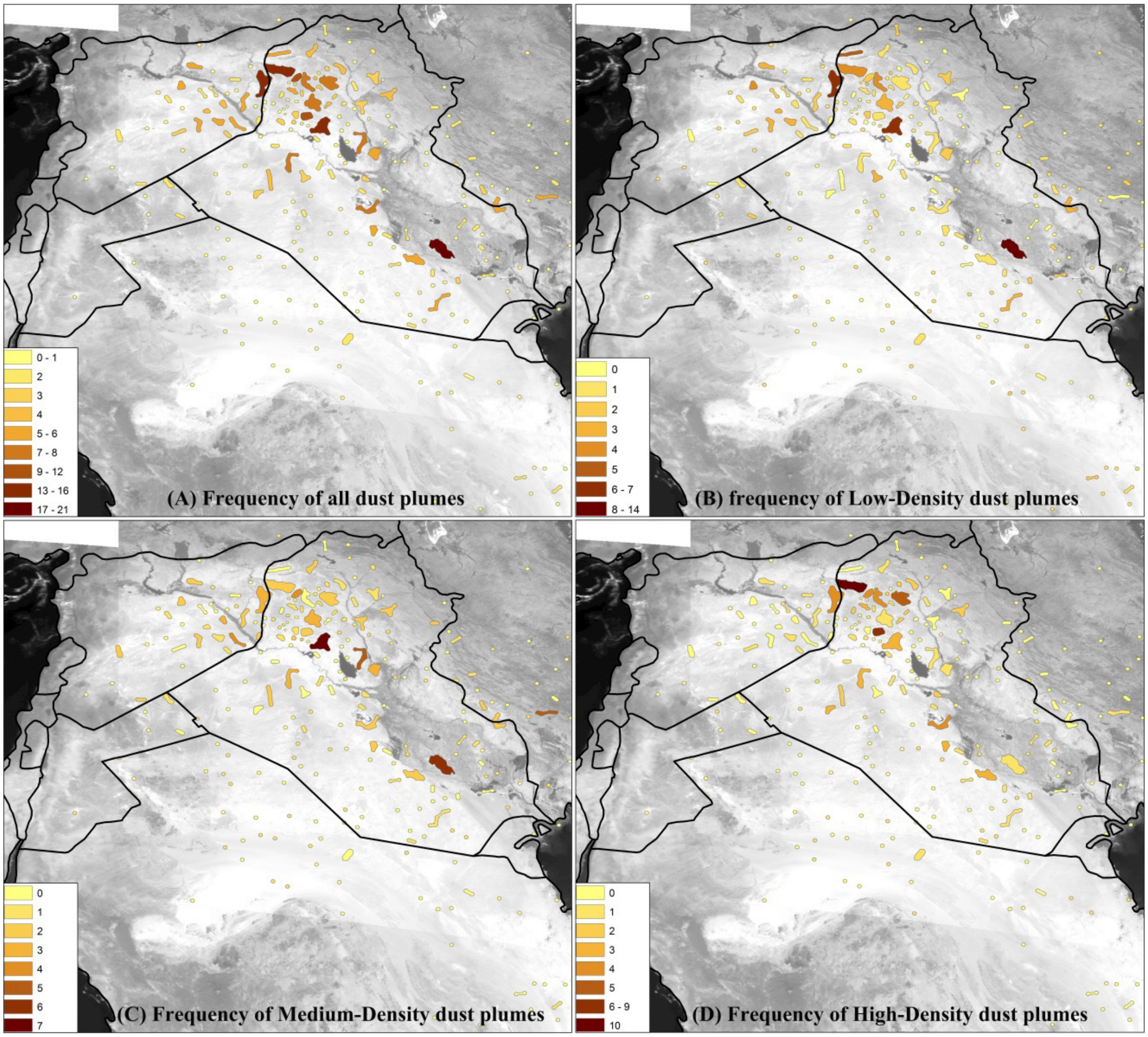

Figure 2.3: (a) Spatial patterns of dust plume frequency over each identified source points over 12 years (2001-2012), (b) frequency of low-intensity dust plumes over each identified source point, (c) frequency of medium-intensity dust plumes over each identified source point, (d) frequency of high-intensity dust plumes over each identified source point.

than 2500 km^2. Based on our analysis, a significant number of source points are smaller than this spatial resolution. Moreover, TOMS AI depends almost linearly on the altitude of the plume.[126] As the sensitivity near the surface is reduced, the source location is biased toward the downwind area, as shown by Mahowald et al.[127] Another issue, which restricts the TOMS AI method in identifying actual source points, is the high value of AI through the pathway of dust storms. Although as a general rule that the value of AI in source points is greater than the other regions,[126] the value of AI is usually high in the pathway of the dust plumes, similar to source points. On the occurrence of dust storms, the value of AI is significantly high in both source areas and the way that dust emanates toward the other regions. Therefore, it has been observed that in several regions where dust has already crossed, these areas have been misidentified as source regions.[126,128]

Another comprehensive study has been recently accomplished by Ginoux et al.[128] in which the global scale attribution of anthropogenic and natural dust sources and their emission rates were derived based on the MODIS Deep Blue level 2 (M-DB2) aerosol products. They have used collection 5.1 level 2 products from MODIS on the Aqua platform from 2003 to 2009, and the aerosol products were interpolated on a regular 0.1° latitude-longitude grid using the algorithm described by Ginoux et al.[105] They have also derived dust optical depth (DOD) from AOD using a screening method which applies three conditions that are based on size distribution, absorption of solar radiation in the green (550 nm), and the contrast of absorption between the red (670 nm) and Deep Blue (412 nm) channels.[128]

Unlike the TOMS AI index, the MODIS DB algorithm is using wavelengths in the visible (although near the ultraviolet part of the visible spectrum), and the retrieval is thus much less sensitive to the altitude of the aerosol layer.[120] Similar to the TOMS AI algorithm, a drawback of the MODIS DB algorithm methodology[128] is that the spatial resolution of Deep Blue data is about 1°, which are too coarse to accurately detect small-scale sources. In our analysis, the MODIS data with a spatial resolution of about 1000 m was used to ensure detection of most source point regions with small areas. These regions are usually not identified as dust source regions due to the above mentioned discussions. Figure. 2.4 illustrates the results of both Ginoux et al.,[128] and our analysis in a small region near the border of Iraq and Syria. As shown in this figure, although the results of both studies show small differences, they both identify this source region accurately. As illustrated in Figure. 2.5, Ginoux et al.[128] have identified the entire Nainava region as source points, while the present study provided agreement on the identification of this source region, it also provided added details and complexity to these identified sources. Dust source areas extracted from the Ginoux et al.[128] study covered a significantly larger area than this work.

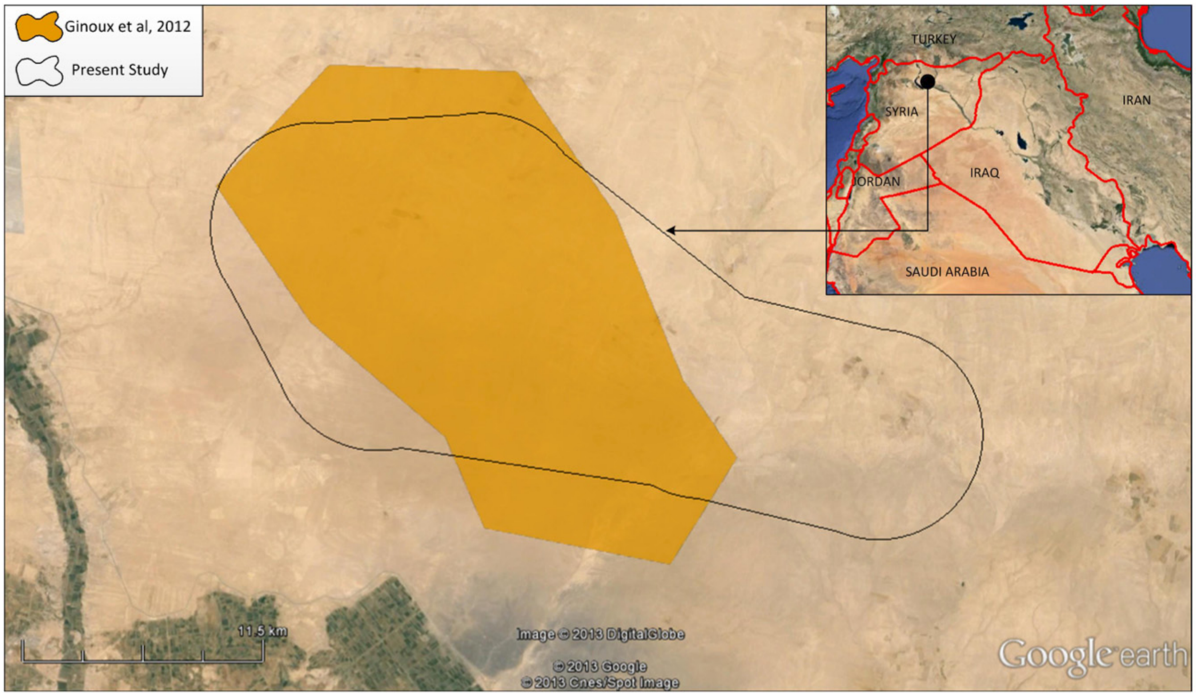

Figure 2.4: Comparison of source identification techniques in a small region in Syria.

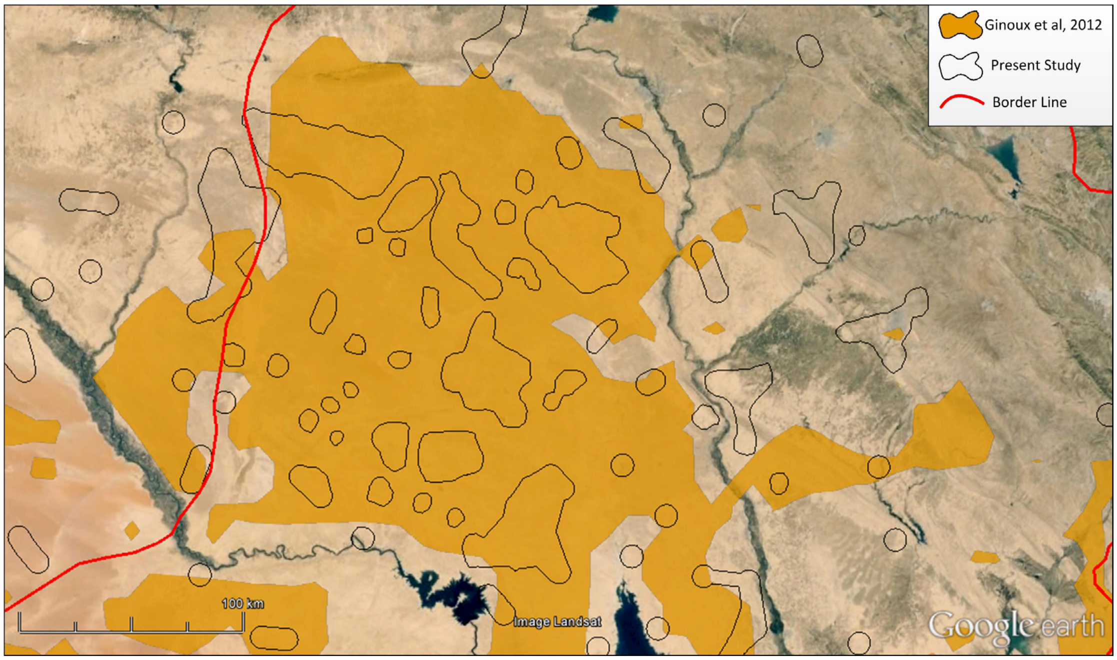

Figure 2.5: Comparison of dust source identification techniques over a major area of sources on the border of Iraq and Syria.

2.5 Conclusion

We found that 247 different source points located in Iraq, Syria, Saudi Arabia, Jordan, and Iran have participated in dust storm generation in the region. Results of this study also demonstrate that Iraq is currently the most efficient site for dust storm generation in the region. In particular, Neinava was identified as the most active hot spot in the Middle East. Although the present study shows much promise and clear advances in identification of the majority of dust sources, there is room for improvement in future studies. Namely, data used in this study are based on visual confirmation of dust storms, among all datasets, which should be more substantiated with other techniques including ground and remote sensing measurements in the future. Another source of future work can be related to the sampling time by MODIS. Polar orbiting satellite instruments, like TOMS or MODIS, have a local passing time, which may not necessarily coincide with the peak of dust emissions. Further observational meteorological sites in the Middle East are required, as current ground-based observation sites are scarce at best. Furthermore, the impact of anthropogenic activities in the generation of new dust source points and their impacts in the region should be studied.

Chapter 3

Newly Desertified Regions in Iraq and its Surrounding Areas: Significant Novel Sources of Global Dust Particles

Abstract

Using the newly developed Middle East Dust Index (MEDI) applied to MODIS satellite data, we consider a relationship between recently desertified regions, over the past three decades, and the dust source points identified during the period of 2001-2012. Results indicate that major source points are located in Iraq and Syria, and by implementing the spectral mixture analysis on the Landsat TM images (1984 and 2012), a novel desertification map was extracted. Results of this study indicate for the first time that c.a., 39% of all detected source points are located in this newly anthropogenically desertified area. Using extracted indices for Deep Blue algorithm, dust sources were classified into three levels of intensity: low, medium, and high. A large number of low frequency sources are located within or close to the newly desertified areas. These severely desertified regions are an immediate concern at a global scale.

3.1 Introduction

In recent decades, there has been increasing interest in understanding atmospheric physics and chemistry of aerosols, and aerosol-cloud interaction processes. Atmospheric aerosols are defined as condensed matter (liquid, solid or heterogeneous) suspended in the air. These aerosols consist of natural and anthropogenic species in particle form with aerodynamic diameters ranging from a few nm to several micrometers. The two ubiquitous and important natural kinds of aerosols are sea salt and mineral dust, which are emitted into the atmosphere as a result of wind stress at the ocean surface and arid land areas, respectively.[129]

Aerosols and their interactions with clouds and radiation "contribute the largest uncertainty to the total radiative forcing estimate" for climate change. Dust aerosols can significantly impact the Earth's climate system[130,131] by changing the radiation budget,[132–135] cloud optical properties and lifetimes,[136,137] and precipitation processes.[138,139] They can also influence the Earth's ecosystems through marine and terrestrial biogeochemical cycles,[140–142] hydrologic processes[143,144] and human health.[145] Desertification, the damage to land that creates deserts, is a serious environmental threat for inhabitants of deserts and a main element of global change, causing wide scale land degradation in arid and semi arid regions of the world.[146] Different forms of desertification take place in terms of patterns and processes. In this study, this term has been used to refer to the removal of vegetation and soil salinization and is driven by a number of social, political, economic, and natural factors (such as population growth, drought, climate variations or changes, tillage for cultivation and overgrazing). Indeed, vegetation cover and soil salinity (alone or combined) plays a major role in determining the biological composition of the soil and has been the main driver the development and increase in desertification. The concept of desertification and dust plumes is well established. The term of desertification became well known in the 1930s when parts of the Great Plains in the United States turned into the Dust Bowl.

By studying the interactions between desertification and dust storms, scientists will be better able to understand the role human and natural induced factors play in the magnitude of dust storms.[128,147] Okin et al.[148] in a study over the Mojave Desert found that abandoned agricultural fields can produce materials that are transportable into stable desert surfaces and can change dersert spectral reflectance.[149] Additionally, wind-blown sand can lead to the expansion of desertification by burying, abrading, or stripping leaves from plants that are in the flow direction and potentially lengthen the pathway of dust.[146]

Human contribution to the mineral dust abundance has been estimated to be as high as 30-50%.[132,150] Some researchers have provided a sensitive link between desert dust emissions and climate; yet, how humans affect desert dust emissions is not well characterized,[151] partly due to the fact that the anthropogenic forcing is very sensitive to models and meteorological conditions.[152–154]

The Middle East region has been considered to be responsible for approximately 25% of the Earth's global emissions of dust particles.[155,156] This region, which has been experiencing severe environmental challenges is also vulnerable to climate and human induced changes. Dust storms are one of the traditional outcomes of extreme weather events in arid and semi-arid countries located in this region and these have been more frequent and intense in the past decade.[113] Recent studies in the area have shown that Iraq and Syria are the major countries generating dust storms, noting that there is currently no consensus on the factors driving enhanced dust storms. Some contributing factors include inappropriate agricultural practices,[157] unsustainable water resources management and climate change,[158] military operations[159] and land degradations.[160] Gibson[159] in a thorough study assessed whether cultivated areas in Iraq changed during or as a result of war and sanctions. The results indicate that cultivated areas changed little between the Iran-Iraq War (1980-1988) and the Gulf War (1990-1991), increased by 20 percent (from 1.72 to 2.04 Mha) during the period of the United Nations sanctions (1990-2003), and dropped to below pre-sanction levels (1.40 Mha) during Operation Iraqi Freedom (2003-2011). Also, more information on the impact of haphazard driving and military operations (thousands of trucks and heavy vehicles, explosion of numerous bombs and rockets) on compacted top soil layers, causing emissions of dust, can be found in the work of Sissakian et al.[160] These factors have been suggested as having major impacts on desertification in the region, and the increased challenges linked to regional dust storms.

The aim of our study was to provide insights on the location, frequency and intensity of the new and mostly man-made dust storms. Also, the main objective of the present study is to determine the role of desertification in the process of the growing frequency and intensity of dust storms in the Middle East region. We herein concurrently deploy: (a) satellite data (NASA/MODIS and NASA Landsat TM), (b) dust source point identification techniques (using the newly developed Middle East Dust index to map the region); (c) spectral mixture analysis (for further desertification information extraction), and (d) change vector analysis (to study intensity of desertification change in the Middle East).

3.2 Background of Study Region

The Middle East, which consists largely of the Arabian Plateau and the Tigris-Euphrates Basin, is one of the world's active wind erosion regions.[114] The Arabian Plateau is generally considered to be from the southwest high terrains (1500-3000 m) bordering the Red Sea towards the northeast flat lands (50-200 m) next to the Persian Gulf[161] identified as Arabia, one of five world regions where dust storm generation is intense (Figure. 3.1). The area of desert, which stretches across Iraq, Iran, Afghanistan, Pakistan, and northwest India, has long been recognized as a source of atmospheric mineral dust.[115,116] The major southern interior of the Arabian Peninsula is made up of the Rub Al-Khali (or Empty Quarter, 582750 km^2), which is one of the largest sand deserts in the world and is connected to the An Nafud sand sea in the north by the Ad Dahna (a sand corridor 1287 km long).[114]

Previously, researchers have recognized two major dust regions in the Middle East: (I) In 1986, Middleton[162] carried out a preliminary analysis of the distribution and seasonality of dust storms using meteorological data and demonstrated that the Lower Mesopotamian plains (Iraq and Kuwait) exhibited the highest number of dust storm days per year (especially from April to August). Central Saudi Arabia showed a moderate level of dust storm. Note that previous studies have indicated the alluvial plains,[163] off the Omani coast[164] and Arabian Sea[165] have a considerable number of dust storms in the Middle East.

There are four dominant climate systems in the Middle East: (1) in winter, the Siberian anticyclone over central Asia; (2) the Polar anticyclone over eastern Europe and the Mediterranean Sea, in the summer; (3) the monsoon cyclones over the Indian Subcontinent, the south and southeast of Iran and southeast of the Arabian peninsula, in the summer; (4) the depres-

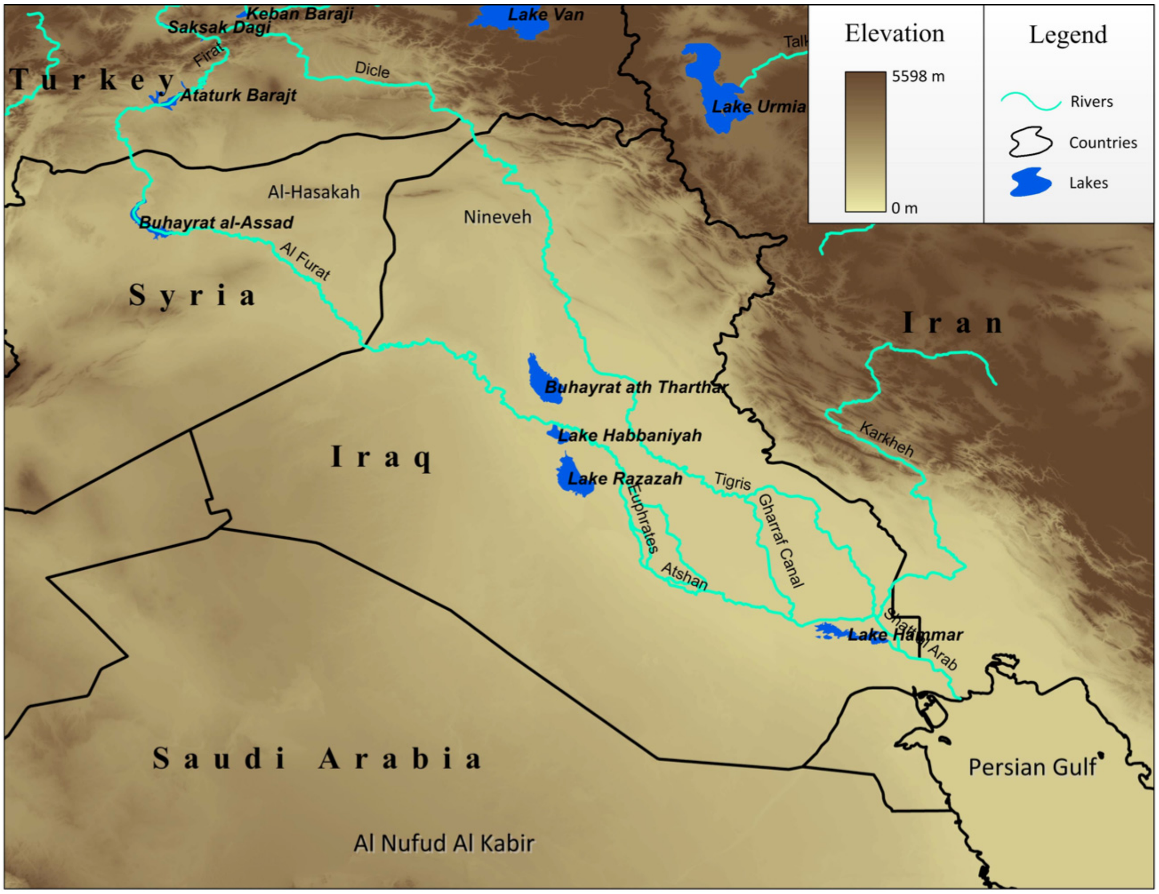

Figure 3.1: Iraq and its surrounding countries (Background image shows the topography of study area).

sions traveling from northern Africa and the southern and eastern Mediterranean sea across the Middle East and southwest of Asia in the non-summer seasons (spring and winter).[117] Two winds in particular generate dust in the region: The Shamal wind, which blows from mid-June to mid-September, creates severe summer Shamal dust storms, and prefrontal and postfrontal winds which generate frontal dust storms in other seasons.[118]

3.3 Data and Methodology

3.3.1 NASA/MODIS

Moderate Resolution Imaging Spectroradiometer (MODIS) data were used to compare several dust retrieval algorithms and to apply a new approach to identify dust source points by a combination of the visible (VIS) and thermal infrared (TIR) bands. This sensor makes observations using 36 bands with wavelengths ranging from 0.41 to 14.4 μm and nadir spatial resolution of 0.25, 0.5, and 1 km. MODIS, launched in December 1999 and May 2002, respectively, is operating onboard the NASA Earth Observing System (EOS) Terra and Aqua satellites. MODIS data were obtained from the Level 1 Atmosphere Archived and Distribution System and processed to convert the digital numbers into radiometrically calibrated and geo-located data products. The daily MODIS Level 2 Aerosol data were also used. These data are produced at spatial resolutions of about 1×1 km^2 pixel arrays.

3.3.2 NASA/Landsat TM

The Landsat Thematic Mapper (TM) sensor was carried onboard Landsats 4 and 5 from July 1982 to May 2012 with a 16-day repeat cycle. Images consist of seven spectral bands with a spatial resolution of 30 m for Bands 1 to 5 and 7. Spatial resolution for Band 6 (thermal infrared) is 120 m. This data was used in change detection analysis and desertification extraction. Since we are looking for the trend and potential impact of desertification on the dust source point developments, the study tried to define a possible longer period of time for better analysis. On the other hand, the availability of data and the highest number of cloud-free images giving almost a full coverage for the region within a year were other factors in choosing the time domain. We used data from the Landsat TM sensor that has been operational since 1984. Therefore, 1984 and 2011 were selected as the boundaries of the study. According to our hydrologic analysis, both years are normal rainfall years as well.

Therefore, 32 cloud and dust free satellite images, of equal scale, were used and analyzed. More importantly, based on the goal of this study and other similar studies for land and water cover change detection, the images obtained correspond to the end of the growing season. Consequently, all images were acquired for September, which is considered the end of the growing season in the Middle East region.

3.3.3 Source Point Identification

We used satellite observations to illustrate a new mapping technique for dust source points in the Middle East region to retrieve spatial pattern, area, and intensity of each source point and to interpret different countries' contributions to the generation of dust storms in the study area. Unlike ocean and water surfaces, it is very difficult to detect mineral aerosol (or dust events) over the surface of desert and land bodies due to the similar reflectivity of mineral aerosol and desert lands using unadjusted VIS satellite imagery. In addition, several challenges (such as sensor capability and model accuracy) exist in differentiating mineral aerosol from cloud, sea salt, and anthropogenic pollution. As a result, a number of studies have used brightness temperature changes between mineral aerosols and land surfaces to distinguish them from each other.[121,122] The use of single TIR has had limited success due to the changes in surface emissivity.[123,124] Because of this limitation as well as the emissive variability and the transmissive properties of mineral particles within multi- TIR ranges, several algorithms have been invented based on the brightness temperature difference (BTD), as bi-spectral split window techniques. BTD is based on temperature differences between the ground surface and cooler mineral aerosols which at the same time is largely unaffected by absorption from other atmospheric gases.[125]

The dust source identification method in this study is based on a new model, called Middle East Dust Index (MEDI) retrieved in the previous work by Karimi et al.[113] In MEDI, four major dust source identification models: (Ackerman's model, Roskovenesky and Liou algorithm, Normalized Difference Dust Index (NDDI), Deep Blue algorithm) were analyzed and compared within the study region, and the advantages and shortcomings were evaluated. To analyze the performance of different MODIS dust retrieval methods in identifying source points, three dust events, which originated in the Middle East region, were studied. Because of the specific situation of the Middle East area (more brilliant desert, mineralogical diversity of source points, and dust storm occurrence in different meteorological conditions), these techniques could not effectively differentiate dust plume from the bright desert surfaces (due to the same thermal behavior of dust and desert surfaces in brighness temperature (BT) of both BT_{31} and BT_{32}). Numbers denote the number of band in MODIS image. Consequently, we previously strived to develop a new approach by gathering all points to improve dust plume identification using MODIS data called MEDI. In this model, BT_{29} was involved to highlight the difference between dust and desert surfaces. Several factors, which can significantly affect dust plume and source identification, have also been included in MEDI, namely single or multiple dust plumes and multi-mineralogical dust plumes. In addition to the satellite-based algorithms, the HYbrid Single-Particle Lagrangian Integrated Trajectory (HYSPLIT) model was used to recognize dust sources in each event separately. For dust source identification, we first developed a new model, MEDI, specifically designed for the Middle East region, and then applied it to all MODIS images associated with 70 dust storms occurring in the period 2001 to 2012.

$$\mathrm{MEDI} = \frac{\mathrm{BT}_{31} - \mathrm{BT}_{29}}{\mathrm{BT}_{32} + \mathrm{BT}_{29}} \times \mathrm{A} \tag{3.1}$$

$$A = \begin{cases} -999, & \text{if NDDI} < 0 \\ 1, & \text{otherwise} \end{cases} \tag{3.2}$$

$$\mathrm{NDDI} = \frac{\rho_{2.13} - \rho_{0.469}}{\rho_{2.13} + \rho_{0.469}} \tag{3.3}$$

$$\mathrm{Dust} = \mathrm{MEDI} < 0.6 \tag{3.4}$$

Where BT is the brightness temperature in MODIS bands and ρ is the reflectance of dust. Normalized Difference Dust Index (NDDI) is another dust characterization factor, which enables the MEDI model to better distinguish dust plumes in the satellite images. After validation of MEDI and ensuring that it is capable of dust source identification, this model was applied, in this study, to 70 separate storms during the period of 2001 and 2012.

Although our new model shows its capability to determine dusty pixels more accurately, some mismatches of our models should be noted here. First, in the case of cirrus clouds, some misidentifications were found and the NDDI index was used to modify them. Also, in snow-covered areas, some misclassifications were detected in some cases. This can introduce some errors in winter storms and in the high mountain areas of Iran as most of the time these regions are snow covered. Thus, it is suggested that before using the MEDI model, the Normalized Difference Snow Index (NDSI) should be used to eliminate the snow-covered areas.

Although in MEDI the 0.6 threshold value (dust B 0.6) can identify dusty pixels sufficiently, it should be adjusted for each event separately using its relevant histogram, because like other discriminating algorithms, this value can vary based on the thermal properties of ground surface and the amount of moisture content.

3.3.4 Desertification Extraction

Vegetation indexes (such as Normalized Difference Vegetation Indexes (NDVI)) and image classification approaches (including maximum-likelihood, clustering and discrimination analysis) have been most commonly used to map spatial and temporal variation in vegetation covers and ultimately desertification monitoring.[166,167] But the biggest obstacle and difficulty of these methods is the existence of mixed pixels in the satellite imagery used. This issue is more common in using low and medium spatial resolution satellite images (e.g., Landsat-TM and MODIS images). Therefore, if the aforementioned techniques (vegetation indexes and classification approaches) are used for desertification monitoring, to obtain an accurate measurement, the pixel size of the image used must be smaller than the scale of variability of at least one of the principle landscape elements (e.g., trees or grasslands). One of the best and most efficient solutions to resolve this problem is to use sub-pixel classification techniques that could be used to unmix the soil-plant canopy measurements into the respective soil, vegetation, and non-photosynthetic vegetation. In other words, one approach for measuring desertification in terms of the relative proportion of vegetation covers in image pixels is the Spectral Mixture Analysis (SMA) method that can quantify the proportion of each pixel occupied by individual image components.

In order to study desertification, several factors prompted the use of the SMA in the present study: (1) Sparser vegetation cover due to the arid and semi-arid characteristics of the study area; (2) Inefficiency of the common classification methods; (3) Higher accuracy of the spectral mixture analysis method compared to vegetation indices approaches; (4) The ability of the spectral mixture analysis method to identify the intensity and direction of changes over land at the same time.

Implementation of SMA techniques consists of three steps: (A) identification and assessment of the dominant phenomena in a landscape for endmember selection, (B) identification of endmembers within a pixel and extraction of their spectral libraries, (C) determination the contribution of each of the dominant phenomena (endmembers) in each pixel of the satellite image used. SMA can be implemented in different ways, whereby the Linear SMA (LSMA) is the most common and most popular. The basic LSMA equation is as follows:[167,168]

$$R_p(\lambda) = \sum_{i=1}^{n} f_i R_i(\lambda) + \epsilon(\lambda) \tag{3.5}$$

Where $R_p(\lambda)$ is the surface reflectance of each individual pixel, f_i is the weighting coefficient (the sum of all values will be equal to one) and interpreted as a fraction of each pixel made up of endmember (e.g., soil, vegetation of salt), $R_i(\lambda)$ is the amount of reflectance for each endmember in a n-endmember model and $\epsilon(\lambda)$ is the difference between the actual and modeled reflectance.

Endmembers selection is the most critical step in SMA.[169] Although there are many approaches for selecting endmembers (e.g., image endmember and library endmember), image endmember selection based on the Principle Component Analysis (PCA) approach is more common and has been used frequently for change detection analysis.[170–172] Two advantages of this technique are that the selection of the endmember spectra is based on the inherent spectral variability of the image data without requiring homogeneous pixels of each endmember and its simple implementation.[167,173] A more detailed description of image endmember selection is given by Dawelbait and Morari.[167]

After implementing the spectral mixture analysis, the trend of changes for four main extracted features including soil, vegetation, salt, and water cover were analyzed over Iraq and Syria which, between 1984 and 2011, were two major source points of severe and frequent dust storms in the Middle East region. Since the study area is very large (c.a., 547,000 km^2), it was divided into two separate upper and lower parts and 16 Landsat-TM images were merged in order to obtain the complete coverage of the area.

3.3.5 Change Vector Analysis (CVA)

Although trend of changes for different covers was quantified separately, it is not possible to have a comprehensive analysis of all parameters together (e.g changes in area of vegetation, water body, marshlands, ...). In fact, these types of comparisons can specifically explain changes in different covers; however they do not evaluate the possibility of identifying the desertified regions and making final decisions for dust storm source points. Consequently, besides these comparisons, changes were analyzed using the CVA method. Euclidean distance was used to measure the intensity of changes. To identify the direction of changes, change vector was employed as a function of angle in each satellite image in time 1 (1984) and time 2 (2012). Three dimensional vector analyses were used, in which the trend of changes for three parameters, which included soil, vegetation, and salt covers were analyzed at the same time. By implementing this model, two major types of changes were observed. The first is the new irrigated farmlands as a result of agricultural development along the rivers and irrigation networks in the region and the second type of change is the area in which the vegetation, soil, and salt covers have been degraded toward being a desert. As previously mentioned, this mainly includes the abandoned farmlands no longer used for agriculture and farming. Figure 3.2 contains a flowchart outlining how the desertification map is extracted.

3.4 Results and Discussion

By studying all the dust sources points in the Middle East in the period from 2001 to 2012, it was found that major dust spots are located in Iraq and Syria when compared to the other countries of the region. Our results indicate that approximately 12,218 km^2 of both Iraq and Syria has become desertified during the past three decades (Figure. 3.3). Note these areas have recently joined traditional sources of dust storms in the region and produce significant dust storms. The major desertified areas identified through change detection analysis are located between the Euphrates and Tigris Rivers which include northeastern Syria and northwestern and western parts of Iraq (elevation 270-640 m), some parts of central and eastern Iraq close to the border of Iran (elevation 3-360 m), and finally the northern border of Saudi Arabia with Iraq and Jordan (elevation 790-930 m). Lakes were separately classified into two groups: dried and generated. In addition to desertification, an increase in the vegetation cover (regrowth) was also detected and was categorized into low and high regrowth.

As depicted in Figure. 3.3, the highest area of concentration for severe desertification is located in the northwestern border of Iraq and Syria from Nineveh in Iraq to Al-Hasakah in Syria. This region predominantly comprises farmlands, and is close to the border of Turkey. The topography and river morphology of this region indicates that constructed dams and water control in river basins have significantly reduced the stream flow, which impacts the

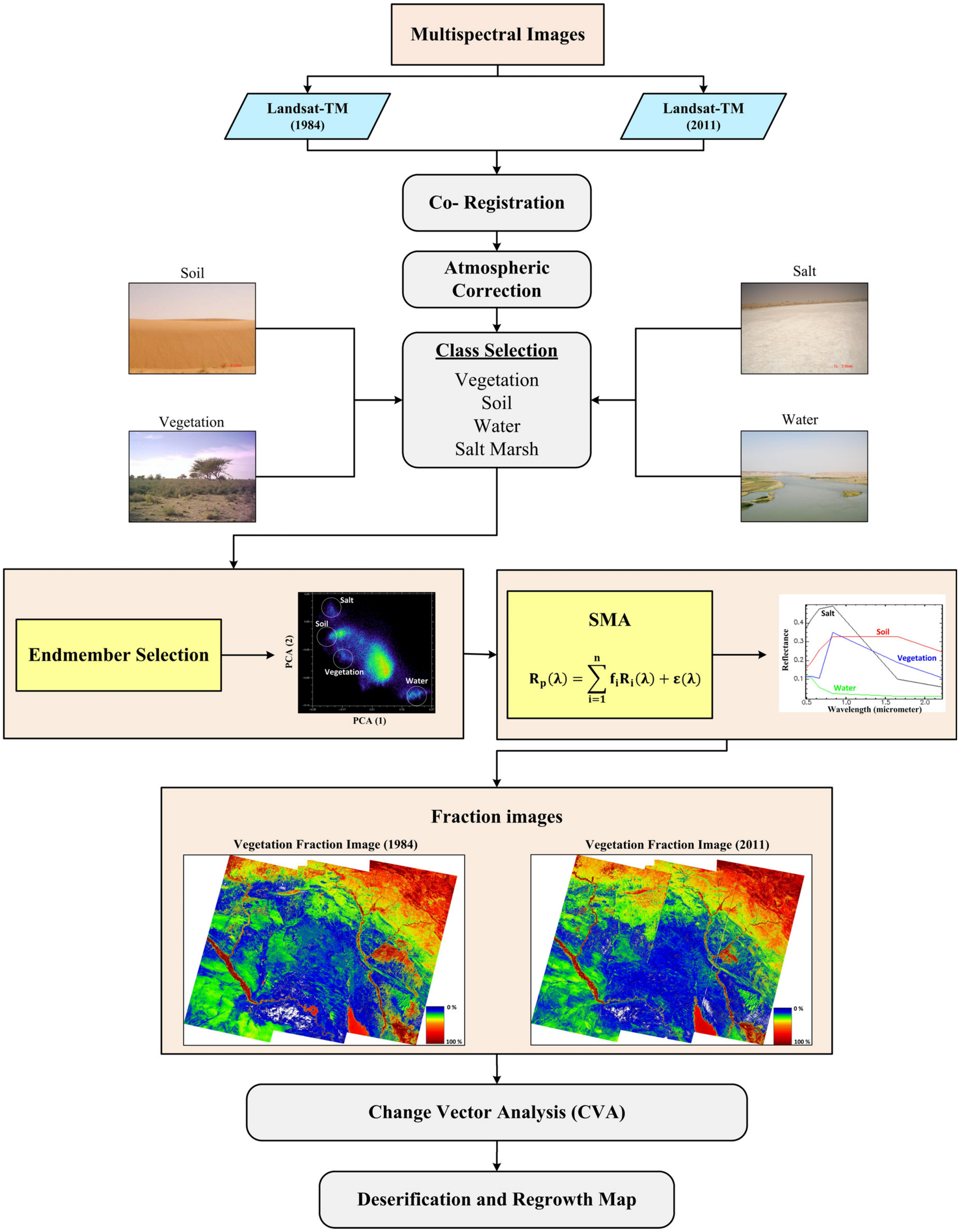

Figure 3.2: Spectral Mixture Analysis procedure for delineating desertified areas.

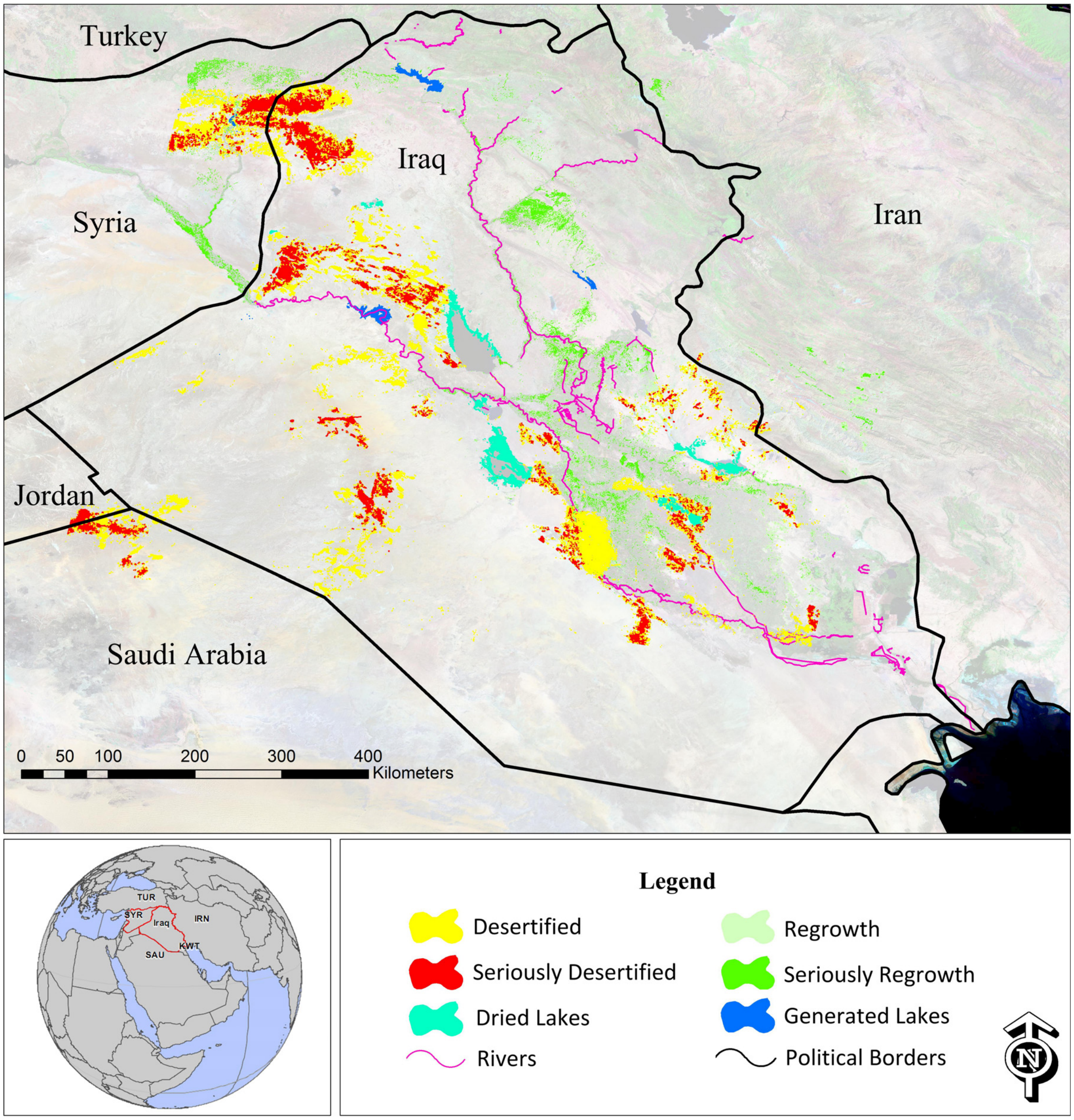

Figure 3.3: The newly desertified regions over Middle East region involved in dust storm.

downstream zones. Another large portion of both high and low intensity desertified areas originates in the northern part of the Euphrates River between Tharthar Lake in Iraq and the Iraq-Syria border and continues through scattered areas in central and eastern parts of Iraq.

A large number of low desertified zones were found in the lowlands (elevation between 20 and 25 m), along the Euphrates River before and after the city of Najafol Ashraf. Interestingly enough, the highest concentration of high and low regrowth lands is also located in this zone. The main reason for this consequence is that most parts of this area, which was already deser-

Table 3.1: Area of different desertified categories in Iraq and Syria (in km^2)

Desertified-high	Desertified-low	Dried water	Regrowth water	Regrowth low	Regrowth High
6968	3752	1498	550	1191	2512

The cumulative error is less than or equal to ±5 percent.

tified, have recently been recovered by releasing the stream flow in the upstream (Richardson et al., 2005).

Our results (Figure. 3.3) show that Rezazza Lake in northeastern Karbala in the heart of Iraq has severely shrunk to less than half the size, compared to three decades ago. The Euphrates River is the source of water for this lake as well as for Habbaniyah Lake to the north of Rezazza Lake. The surface area of Tharthar Lake, located in northwestern Baghdad, which is fed by the Tigris River, has also decreased in both sides and in the north. In the last decade, several small bodies of water, close to Nineveh and in the eastern parts of Iraq, have been completely desiccated (Figure. 3.3).

Water surface has increased by about 550 km^2 (Table 3.1) in the sites of the newly constructed dams' reservoirs that impound large lakes including Mosul Dam Lake, Dukan Lake, Haditha Dam Lake and Al-Azim Dam Lake in Iraq and Ad Dughayrat Dam Lake in Syria. Growth change analysis (Table 3.1), indicates that the highest regrowth areas are mostly located along the rivers and downstream of the newly-constructed regional dam. The main factor for the increase in green lands surface is attributed to the agricultural development and the establishment of irrigation systems and harvesting water from the rivers. Such changes are observed in northeastern and eastern Syria along the Euphrates River especially from Deir ez-Zur to Al Bukamal and north of Al Hasakah. Kirkuk, in Iraq, can be considered a regrowth focal point along with other regions in northwestern Iraq up to Diyala in the East and Najafol Ashraf, Al Qadesiyyah, Dhi Qar, Wasit and Maysan in central and eastern Iraq. These areas are mostly marshlands and wetlands that have recently been recovered.[174]

The extracted desertification map was superimposed on to the identified atmospheric dust source points in the Middle East region on the basis of recently developed Middle East Dust Index (MEDI) applied to 70 dust storms, which occurred in the period between 2001 and 2012 (Figure. 3.4). Results indicate that about 39% of the 243 different identified source areas, which participated in generating dust storms, are located in the newly desertified regions. Although there are desertified regions in the lower half of Iraq, the concentration and the total area of dust source points increases, up from the center of Iraq to the north and northwest as well as to the north and northeast Syria. These regions also contain the highest concentration of desertified areas and dried lakes, suggesting a positive relationship between desertification and dust source points.

There are other areas in eastern Syria, bordering Jordan with Iraq and Saudi Arabia, mid south and eastern parts of Iraq close to the border of Iran, that source points are not well overlaid on the desertification areas. Several factors can explain this observation. Firstly, there are a number of source points in the study area that are already located in existing deserts and our model shows that the location of these sources has not changed during the last 30 years. Secondly, there are new desertified regions that experienced changes including loss of vegetation cover, desiccation, or land degradation; however, they do not appear to be source points for generating dust storms, yet, they can potentially become future dust source points. Of major concern is the fact that a large portion of desertified regions is unevenly distributed in distinct climate zones, across several countries, which traditionally do not cooperate, thereby making it difficult for environmental scientists and policy makers, to efficiently overcome obstacles or implement further preventative actions to protect the lands and bodies of water, or control and manage the magnitude and rate of changes.

Since throughout the year, one specific, large area source point may not necessarily play a significant role in dust storm emissions, all the identified dust source points during a 12 year period were carefully analyzed on the basis of their frequency of occurrence and intensity. Results of this analysis show that the area of a source point is proportional to its frequency of occurrence. One of the important parameters considered in this study is dust source point classification based on intensity. Using extracted indices for Deep Blue algorithm, identified dust sources are classified into three levels in terms of intensity: low, medium, and high. The desertification map was superimposed on the frequency (Figure. 3.4A) and intensity (Figure. 3.4B-D) of dust source points. Of note is that a large number of low frequency sources are located within or close to the newly desertified areas (Figure. 3.4A). Sources of higher intensity

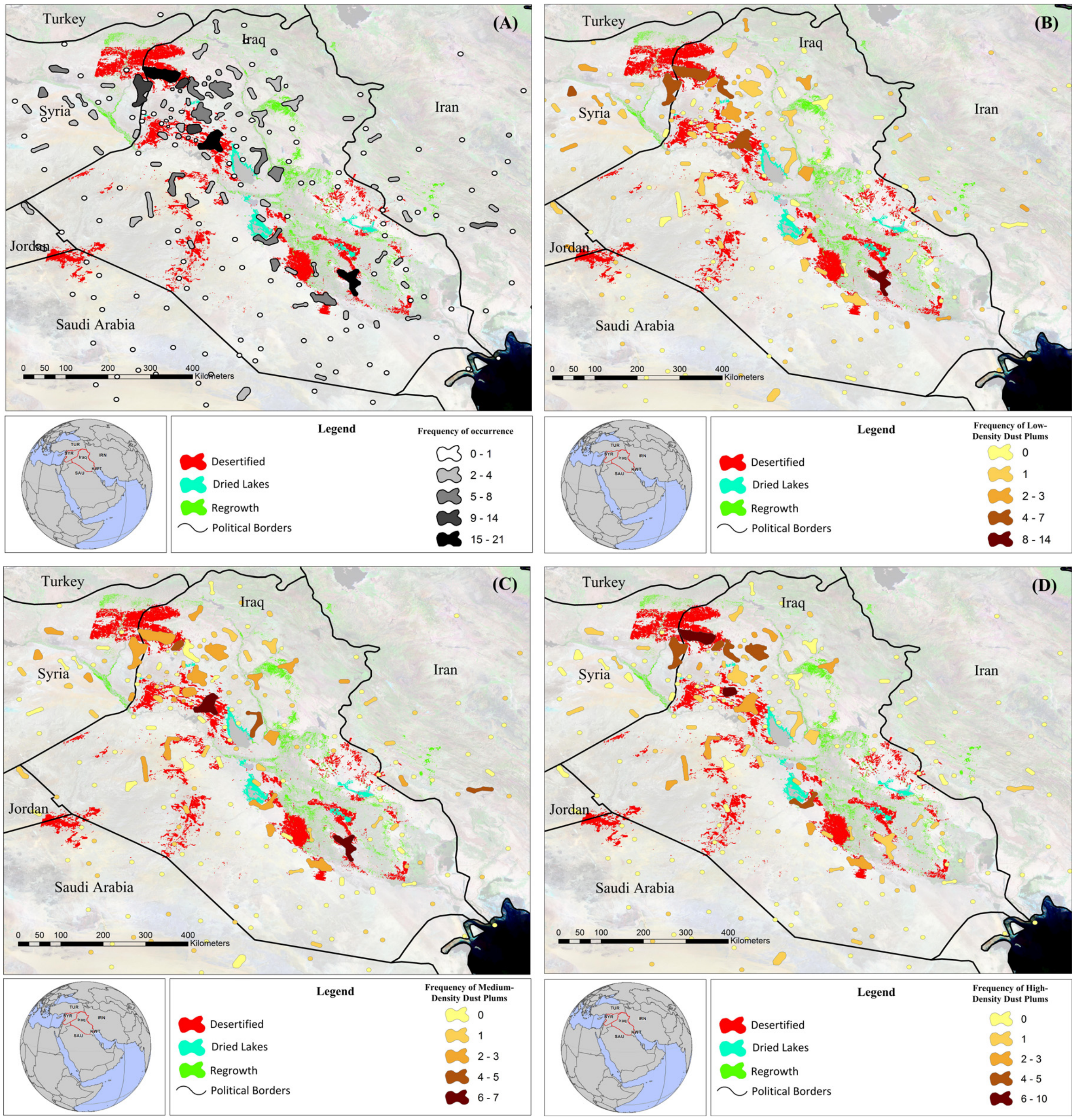

Figure 3.4: Schematic of the Middle East region involved in dust storm generation; (A) Dust storms' frequency of occurrence; (B) map of the low intensity dust source points; (C) map of the medium intensity dust source points; (D) map of the high intensity dust source points.

and frequency are also located in northwestern Iraq and in eastern Syria, where a large portion of the land has recently been desertified.

We classified recent alterations in desertification patterns in the study zone into three main categories. The first group belongs to those agricultural lands, abandoned by farmers during the last decades, which are now barren lands. These changes can be observed in northern parts of Iraq, near the Syrian border, and in eastern parts of Syria. Major causes of these land use changes in Iraq are due to drought, consecutive wars, and the lack of available water resources. The importance of dust emissions in these areas is that 40 out of the 243 source areas identified during the past 12 years are located in these abandoned agricultural fields, and thus the new desertification is predominantly anthropogenically driven. About 49% of all dust events, occur in these regions, exhibiting the highest intensity. The second type of changes is in relation to the lakes and wetlands, which have dried out and have been affected by a decrease in the amount of river flow mainly due to constructed dams on the main river or through drought. However, they have not significantly participated in generating dust storms and only few source points can be found in the dry lake margins. The third type of desertification in Iraq and Syria is in relation to the semi-desert and desert regions, which have been affected in terms of their vegetation cover and/or land condition. This category of changes is the dominant type of changes in the region and is the most important phenomenon responsible for increases in dust storms during recent years.

3.5 Conclusion

Based on AOD550 nm[1] analysis (derived from MODIS-Terra satellite image) it was revealed that the amount of AOD has increased since 2001. Mean daily AOD over Iraq and its surrounding area increased from 0.28 in 2001 to about 0.4 in 2013 (red line in Figure. 3.5). Also, the number of days with AOD greater than 0.3 increased dramatically during last 13 years (black line in Figure 3.5). The AOD greater than 0.3 was used because this threshold usually indicates days whereby dust storms happen in the Middle East. Figure 3.5 indicates that the mean daily AOD > 0.3 increased from 0.45 since 2001 to about 0.53 in 2013. Due to the dramatic recent increase in the number of dust storms, it can be concluded that significant portions of these new desertified regions are the additional causes of generating dust events, which have not been seen in the past. Figure. 3.6, shows one of the new dust plumes which were derived from desertified areas. Most current source points were also active in the past, and proper measures have yet to be taken to control their emissions. Although we did not detect significant changes over these old desert sources in the past three decades, they have

---

[1] Provided by GIOVANNI website (http://disc.sci.gsfc.nasa.gov/giovanni)

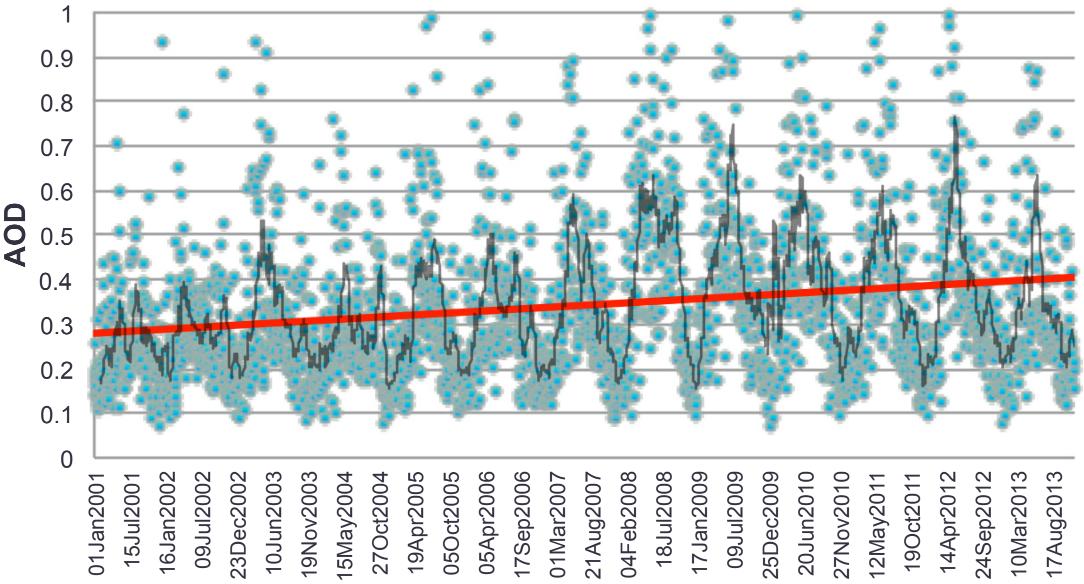

Figure 3.5: Daily mean variation and linear regression trends (red line) for the area-averaged MODIS-Aerosol Optical Depth (AOD550) in Iraq during the period 2001-2013. Black line indicates the trend of AOD >0.3.

produced a considerable amount of dust in the region and according to satellite images, have also emitted to neighboring countries. Indeed, in the Middle East, during the past 12 years, c.a. 28% of all dust events (c.a., 100) initiated at pre-existing dust emission sources. In total, approximately 39% of all analyzed dust events (144 out of 367 events) generated in areas, which have been desertified over the past three decades. In other words, these new emission sources form a significant portion of the global dust storms source points.

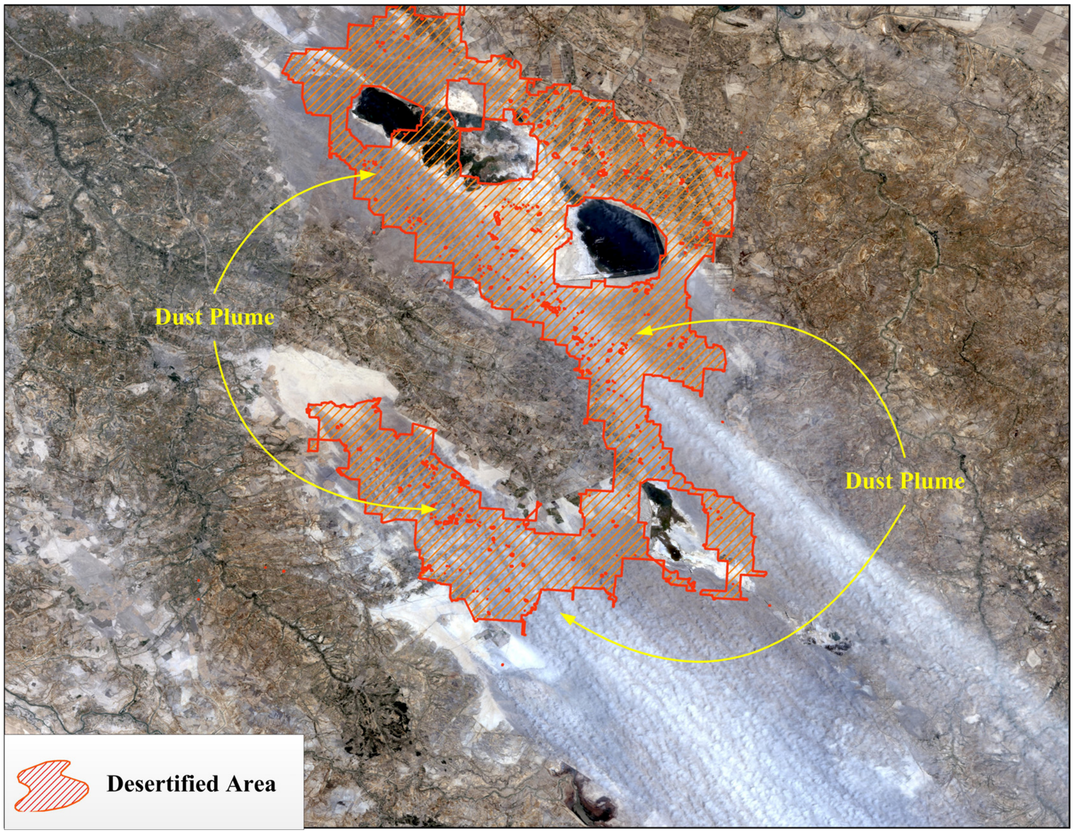

Figure 3.6: Dust plumes occurring from a desertified area. Background image is a Landsat-TM satellite image acquired in May 2012.

Chapter 4

Models of Isotopic Water Diffusion in Spherical Aerosol Particles

Abstract

Isotopic exchange experiments that utilize D_2O and H_2O have received attention as a method for studying water diffusion in high viscosity aerosol particles. However, the mathematical models used to retrieve diffusion coefficients from these measurements have yet to be critically examined. Here, two models for the isotopic exchange of D_2O and H_2O in spherical particles are analyzed and compared. The primary difference between the two models is the choice of boundary condition at the surface of the spherical particle. In one model it is assumed that the concentration of D_2O at the surface is fixed, while in the other model it is assumed that, at the particle surface, the concentration of D_2O in the condensed phase is in equilibrium with D_2O vapor. Closed-form expressions for the two boundary value problems that describe these physical models are found and discussed. Then, specific examples of aqueous droplets containing either sucrose, citric acid, and shikimic acid are examined with both models. It is found that at low relative humidities the choice of boundary condition has a negligible effect on the predicted lifetime of isotopic exchange, while at high relative humidities predicted lifetimes can differ by orders of magnitude. The implication of this result is that the choice of model can greatly affect diffusion coefficients retrieved from experimental measurements under certain conditions. Finally, discrepancies between diffusion coefficients measured using isotopic

exchange and water sorption and desorption experiments are discussed.

4.1 Introduction

Atmospheric aerosols contribute to Earth's energy budget in two major ways. First, they directly participate by scattering or absorbing solar and infrared radiation to varying degrees depending on their physical properties.[9,175,176] Second, they indirectly modify the energy budget through their interactions with clouds.[9,177,178] Reducing the uncertainties in aerosol-cloud-radiation interactions will provide significant insight on aerosols' atmospheric and climate implications.

Atmospheric aerosols can be characterized based not only on their natural and anthropogenic origins but also as being primary or secondary. Primary aerosols are directly emitted from the Earth's surface while secondary aerosols form in the atmosphere.[179] When volatile organic compounds are sufficiently oxidized and functionalized, they become much less volatile leading to compounds that can condense and form so-called secondary organic aerosols (SOAs).[180,203] Studying these particles is challenging.[181,182] An accurate estimation of the SOA fraction in the total global organic aerosol production is a top priority in today's atmospheric chemistry research, largely due to uncertainties in SOA formation mechanisms.[183–189] About 70% of organic aerosol mass consists of SOA and thus accounts for a significant fraction of ambient tropospheric aerosols.[203]

Until recently, SOA particles were assumed to be well-mixed liquid droplets with very low viscosities that would rapidly establish equilibrium with their surrounding environment. In fact, this still remains a fundamental assumption in much of the current modelling of these particles.[190] More recently, however, the discovery of viscous amorphous aerosols that form during cooling or drying have shown that kinetic limitations may be important as environmental conditions change.[60–65] A high viscosity condensed phase can lead to changes in particle dynamics and the aerosols may exhibit non-ergodic behaviour that can impact the hygroscopic growth and the activation of cloud condensation nuclei or ice nucleation.[16,72] Therefore, the assumption of instantaneous equilibrium partitioning results in significant overvaluing of the mass concentration of particles and subsequent undervaluing vapor-phase concentration of water.[191]

Recent studies have shown that SOA particles can exist in an amorphous semi-solid or glassy state based on their viscosity under very low relative humidity (RH) or temperature.[72,102,192] One definition of the glassy state is when the viscosity reaches values of greater than 10^{12} Pa·s and the glass transition temperature, T_g, refers to the temperature below which a liquid forms a glass.[67,193] Other researchers have defined viscosities of 10^8 Pa·s and higher as a threshold of the solid state for SOA derived from α-pinene ozonolysis,[61,63] which indicates that the glass transition is not sharp enough to accurately distinguish semi-solids from solids.[194]

It is now well documented that the glassy state substantially slows down the growth rate of droplets by impeding condensed phase diffusion.[64,72,73] However, in a recent study, Lienhard *et al.* argued that water diffusion in SOA particles is not as slow as it was previously presumed to be and that there is no major kinetic limitation at temperatures higher than 220 K.[81] They believe that water diffusivity in the amorphous state extends across many orders of magnitude while viscosity, bouncing factors, and T_g give indirect indications of kinetic limitations leading to poor quantification for multiphase chemistry. This might alter the direct climate effect of SOA particles.[81]

Studying aerosols on the single-particle level is appealing due to the potential for high accuracy in physical parameters retrieved from measurements.[84–89] Over the past several years, diffusion in glassy aerosols has mainly been studied by measuring water sorption and desorption from single particles.[15,80,81,83,90–92] Fitting the response of a single droplet to a changing RH during these sorption/desorption experiments has allowed for the retrieval of the mutual diffusion coefficients for a wide range of aqueous systems.[81] However, the fitting process can be time consuming as it requires using numerical solutions to a non-linear boundary value problem. For instance, Zobrist *et al.* used a finite difference method for numerical calculations of non-linear diffusion in aqueous sucrose droplets.[15] In that work, the retrieved diffusion coefficient was a complicated parameterization that was a function of temperature and water activity. The large number of parameters in the fitted function undoubtedly required an enormous amount of time to retrieve through error minimization, making this retrieval process somewhat unappealing.

An alternative experimental method for studying water diffusion in aerosol droplets that has been gaining popularity involves the use of isotopic labeling.[93–95] In this experiment, at a fixed RH, the droplet is first equilibrated with water vapor that is almost entirely H_2O. Once the equilibration is complete, the source of water vapor is replaced with one that is almost entirely D_2O. Isotopic exchange inside the droplet is then monitored over time using Raman scattering. Key to this experiment is that the RH remains constant over time. Consequently, isotopic exchange should be governed by the linear diffusion equation. Mathematically, the analysis of this experiment is more straightforward than the sorption/desorption experiment as all of the non-linearities in the boundary value problem are no longer present. This allows for analytical solutions to the diffusion equation to be found and used during the process of retrieving the diffusion coefficient.

The focus of this work is on the details of the model used in isotopic exchange experiments. In Section 4.2, using two different boundary conditions, we present two analytical solutions to the boundary value problem that describes the exchange experiment. In Section 4.3.1 we discuss how the solutions obtained using the two different boundary conditions can lead to very different results. In Section 4.3.2, this is explored further through the consideration of aqueous sucrose, citric acid and shikimic acid droplets (all systems that have been studied using both sorption/desorption experiments and isotopic exchange experiments). Finally, in Section 4.3.3 we discuss how the choice in boundary condition can lead to discrepancies in the retrieved diffusion coefficient. The context for this final section is the recent reports that there can be orders of magnitude difference between diffusion coefficients retrieved using the sorption/desorption and isotopic exchange experiments.[81,95]

4.2 Theory

During the isotopic exchange experiment, the overall concentration of water in the particle c_w is assumed to remain constant with time and is equal to the sum of the concentrations of H_2O and D_2O, both of which can change, i.e.: $c_w = c_{\mathrm{H_2O}} + c_{\mathrm{D_2O}}$. If we then assume that H_2O and D_2O have identical physical properties, the constant c_w simplifies the diffusion problem in the following ways: First, the diffusion coefficient in the liquid phase will be constant as the total concentration of water will not change over time. Second, the density of the medium will also remain constant and the radius of the particle will not change over time. This eliminates the moving boundary from the problem. Third, when working with the assumption that the liquid and vapor are in equilibrium at the surface, what would normally be a non-linear boundary condition becomes linear (discussed in Section 4.2.1). Therefore, the mathematical model that describes the diffusion of water in the exchange experiment will have both linear partial differential equations and linear boundary conditions. Finally, in all of the analysis presented here, it will be assumed that the solute in the aqueous particle is non-volatile.

For an n-dimensional space, the diffusion problem in the liquid and gas-phase can be formulated as follows

$$r^{n-1}\frac{\partial c(r,t)}{\partial t} = D\frac{\partial}{\partial r}\left(r^{n-1}\frac{\partial c(r,t)}{\partial r}\right) \quad \text{for} \quad 0 < r < a, \quad t > 0, \tag{4.1}$$

$$r^{n-1}\frac{\partial c_g(r,t)}{\partial t} = D_g\frac{\partial}{\partial r}\left(r^{n-1}\frac{\partial c_g(r,t)}{\partial r}\right) \quad \text{for} \quad a < r < \infty, \quad t > 0, \tag{4.2}$$

where D is the diffusion coefficient in the liquid at c_w, D_g is the gas-phase diffusion coefficient of water, and, for brevity, $c \equiv c_{\mathrm{D_2O}}$ and $c_g \equiv c_{g,\mathrm{D_2O}}$ which are the concentrations of $\mathrm{D_2O}$ in the liquid and gas phase, respectively. For a sphere $n = 3$, for a cylinder $n = 2$, and for a flat surface $n = 1$. The boundary of the two phases is located at a (e.g. the radius of the sphere when $n = 3$). The boundary conditions come from conservation of mass,

$$D\frac{\partial c}{\partial r} = D_g\frac{\partial c_g}{\partial r} \quad \text{at} \quad r = a, \quad t > 0, \tag{4.3}$$

symmetry,

$$\frac{\partial c}{\partial r} = 0 \quad \text{at} \quad r = 0, \quad t > 0, \tag{4.4}$$

and the fixed RH at $r = \infty$,

$$c_g = c_\infty \quad \text{as} \quad r \to \infty, \quad t > 0, \tag{4.5}$$

where c_∞ is the concentration of D_2O for the RH. In addition to Eqs. A.3 to A.13, a fourth boundary condition is needed to solve Eqs. 4.1 and 4.2. Here we will discuss two possible choices: The first being that the liquid and vapor are in equilibrium at $r = a$ and the second being that c is constant at $r = a$.

4.2.1 Liquid and Vapor in Equilibrium at $r = a$

For an ideal liquid, Raoult's law states that the mole fraction of the solvent (e.g. water) is equal to its partial pressure divided by its saturated vapor pressure. For the situation of interest here, if we assume that the solution is non-ideal and that the liquid water and its vapor are in equilibrium with each other at $r = a$ we get

$$\gamma x = p/p_0 \quad \text{at} \quad r = a, \quad t > 0, \tag{4.6}$$

where γ is the activity coefficient for the mole fraction of water at the surface, x is the mole fraction of D_2O at the surface, p is the partial pressure of D_2O at the surface, and p_0 is the vapor pressure of water. The effect of surface curvature has been neglected in Eq. 4.6. Care should be taken when distinguishing between quantities that depend only on the concentration of D_2O and those that depend on the total concentration of water. In the model of the isotopic exchange experiment, γ and p_0 remain constant due to the assumptions that the total amount of water and solute remain fixed over time and that both parameters are the same for H_2O and D_2O. Using $x = c/(c_w + c_s)$ and the ideal gas law, $p = c_g RT$, Eq. 4.6 can be expressed in terms of molar concentrations c and c_g and the boundary condition will be

$$c = kc_g \quad \text{at} \quad r = a, \quad t > 0, \tag{4.7}$$

where $k = RT(c_w + c_s)/(\gamma p_0)$, c_s in the molar concentration of the solute, T is the temperature, and R is the gas constant.

To solve the above problem using the equilibrium boundary condition (Eq. A.12) we also use the steady-state assumption in the gas-phase, $\partial c_g(r,t)/\partial t = 0$. For the case of interest here, a sphere, $n = 3$ and Eqs. 4.1 and 4.2 become

$$\frac{\partial c(r,t)}{\partial t} = \frac{D}{r^2}\frac{\partial}{\partial r}\left(r^2\frac{\partial c(r,t)}{\partial r}\right) \qquad \text{for} \qquad 0 < r < a, \quad t > 0, \tag{4.8}$$

$$\frac{\partial}{\partial r}\left(r^2\frac{\partial c_g(r,t)}{\partial r}\right) = 0 \qquad \text{for} \qquad a < r < \infty, \quad t > 0. \tag{4.9}$$

The concentration outside of the sphere can be found immediately:

$$c_g(r,t) = c_\infty + \frac{a}{r}\left(\frac{c(a,t)}{k} - c_\infty\right). \tag{4.10}$$

Of course, this equation is only useful once the time-dependent surface concentration $c(a,t)$ is known. The non-homogeneous boundary value problem given by Eq. A.1 and the boundary conditions from Eqs. A.3 and A.21 can be solved once Eq. 4.10 is inserted into Eq. A.3. For the initial condition $c(r,0) = c_0$, the solution for the system is given as

$$c(r,t) = c_\infty k + \frac{2a}{r}(c_\infty k - c_0)(\beta - 1)\sum_{n=1}^{\infty} B_n \sin\frac{\lambda_n r}{a}\, e^{-D\lambda_n^2 t/a^2}, \tag{4.11}$$

where the Fourier coefficients are

$$B_n = \frac{(\lambda_n^2 + \beta^2)\sin\lambda_n}{\lambda_n^2(\lambda_n^2 + \beta(\beta - 1))}, \tag{4.12}$$

the eigenvalues λ_n are given by the equation

$$\lambda_n \cot\lambda_n = \beta, \tag{4.13}$$

and where $\beta = 1 - \alpha$ and $\alpha = D_g/(Dk)$.

The total amount of D_2O in the particle will be

$$Q_e(t) = \frac{4\pi a^3}{3}c_\infty k - 8\pi a^3(c_\infty k - c_0)(\beta - 1)^2\sum_{n=1}^{\infty}\frac{B_n}{\lambda_n^2}\sin\lambda_n\, e^{-D\lambda_n^2 t/a^2}. \tag{4.14}$$

4.2.2 Constant Concentration at $r = a$

If it is assumed that the concentration of water at $r = a$ remains constant over time then

$$c = c_\infty k \quad \text{at} \quad r = a, \quad t > 0. \tag{4.15}$$

The boundary value problem will only involve Eqs. A.21, A.1, and 4.15 (the interior of the particle) for which the solution is well-known when $n = 3$:[4]

$$c(r,t) = c_\infty k + \frac{2a}{\pi r}(c_\infty k - c_0)\sum_{n=1}^{\infty} \frac{(-1)^n}{n} \sin\frac{n\pi r}{a}\, e^{-n^2\pi^2 Dt/a^2}. \tag{4.16}$$

Outside of the particle the concentration will simply be $c_g = c_\infty$ and the total amount of D_2O in the particle will be

$$Q_c(t) = \frac{4\pi a^3}{3} c_\infty k - \frac{8a^3}{\pi}(c_\infty k - c_0)\sum_{n=1}^{\infty} \frac{1}{n^2}\, e^{-n^2\pi^2 Dt/a^2}. \tag{4.17}$$

4.3 Results and Discussion

4.3.1 The Effect of the Boundary Condition on Isotopic Exchange

In Section 4.2, two different boundary conditions were used to obtain solutions to the isotopic exchange diffusion problem: The equilibrium boundary condition was used in Section 4.2.1 and the constant surface concentration boundary condition was used in Section 4.2.2. To study the differences between these solutions it is convenient to introduce the dimensionless variables

$$\tilde{t} = \frac{Dt}{a^2}, \quad \tilde{r} = \frac{r}{a}, \quad \tilde{c} = \frac{c}{c_\infty k}, \quad \text{and} \quad \tilde{Q} = \frac{3}{4\pi}\frac{Q}{a^3 c_\infty k}.$$

Using these variables and the solution found using the equilibrium boundary condition we define

$$\tilde{Q}_e(\tilde{t}) = 1 - 6\alpha^2 \sum_{n=1}^{\infty} \frac{B_n}{\lambda_n^2} \sin\lambda_n\, e^{-\lambda_n^2 \tilde{t}}, \tag{4.18}$$

using Eq. 4.14, and

$$\tilde{c}_e(\tilde{r}, \tilde{t}) = 1 - \frac{2\alpha}{\tilde{r}} \sum_{n=1}^{\infty} B_n \sin \lambda_n \tilde{r}\, e^{-\lambda_n^2 \tilde{t}}, \tag{4.19}$$

using Eq. 4.11.

Analogously, we can use the solution found using the constant surface concentration boundary condition to define

$$\tilde{Q}_c(\tilde{t}) = 1 - \frac{6}{\pi^2} \sum_{n=1}^{\infty} \frac{1}{n^2}\, e^{-n^2\pi^2\tilde{t}}, \tag{4.20}$$

using Eq. 4.17, and

$$\tilde{c}_c(\tilde{r}, \tilde{t}) = 1 - \frac{2}{\pi\tilde{r}} \sum_{n=1}^{\infty} \frac{(-1)^n}{n} \sin n\pi\tilde{r}\, e^{-n^2\pi^2\tilde{t}}, \tag{4.21}$$

using Eq. 4.16. In Eqs. 4.18 through 4.21, we have set $c_0 = 0$.

Fig. 4.1a shows both $\tilde{Q}_e$ and $\tilde{Q}_c$ plotted as a function of $\tilde{t}$. For the dimensionless variables chosen here, $\tilde{Q}_c$ is represented by one curve while $\tilde{Q}_e$ is represented by a one-parameter family of curves. As the parameter α increases, the $\tilde{Q}_e$ curves approach the $\tilde{Q}_c$ curve until, at large α, the curves overlap and the $\tilde{Q}_e$ family of curves no longer changes with increasing α. In this large α limit, the solutions found using the two different boundary conditions become indistinguishable. Therefore, for any given $\tilde{t}$, $\tilde{Q}_c$ will always be greater than or approximately equal to $\tilde{Q}_e$. Fig. 4.1b illustrates this point even more clearly: as α increases, the lifetime (or e-folding time), $\tilde{\tau}_e$, of the corresponding $\tilde{Q}_e$ curve decreases and approaches the lifetime of the $\tilde{Q}_c$ curve, $\tilde{\tau}_c$.

Referring to the definition of α from Section 4.2.1, the results in Fig. 4.1 can be interpreted as follows: For physical values of D, D_g, and k, the amount of D_2O predicted using $\tilde{Q}_c$ at $\tilde{t}$ will always be larger than that predicted using $\tilde{Q}_e$. However, for large α the difference between $\tilde{Q}_c$ and $\tilde{Q}_e$ is negligible. For example, when $\alpha = 1000$ the difference between $\tilde{\tau}_c$ and $\tilde{\tau}_e$ is 0.67% and when $\alpha = 10000$ the difference is 0.067%. Therefore, there exists a wide range of D, D_g, and k where the choice of boundary condition has an insignificant effect on the results of the calculation. In Section 4.3.2, physical examples will be used to explore this conclusion in more detail. It will be shown that for many physically relevant cases the choice of solution when fitting data is inconsequential.

Fig. 4.2 shows concentration profiles at several $\tilde{t}$ for solutions found using the constant

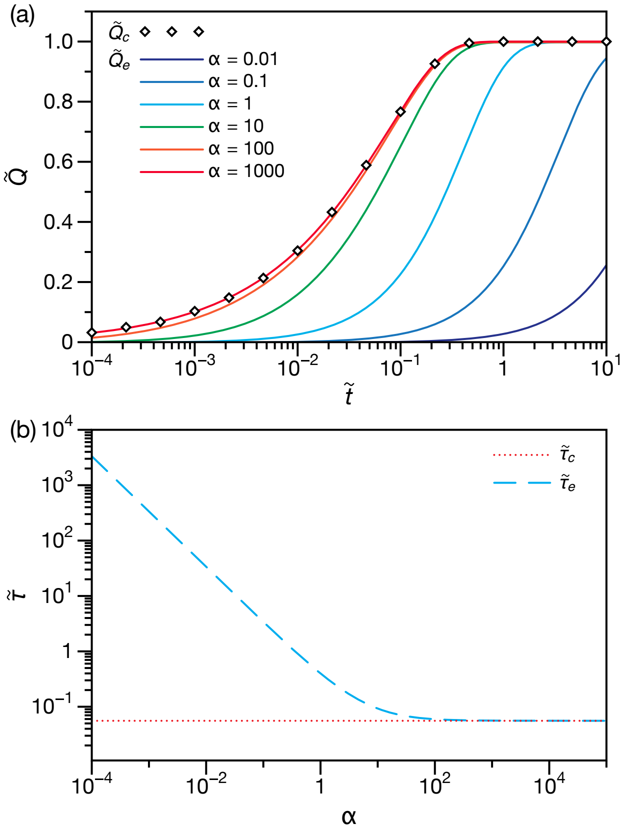

Figure 4.1: (a) Dimensionless total amount of D_2O in a particle, $\tilde{Q}$, as a function of the dimensionless time, $\tilde{t}$, and (b) the dimensionless lifetime, $\tilde{\tau}$, as a function of the parameter α, where $\alpha = D_g/(Dk)$ (see Section 4.2.1 for further details). Note that $\tilde{Q}(\tilde{\tau}) = 1 - 1/e$. Values of $\tilde{Q}_e$ and $\tilde{\tau}_e$ were calculated using the dimensionless closed-form solution to the diffusion problem found using the equilibrium boundary condition (Section 4.2.1). Values of $\tilde{Q}_c$ and $\tilde{\tau}_c$ were calculated using the dimensionless closed-form solution to the diffusion problem found using the constant surface concentration boundary condition (Section 4.2.2).

surface concentration boundary condition ($\tilde{c}_c$ in Fig. 4.2a) and the equilibrium boundary condition at three different values of α ($\tilde{c}_e$ in Fig. 4.2b-d). Similar to the discussion above concerning $\tilde{\tau}_e$ and $\tilde{\tau}_c$, $\tilde{c}_e$ is always less than $\tilde{c}_c$ for any given $\tilde{r}$ and $\tilde{t}$. It is apparent from Fig. 4.2 why this always has to be the case: at $\tilde{r} = 1$ (the surface), $\tilde{c}_c$ begins at its final concentration whereas $\tilde{c}_e$ does not. Therefore, $\tilde{c}_c$ is initially ahead of $\tilde{c}_e$ and cannot be overtaken. Of course, $\tilde{c}_e$ will catch up to $\tilde{c}_c$ at large $\tilde{t}$.

4.3.2 Isotopic Exchange in Binary Solution Droplets

Fig. 4.3 shows the calculated $Q(t)$ for aqueous sucrose particles at various temperatures and RHs. For the three temperatures listed in Fig. 4.3, the only RH where there is a non-negligible

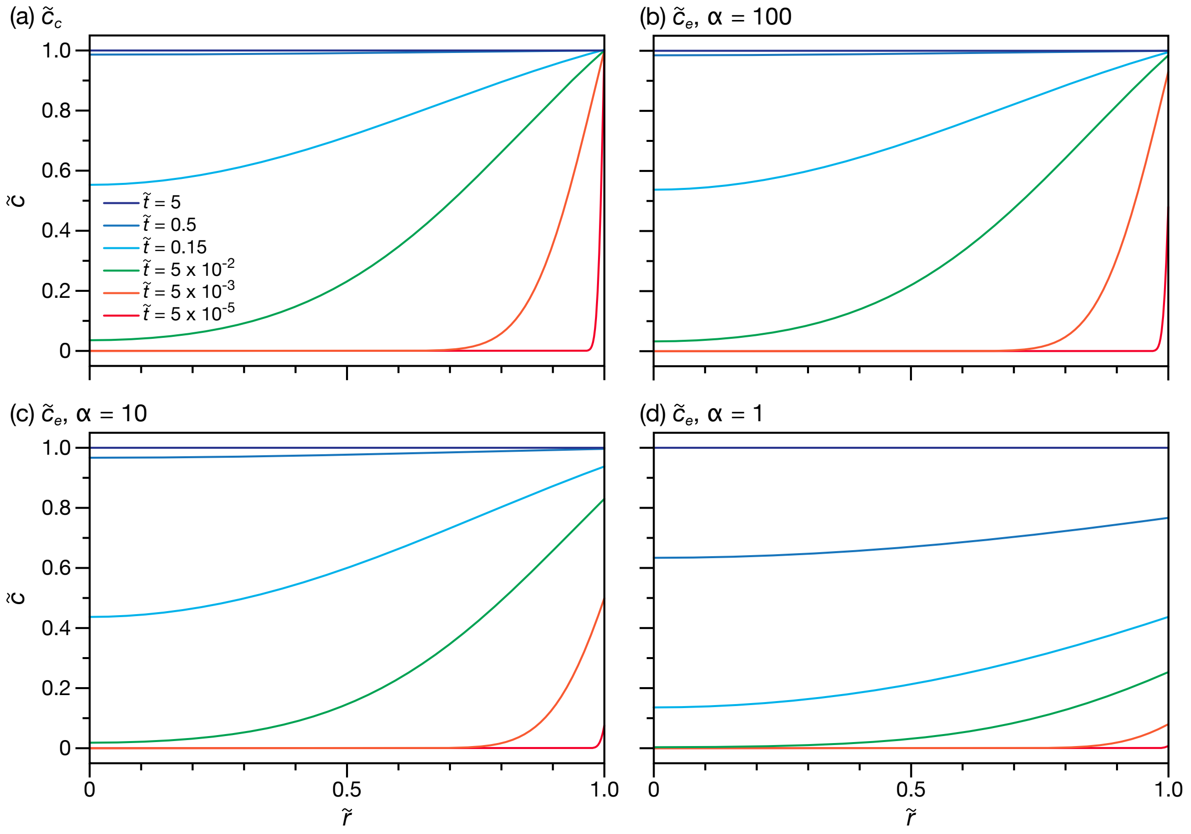

Figure 4.2: Concentration profiles calculated using dimensionless forms of (a) Eq. 4.16 and (b-d) Eq. 4.11 as a function of the dimensionless time, $\tilde{t}$.

difference between Q_e and Q_c is 80%. For the other, lower RHs, the curves for Q_e and Q_c overlap.

Fig. 4.4 explores isotopic exchange further by plotting the lifetimes τ_e and τ_c associated with Q_e and Q_c, respectively, as a function of RH for sucrose, citric acid, and shikimic acid droplets. In all cases, τ_e and τ_c diverge as the RH increases. In the context of Fig. 4.1b and the definition of α, this can be understood to be primarily the result of the fact that, for all these systems, D increases by several orders of magnitude from RH $= 0$ to 100% for any given T. Across this RH range, k also increases for all of these systems but not as rapidly as D (D_g only changes with T) so the product Dk only increases with increasing RH. Therefore, α decreases from RH $= 0$ to 100% and, at high RH, corresponds to values in Fig. 4.1b where large discrepancies between $\tilde{\tau}_e$ and $\tilde{\tau}_c$ exist yielding similar discrepancies between τ_e and τ_c in Fig. 4.4. What is also interesting in Fig. 4.4 is that at high RH all τ_e change very little as a

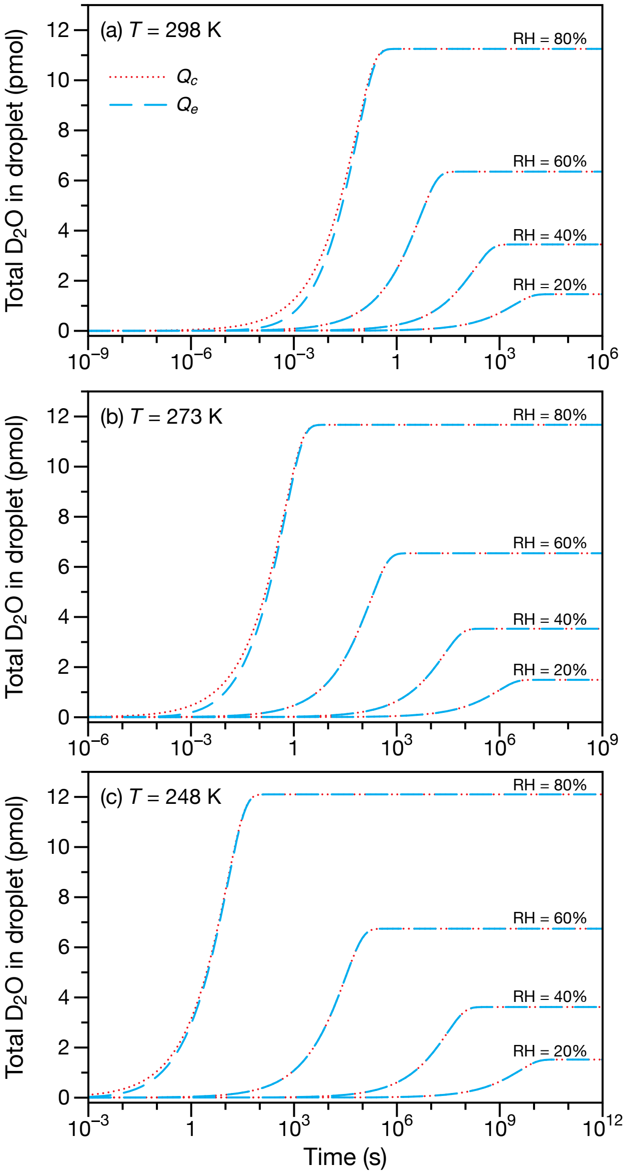

Figure 4.3: Calculated amount of D_2O in an aqueous sucrose droplet ($a = 5.0$ μm) during an isotopic exchange experiment at (a) $T = 298$ K, (b) $T = 273$ K, and (c) $T = 248$ K. Parameters for aqueous sucrose were taken from Ref. 15. Calculations were done using either Eq. 4.14 or Eq. 4.17. In all cases, the initial concentration of D_2O in the droplet, c_0, is zero.

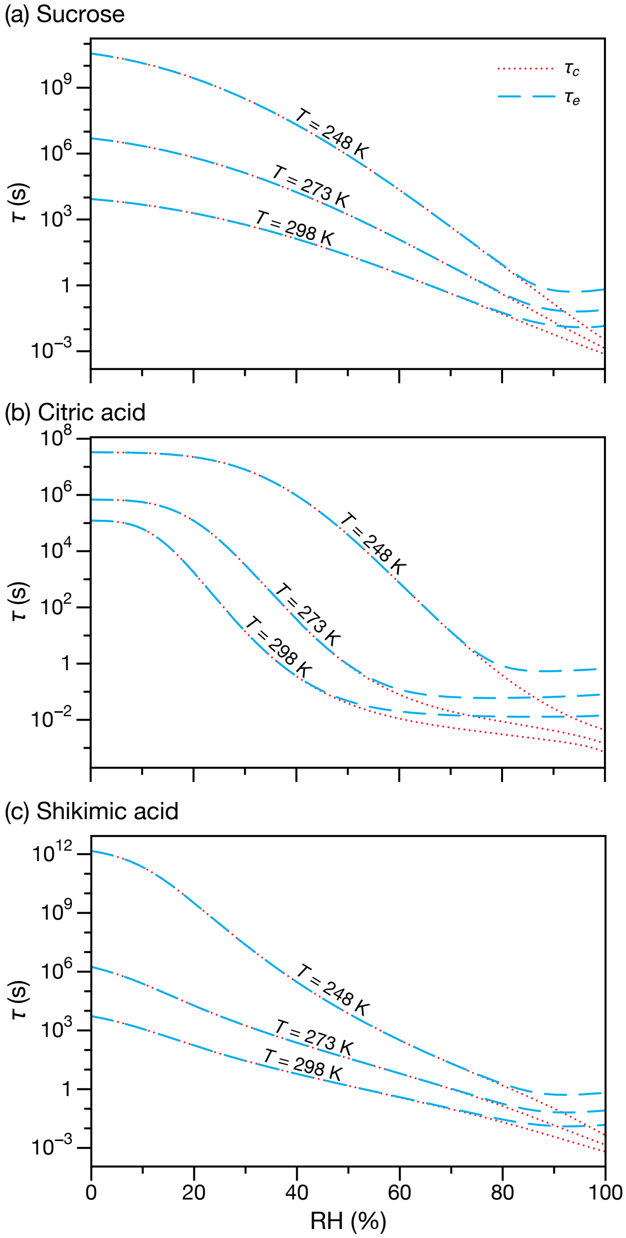

Figure 4.4: Lifetimes, τ_c and τ_e, as a function of RH at $T = 248$, 273, and 298 K for aqueous (a) sucrose, (b) citric acid, and (c) shikimic acid droplets ($a = 5.0$ μm). Values of τ_e were calculated using the closed-form solution to the diffusion problem found using the equilibrium boundary condition (Section 4.2.1). Values of τ_c were calculated using the closed-form solution to the diffusion problem found using the constant surface concentration boundary condition (Section 4.2.2). Parameters for aqueous sucrose were taken from Ref. 15, parameters for aqueous citric acid were taken from Ref. 80 and 195, and parameters for aqueous shikimic acid were taken from Ref. 83.

function of RH. Again, under these conditions, values of α fall in the region of Fig. 4.1b where the difference between $\tilde{\tau}_c$ and $\tilde{\tau}_e$ is large. Here, as the RH increases, α decreases causing $\tilde{\tau}_e$ to increase rapidly (at lower RHs where α was large, $\tilde{\tau}_e$ hardly varies with RH). However, as D also increases with RH for the aqueous systems in Fig. 4.4, the value of τ_e actually changes very little as $\tau_e = a^2\tilde{\tau}_e/D$.

Overall, Fig. 4.3 and 4.4 show that at low RH the choice of boundary condition is insignificant. However, at high RH the choice of boundary condition leads to solutions that give very different results. Fitting experimental measurements at these high RHs with either model will require different values of D. In such situations, using measurements of τ to determine D is not advised as Q is very sensitive to the boundary condition at $r = a$.

4.3.3 Discrepancies Between Retrieved Diffusion Coefficients

Recent studies have shown that there can be orders of magnitude difference between diffusion coefficients retrieved using isotopic exchange experiments and those retrieved using sorption/desorption experiments.[81,95] Understanding the source of these discrepancies is not straightforward as the methods of measurement and analysis differ between the two experiments. Isotopic exchange experiments have been performed on both disks on hydrophobic slides[93] and optically trapped, spherical particles.[95] These measurements have been analyzed using solutions to Eq. 4.1 with a constant concentration at the boundary $r = a$ (Eq. 4.15).[93,95] Water sorption/desorption experiments have been performed on both optically trapped and electrodynamically levitated particles.[15,80,81,83,90–92] Measurements have been modelled using the non-linear diffusion equation

$$\frac{\partial c}{\partial t} = \nabla \cdot (D(c)\nabla c), \tag{4.22}$$

where $D(c)$ is the concentration dependent diffusion coefficient.[15] This model involves a moving boundary (the radius of the particle changes during water sorption and desorption) and a non-linear boundary condition (Eq. 4.6). There is likely no analytical solution to this boundary value problem and numerical evaluation is required. Most measurements in water sorption/desorption experiments have been modelled using the finite difference method outlined by Zobrist *et al.*[15] Note that while convection is not present in Eq. 4.22, convective mass transfer is incorporated into the model of Zobrist *et al.* by adjusting the thickness of the shells that make up the spherical particle throughout the course of the simulation.

If the model used to simulate sorption/desorption experiments was modified to handle isotopic exchange experiments it should yield results identical to Q_e rather than Q_c due to the boundary condition at $r = a$. We tested such a modified version of the finite difference method described by Zobrist *et al.*[15] for the various conditions listed in Fig. 4.3. As expected, all numerical results matched the Q_e curves. Therefore, even when treating the same physical situation, the analytical model that has previously been used to analyze isotopic exchange experiments would produce different results than the numerical model that has been used to analyze sorption/desorption experiments. Consequently, this would lead to a retrieval of different diffusion coefficients.

In Ref. 95, it was found that discrepancies between diffusion coefficients (orders of magnitude) occurred when the RH was less than 30%. Large discrepancies were also reported in Ref. 81. Based on the results shown in Fig. 4.4, it appears that the choice of boundary condition has a negligible effect on the calculated time-dependent amount of D_2O in the droplet for RH less than 30%. As discussed in Section 4.3.2, differences only become significant at much larger RHs. At low RH in the systems of interest, the particle surface reaches its final concentration before significant exchange occurs. As a result, during the period of time when the majority of isotopic exchange occurs, Q_e and Q_c are indistinguishable. Therefore, fitting using either model in the RH range where the largest discrepancies have been reported would not lead to the observed differences in retrieved diffusion coefficients.

4.4 Conclusion

Closed-form expressions for two different models of isotopic exchange in spherical particles were presented. The main difference between these two models was the choice of boundary condition at $r = a$. One model assumed that D_2O in the liquid and vapor phase were in equilibrium and applied the steady-state assumption to D_2O in the vapor phase. The second model assumed that concentration of D_2O at $r = a$ and in the vapor phase was constant and did not change over time. The closed-form solutions that were found by solving the two resulting boundary value problems were analyzed. First, using dimensionless variables and, second, using parameters that describe the behaviour of three different binary aqueous particles. For systems of physical interest, the two models gave similar results at low RH across a range of temperatures. However, at high RH, there were always significant differences between predicted τ. Consequently, the models will yield different diffusion coefficients when used to fit measurements taken at high RH. Finally, the results were discussed in the context of recent reports that large deviations between diffusion coefficients retrieved using sorption/desorption experiments and isotopic exchange experiments had been found. It was concluded that the difference in boundary conditions used in the two models is not the source of the discrepancies seen in the diffusion coefficient retrievals as the differences occur at RHs and temperatures where both conditions give nearly identical results.

Chapter 5

Tracking Water Sorption in Glassy Aerosol Particles Using Morphology-Dependent Resonances

Abstract

Morphology-dependent resonances (MDRs) can serve as a sensitive probe of the size and composition of microspheres. While the utilization of MDRs to characterize homogeneous spheres is now routine, analysis of spherical particles with more complicated refractive index profiles can be extremely difficult and time consuming. In ultraviscous and glassy aerosol particles, the concentration profile of water during sorption often contains a sharp front that propagates from the particle surface to the particle center over time. Here we show that the MDR positions associated with this type of concentration profile closely match those of a spherical core-shell profile. Due to the similarities, a core-shell model can be used to simplify the analysis of MDR positions that are observed during water uptake by high viscosity aerosol particles. We examine the applicability and limitations of this core-shell model in the tracking of water sorption by single particles. Overall, the core-shell model allows for the radial position of a sharp diffusion front to be readily found using MDR positions observed during water sorption, making the analysis of light scattering measurements much faster and less error prone than previously used fitting schemes. Additionally, methods for calculating MDRs in spherical core-shell particles

are also discussed.

5.1 Introduction

In systems where the mass transport of a penetrant is not governed by linear diffusion, steep concentration gradients can form during sorption. This will result in a sharp concentration front that propagates through the medium during penetrant uptake. There are numerous reported examples of this type of behavior, the vast majority of which involve the diffusion of penetrants in glassy polymers.[196–202] In the atmospheric sciences, experiments studying water transport in high viscosity aerosol particles have demonstrated that similar fronts can readily form during sorption.[15,80,90]

Secondary organic aerosol (SOA) particles form in the troposphere when volatile organic compounds are oxidized and condense.[203] Depending on chemical composition and atmospheric conditions (i.e. relative humidity (RH) and temperature), the viscosity, η, of the condensed phase that forms these particles can vary tremendously. Typically, states are classified using ranges of η: low and high viscosity liquids ($\eta < 10^2$ Pa·s), semi-solids ($10^2 < \eta < 10^{12}$ Pa·s), and glasses ($\eta > 10^{12}$ Pa·s).[102] Simliar to the behavior described above, when the secondary organic matter is in a highly viscous state, water sorption will not be governed by linear diffusion. An accurate model of water transport in SOA particles is essential in order to understand hygroscopic growth and ice nucleation pathways.[81,204]

The discovery of glassy SOA particles in the atmosphere has stimulated broad research efforts. The central focus of the researchers is on the formation,[192,193,205] water uptake and diffusivity,[14,15,93,95,100,206] and viscosities[61,194,207] of SOA particles. Different techniques such as evaporation kinetics,[63,190] particle bounce,[192] the stability of two reverse-layered morphologies,[208] damped oscillations of spherical particles,[62] bead-mobility and poke-flow,[61] coalescence time analysis,[194] and particle dynamic shape factor[65] have been developed to evaluate the viscosity. All of these methods have provided insight into the dynamic behavior of atmospheric aerosols that are in the viscous state.

For particles in the micron size regime, resonances that appear in measured optical spectra, referred to as morphology-dependent resonances (MDRs) or whispering gallery mode

(WGM) resonances, have been used to track water uptake in single particle sorption experiments.[15,80,90,92,209] However, the retrieval of time-dependent concentration profiles from MDRs is complicated by two factors: First, unlike simpler systems (e.g. a spherical particle with a uniform concentration profile), there is no characteristic equation that allows for the direct calculation of MDRs for particles with arbitrary concentration profiles. MDR positions need to be found by identifying peaks in spectra calculated using a multilayer Mie code. Second, often the only practical way to generate concentration profiles that are used in the multilayer Mie scattering calculation is to numerically solve the boundary value problem that describes water transport. For instance, the diffusion of water in glassy aerosols is typically described by a concentration dependent diffusion coefficient resulting in a system where mass transfer is governed by nonlinear diffusion.[15,81,209] As the purpose of performing the sorption experiment is the retrieval of the parameters that go into these simulations (e.g. the coefficients in a parameterization that describes the concentration dependent diffusivity), it is necessary to run multiple simulations where parameters are iteratively changed as the error between calculated and observed MDR positions is minimized. This process is extremely time consuming.

Here, we demonstrate that water sorption in a high viscosity particle can be accurately tracked by approximating the time-dependent concentration profile as a traveling step-function. At any moment in time, the particle can be thought of as consisting of a core with a uniform concentration profile and a shell with a uniform concentration profile. An example of this approximation, plotted using the mole fraction of water, is illustrated in Fig. 5.1. The spherical geometry and the stepwise change in the refractive index allows electromagnetic scattering to be modeled using two concentric spheres (Fig. 5.2). The analytical solution to this scattering problem is known and, in this work, we present a characteristic equation for the MDRs of such a core-shell particle. With this equation, MDRs can be rapidly calculated enabling the tracking of both the core and shell positions over time through measured optical spectra. Diffusion simulations for a spherical particle undergoing water sorption are performed. The associated time-dependent refractive index profiles are used in conjunction with multilayer Mie theory to calculate both MDRs (Section 5.3.1) and extinction spectra (Section 5.3.2). Both sets of results are compared to resonances calculated using a core-shell model. It is shown

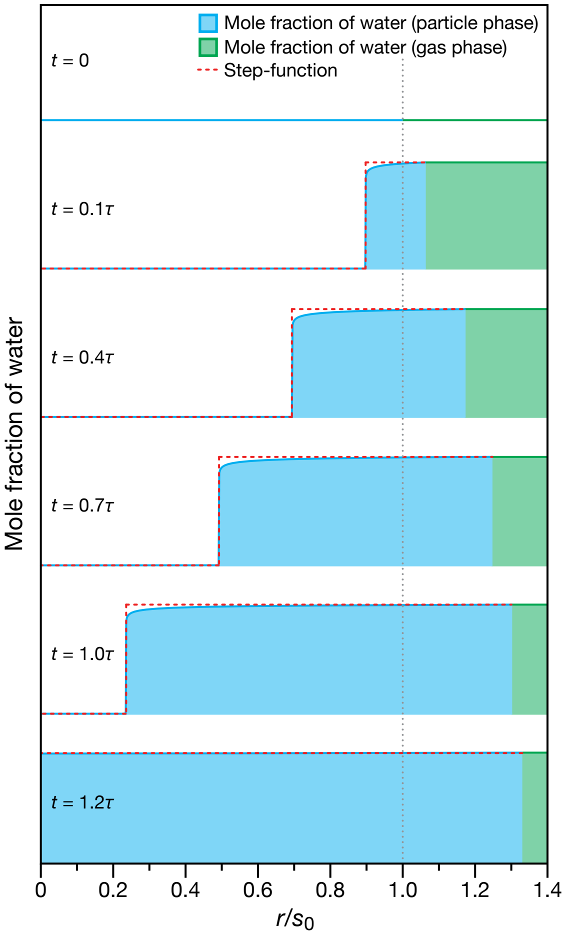

Figure 5.1: Examples of the mole fraction of water at various times, t, as a function of the radial coordinate, r, in a glassy particle with an initial radius, s_0, during water sorption. At $t = 0$, the RH outside the particle is zero but for $t > 0$ the RH is increased (to 95% in the simulations used to generate these curves). The characteristic time, τ, is the time at which the normalized sorption is equal to $1 - 1/e$. Step-functions are superimposed on the mole fraction curves inside the particle in order to highlight the similarities. The particle swells during sorption, hence the increase in the radius, $s(t)$, over time. The plots have been offset and the mole fraction scale is not shown. Parameters used in the simulations are discussed in Section 5.2.2.

that for these model systems, MDRs can be accurately reproduced using a core-shell model for situations of atmospheric interest. Overall, this provides a powerful method to monitor water sorption in single glassy particles.

5.2 Theory

5.2.1 Morphology-Dependent Resonances in Spherical Particles

5.2.1.1 Homogeneous Sphere

In a spherical particle with a uniform refractive index profile, MDRs occur when the denominators of the Mie scattering coefficients go to zero.[210] The resulting resonance condition can be written as

$$m\gamma \frac{j_n'(mz)}{j_n(mz)} = \frac{h_n^{(1)\prime}(z)}{h_n^{(1)}(z)} + \frac{1-\gamma}{z}, \tag{5.1}$$

where m is the relative refractive index of the sphere, $h_n^{(1)}$ is the spherical Hankel function of the first kind, which is defined by $h_n^{(1)} = j_n + iy_n$, the functions j_n and y_n are spherical Bessel functions of the first and second kinds, respectively, $\gamma = 1$ for the transverse electric (TE) polarization, $\gamma = 1/m^2$ for the transverse magnetic (TM) polarization, and z is the complex size parameter. For a particular mode number n and polarization p, there are an infinite number of solutions to Eq. 5.1 each of which corresponds to a mode order l. The solutions to Eq. 5.1 are complex resonant size parameters $z_{n,l,p} = x_{n,l,p} + iy_{n,l,p}$, where $x_{n,l,p}$ is the position of the resonance and $y_{n,l,p}$ is related to the full width at half-maximum of the resonance, $\Gamma_{n,l,p} = -2y_{n,l,p}$. To convert $x_{n,l,p}$ into a resonant wavelength, the definition $x = ka$, where $k = 2\pi/\lambda$, is used. Here, a is the radius of the sphere, and k and λ are the wavenumber and wavelength of light in the medium surrounding the sphere.

The infinite number of solutions to Eq. 5.1 for any n and p makes identifying $z_{n,l,p}$ for the desired l difficult. One method to overcome this issue is to use the explicit asymptotic formula for $x_{n,l,p}$ determined by Lam *et al.*[211] This approximate formula gives a suitable initial guess for $z_{n,l,p}$, the accuracy of which can then be improved by using Eq. 5.1. Detailed procedures for the accurate retrieval of $z_{n,l,p}$ have been discussed elsewhere.[86,88]

5.2.1.2 Two Concentric Spheres

Using the denominators of previously reported Mie coefficients for the scattering of an electromagnetic plane wave from two concentric spheres,[212] the following resonance condition can be obtained for a spherical core-shell particle:

$$\frac{j_n(m_2z_1)\left(1+m_1z_1j_n'(m_1z_1)/j_n(m_1z_1)\right)-q\left(j_n(m_2z_1)+m_2z_1j_n'(m_2z_1)\right)}{y_n(m_2z_1)\left(1+m_1z_1j_n'(m_1z_1)/j_n(m_1z_1)\right)-q\left(y_n(m_2z_1)+m_2z_1y_n'(m_2z_1)\right)}=$$
$$\frac{j_n(m_2z_2)\left(1+z_2h_n^{(1)\prime}(z_2)/h_n^{(1)}(z_2)\right)-v\left(j_n(m_2z_2)+m_2z_2j_n'(m_2z_2)\right)}{y_n(m_2z_2)\left(1+z_2h_n^{(1)\prime}(z_2)/h_n^{(1)}(z_2)\right)-v\left(y_n(m_2z_2)+m_2z_2y_n'(m_2z_2)\right)}, \quad (5.2)$$

where m_1 and m_2 are the refractive indices of the core and shell, respectively, relative to surrounding medium and z_1 and z_2 are the complex size parameters of the core and shell, respectively. For the TE polarization, $q = 1$ and $v = 1$ and, for the TM polarization, $q = m_1^2/m_2^2$ and $v = 1/m_2^2$. The core-shell geometry is depicted in Fig. 5.2. The inner size parameter, x_1, and outer size parameter, x_2, are related to the inner radius, a_1, and outer radius, a_2, through $x_1 = ka_1$ and $x_2 = ka_2$. The definition of the core to shell ratio is then $\alpha = x_1/x_2 = a_1/a_2$. Solutions to Eq. 5.2 will consist of two complex resonant size parameters, $z_{1,n,l,p}$ and $z_{2,n,l,p}$. Each pair of resonant size parameters that satisfies Eq. 5.2 will also satisfy $z_{1,n,l,p} = \alpha z_{2,n,l,p}$.

Unlike the case of the homogeneous sphere, there is currently no approximate, explicit formula for the resonances of a core-shell sphere that can provide suitable initial guesses for all cases of interest when solving Eq. 5.2. Explicit expressions have been developed in order to calculate resonances in the limits of thin shells[213] and systems with small differences between m_1 and m_2.[214] In general, though, the approach taken to solve Eq. 5.1 for a particular n, l, and p cannot be applied to Eq. 5.2. Therefore, we employ an alternative procedure to find electromagnetic resonances using Eq. 5.2: First, solutions from Eq. 5.1 are used as initial guesses to solve Eq. 5.2 and determine the resonances for a very thin shell (i.e. a system that is very close to a homogeneous sphere). The resonances from this very thin shell are then used as initial guesses to solve Eq. 5.2 for a slightly thicker shell. By increasing the shell thickness in small steps and using the resonances from the previous step as initial guesses for the current

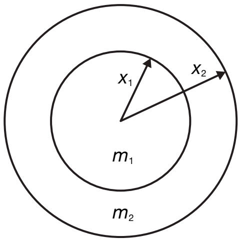

Figure 5.2: Geometry for a core-shell particle composed of two concentric spheres. The refractive index of the core is m_1 and the refractive index of the shell is m_2. The size parameter of the inner sphere is x_1 and the size parameter of the outer sphere is x_2. For an inner radius a_1 and outer radius a_2, the relationships between the size parameters and radii are $x_1 = ka_1$ and $x_2 = ka_2$, where $k = 2\pi/\lambda$ and λ is the wavelength of light in the medium surrounding the particle.

step, a set of resonances for all shell thicknesses can be found. In practical applications one is often interested in constructing a table of resonances to be used when comparing observations to calculations. The algorithm outlined here naturally produces such a table and, for such a task, it turns out to be just as rapid as a method involving an approximate explicit function.

Fig. 5.3 shows the position of the resonance of the outer sphere, $x_{2,n,l,p}$, for both polarizations as a function of α across a range of n and l for (i) $m_1 = 1.4$ and $m_2 = 1.6$ and (ii) $m_1 = 1.6$ and $m_2 = 1.4$. For $m_1 = 1.4$ and $m_2 = 1.6$, $x_{2,n,l,p}$ always decreases monotonically with decreasing α while, for $m_1 = 1.6$ and $m_2 = 1.4$, $x_{2,n,l,p}$ always increases monotonically with decreasing α. In all panels in Fig. 5.3, plateaus in $x_{2,n,l,p}$ are seen in the TE modes. The number of plateaus are equal to l. For TM modes, plateaus are not always seen but the absolute value of the slope of $x_{2,n,l,p}$ always decreases in the region where the TE modes plateau.

As l increases, the region over which $x_{2,n,l,p}$ continues to change becomes larger. For instance, in both Fig. 5.3e and f, the modes are still shifting even when $\alpha = 0.7$. The reason for this is that, for a given n, the peak mode energy will be located at smaller α with increasing l (i.e. the electromagnetic mode penetrates deeper into particle). Consequently, for a given spectral range, modes with higher l will be more sensitive to refractive index changes at smaller α and can probe compositional changes further from the particle surface.

Fig. 5.4 shows the internal and near-fields, plotted using the norm of the electric field, $|\vec{E}|$, divided by the amplitude of the electric field of the incident plane wave, E_0, at the MDR

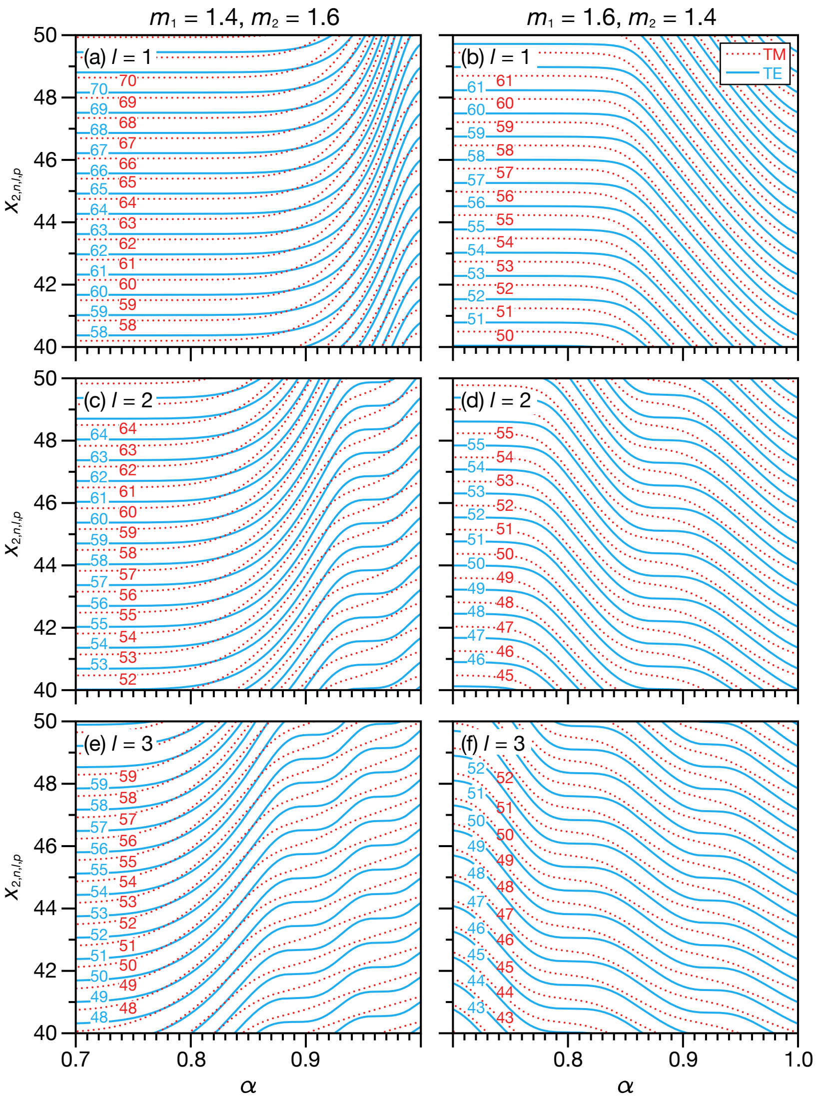

Figure 5.3: MDR positions, $x_{2,n,l,p}$, as a function of the ratio of the core size parameter to the shell size parameter, $\alpha = x_1/x_2$. See Fig. 5.2 for definitions of x_1 and x_2. Two sets of refractive indices are considered: $m_1 = 1.4$ and $m_2 = 1.6$ (a, c, and e) and $m_1 = 1.6$ and $m_2 = 1.4$ (b, d, and f). For $\alpha < 0.7$, $x_{2,n,l,p}$ changes very little for the mode orders, l, chosen here and these values are not shown. The mode numbers, n, are listed on the plots.

position of TE^2_{55} for four different α for the same two pairs of m_1 and m_2 shown in Fig. 5.3. For $m_1 = 1.4$ and $m_2 = 1.6$ (left panels), below $\alpha = 0.8$, there is little change in the plot of $|\vec{E}|/E_0$ and for $m_1 = 1.6$ and $m_2 = 1.4$ (right panels), below $\alpha = 0.7$, the plot of $|\vec{E}|/E_0$ no longer changes significantly. Both results are consistent with how $x_{2,n,l,p}$ changes in Fig. 5.3, specifically, the curves in Fig. 5.3c plateau at higher α than those in Fig. 5.3d.

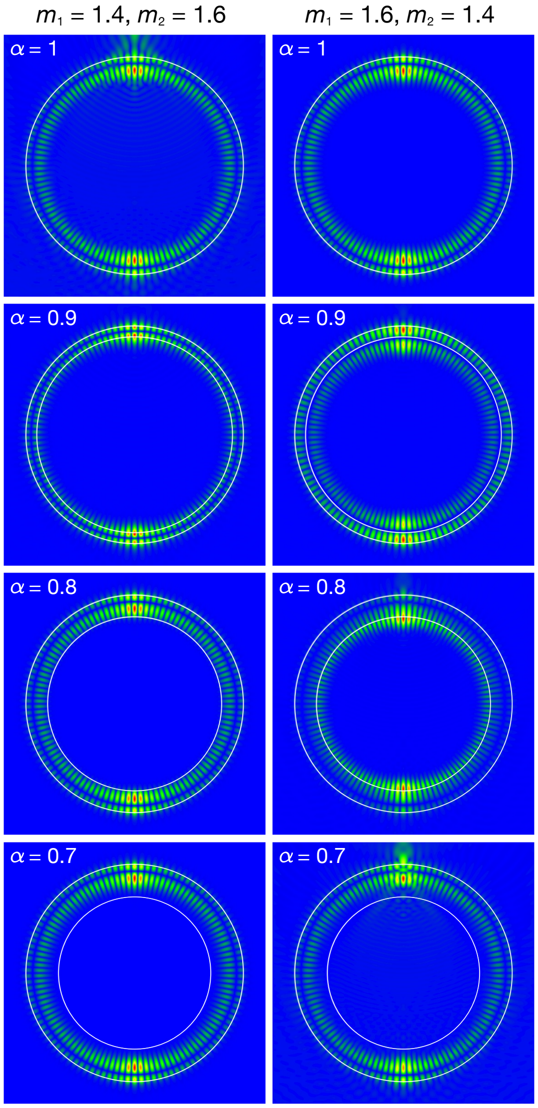

Figure 5.4: Internal and near-fields, plotted using $|\vec{E}|/E_0$, at the MDR position of TE_{55}^{2} for several core size parameter to shell size parameter ratios, α. Two sets of refractive indices are considered: $m_1 = 1.4$ and $m_2 = 1.6$ (left panels) and $m_1 = 1.6$ and $m_2 = 1.4$ (right panels). In each panel, the incident plane wave that excites the MDR is traveling from the bottom to the top. The two dimensional slices that are shown in the panels are normal to the polarization of the incident plane wave and parallel to the wave vector of the incident plane wave. Each slice passes through the centre of the sphere.

5.2.1.3 Multilayer Sphere

Methods for calculating the Mie scattering coefficients for a multilayered sphere have been discussed by several researchers.[215–219] From this body of work, the code published in Ref. 219 was demonstrated by the authors to accurately calculate extinction and scattering efficiencies for size parameters greater than 20. The positions of MDRs can be directly retrieved from scattering coefficients using the resonance condition $\mathrm{Re}(a_n) = 1$ for TM modes and $\mathrm{Re}(b_n) = 1$ for TE modes.[220] Therefore, existing multilayer code requires little modifications to determine x that satisfies the resonance condition. The drawback of using this resonance condition is that it will only yield accurate resonance positions for cases where the complex resonant size parameter is approximately real. This corresponds to sharp lines in the optical spectra of spheres with refractive index profiles that are approximately real. However, for MDRs that appear in optical spectra (our interest here), this is satisfactory as these resonances have narrow linewidths and are only observed in the spectra of weakly absorbing materials.

For a spherical particle with a radially dependent refractive index profile, scattering calculations can be performed by approximating the profile using a N layered sphere. In this discretization, each layer will have a constant refractive index that is equal to the value of the refractive index profile at the midpoint of the layer. With a large enough N, the multilayer sphere will accurately reproduce the optical properties of a sphere with the continuous refractive index profile. In all calculations performed here, $N = 2000$ was used.

5.2.2 Water Sorption

To simulate the time-dependent water sorption of a particle in response to a stepwise change in RH, the mass transport of water is treated using the model developed by Zobrist et al.[15] In this model, the particle is divided into N shells and the flux of water between shells is controlled by the concentration and temperature dependent diffusion coefficient, D, the radii of the shells, and the concentration difference between shells. The particle is spherical with a time-dependent radius, $s(t)$. At the surface of the particle, the mass transfer of water between condensed and vapour phases is controlled by a flux expression that assumes that the vapour phase concentration of water is in a steady state.[2] During the sorption simulation, at any point

r inside the droplet, it is assumed that the density instantaneously reaches its equilibrium value and the shell thicknesses are adjusted based on the equilibrium density.

All simulations performed here were done using the well-studied system of aqueous sucrose.[15,72,221] Sucrose has often been used as a proxy for oxidized organic material as aqueous sucrose readily forms a glass under a wide range of RH and temperature. The parameters for the diffusivity, density and water activity of aqueous sucrose were taken from Ref. 15. Using a Vogel-Fulcher-Tammann (VFT) type of equation,[222–224] the temperature dependance of $D(a_w, T)$ is expressed as:

$$\log_{10} D(a_w, T) = -\left(A(a_w) + \frac{B(a_w)}{T - T_0(a_w)}\right) \tag{5.3}$$

where T is the temperature, a_w is the activity of water, and the three VFT parameters (A, B and T_0) are:[15]

$$A(a_w) = 7 + 0.175(1 - 46.46(1 - a_w)), \tag{5.4}$$

$$B(a_w) = 262.867(1 + 10.53(1 - a_w) - 0.3(1 - a_w)^2), \tag{5.5}$$

$$T_0(a_w) = 127.9(1 + 0.4514(1 - a_w) - 0.5(1 - a_w)1.7). \tag{5.6}$$

The parameterization of a_w used here is[15]

$$a_w(T, w_s) = \frac{(1 + a w_s)}{(1 + b w_s + c w_s^2)} + (T - T^\theta)(d w_s + e w_s^2 + f w_s^3 + g w_s^4), \tag{5.7}$$

where w_s is weight fraction of sucrose in solution, $T^\theta = 298.15$ K and a to g are fit parameters: $a = -1$, $b = -0.99721$, $c = 0.13599$, $d = 0.001688$, $e = -0.005151$, $f = 0.009607$, and $g = -0.006142$.

Data from the Handbook of Chemistry and Physics[225] is used to parameterize the density of aqueous sucrose, ρ, as a function of w_s. This yields

$$\rho(w_s) = d_1 + d_2 w_s + d_3 w_s^2 + d_4 w_s^3 + d_5 w_s^4, \tag{5.8}$$

where $d_1 = 0.9989$, $d_2 = 0.3615$, $d_3 = 0.2964$, $d_4 = -0.3186$, and $d_5 = 0.24191$.

For optical calculations, a refractive index, m, is required. For aqueous sucrose we use

$$m = \beta_1 + \beta_2 w_s + \beta_3 w_s^2, \tag{5.9}$$

where the coefficients are $\beta_1 = 1.33327$, $\beta_2 = 0.13732$, and $\beta_3 = 0.07356$. This parameterization was determined by fitting tabulated refractive index measurements for aqueous sucrose.[226] For all sorption simulations, the temperature of the system was 298 K and the initial radius of the particle, s_0, was always 3.5 μm. At $t = 0$, the RH was changed from zero to its final value. For the simulations discussed in this work, the final value of the RH was either 35, 65, or 95%.

When analyzing water uptake, we make extensive use of the characteristic time, τ, which we define as

$$Q(\tau) = (1 - 1/e)(Q_\infty - Q_0), \tag{5.10}$$

where $Q(\tau)$ is the amount of water in the particle at $t = \tau$, Q_∞ is the amount of water in the particle as $t \to \infty$, and Q_0 is the amount of water in the particle at $t = 0$. Additionally we note that, while it is convenient to use a definition of τ based on Eq. 5.10, we in no way mean to imply that water uptake behaves as a first-order process in the systems that we are currently studying. However, by using the dimensionless quantities, such as t/τ and r/s_0, results can more immediately be applied across a range of T and s_0. Here, all calculations were performed using $s_0 = 3.5$ μm and $T = 298$ K and then nondimensionalized. When the RH is changed from zero to the final values of either 95, 65, or 35% this particular set of conditions yields τ of either 0.132, 4.79, or 449 s, respectively. However, if the calculations had instead been performed using $s_0 = 5.0$ μm and $T = 298$ K, then τ would be either 0.269, 9.75, or 914 s, for the final RH values of either 95, 65, or 35%, respectively. Despite the different values of τ, the nondimensionalized results would be identical. As another example, if the calculations had been performed using $s_0 = 3.5$ μm and $T = 273$ K, then τ would be either 0.803, 158, or 9.69×10^4 s, for the final RH values of either 95, 65, or 35%, respectively. Again, despite the different values of τ, the nondimensionalized results would be very similar to the previous cases (although not identical because many parameters in the calculation depend on T).

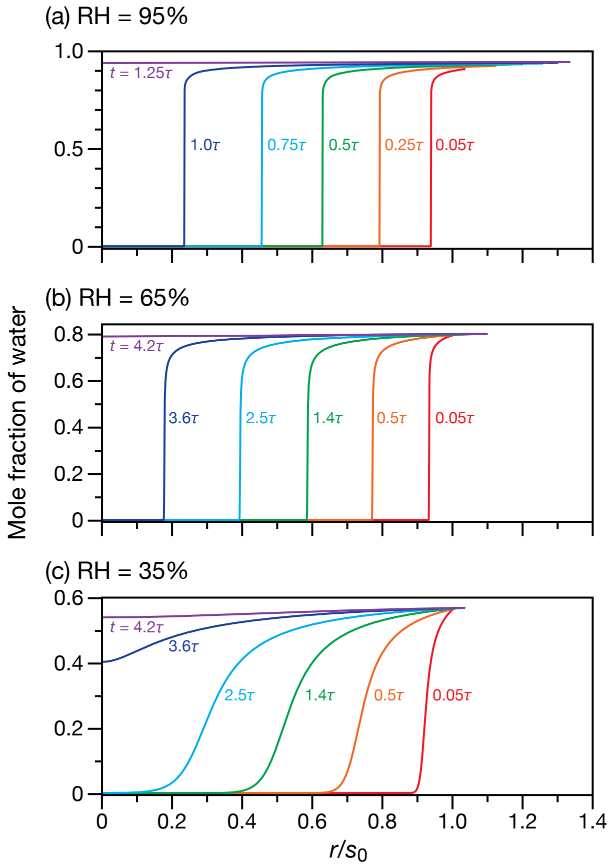

Figure 5.5: Mole fraction profiles at various times after a stepwise change in the RH surrounding the particle. At $t = 0$ the RH is changed from zero to the final values of either (a) 95, (b) 65, or (c) 35%. Parameters used in the simulations and the characteristic times, τ, are discussed in Section 5.2.2.

5.3 Results and Discussion

5.3.1 Behavior of MDRs During Water Sorption

Fig. 5.5 shows the mole fraction of water inside an aqueous sucrose droplet at various times after the RH is increased from zero to either (a) 95, (b) 65, or (c) 35%. As the increase in the final RH is lowered (i.e. going from Fig. 5.5a to c), approximating the profile as a traveling step-function becomes less accurate. For the lowest final RH (Fig. 5.5c), the mole fraction curves do not exhibit steep fronts and instead they begin to more closely resemble shapes that are characteristic of water sorption governed by linear diffusion.

For the mole fraction profiles in Fig. 5.5, corresponding refractive index profiles are shown in Fig. 5.6. The sets of profiles shown in Fig. 5.5 and 5.6 exhibit similar behavior, although

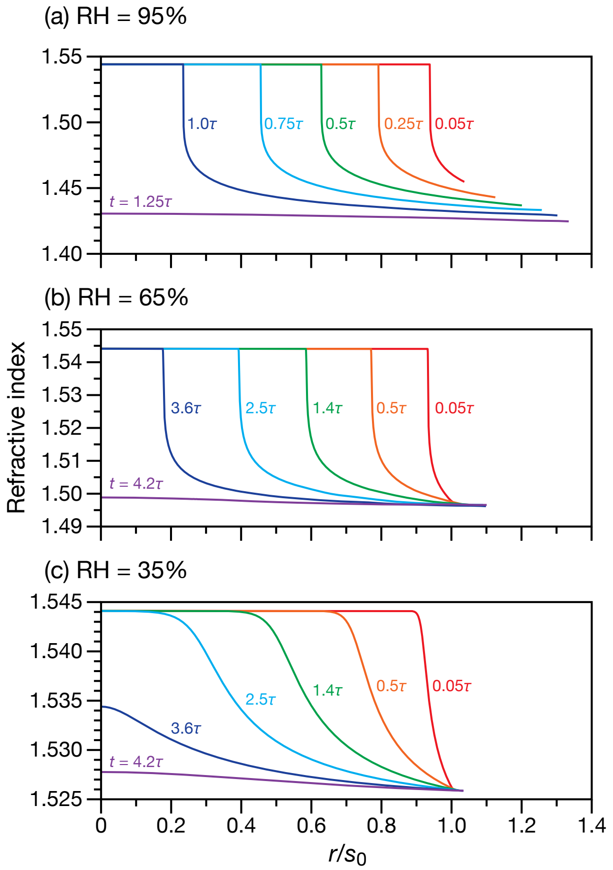

Figure 5.6: Refractive index profiles at various times after a stepwise change in the RH surrounding the particle. At $t = 0$ the RH is changed from zero to the final values of either (a) 95, (b) 65, or (c) 35%. Parameters used in the simulations and the characteristic times, τ, are discussed in Section 5.2.2.

the step-functions travel in opposite directions as the refractive index decreases with increasing mole fraction of water. In Fig. 5.6c, the maximum difference in refractive index at any time is very small and the profiles do not contain steep fronts. While MDRs can be very sensitive to even small changes in the refractive index,[86] retrieving accurate information about the mole fraction profile from observed mode positions will likely be impossible in this case (see Section 5.3.2). For Fig. 5.6a and b, larger maximum differences in the refractive index are seen and the refractive index profile more closely resembles a step-function. During sorption, observed shifts in resonance positions from such particles will be larger and, based on the simulations discussed in Section 5.3.2, the core-shell model will provide a more accurate model of the time-dependent refractive index profile.

Fig. 5.7 shows MDRs from the sorption simulations (calculated using the multilayer sphere method discussed in Section 5.2.1.3) along with core-shell MDRs (calculated using Eq. 5.2). Both sets of results are plotted as a function of α. For the sorption resonances, α is the position of the diffusion front at t divided by the radius of the particle at this time, $s(t)$. This is determined from the diffusion simulations by finding the radial coordinate at which the mole fraction profile is equal to the average of the initial and final mole fractions of water. For the core-shell calculations, α is the ratio of the inner to outer size parameter (defined in Section 5.2.1.2).

In order to calculate the core-shell resonances, m_1 and m_2 are required. Based on Fig. 5.6a and b, the refractive index profile in the core region is nearly uniform so m_1 can simply be set to the value of Eq. 5.9 when the weight fraction of sucrose is one. However, in the shell region the refractive index profile is not uniform. By setting m_2 to values that were close to the mean of the refractive index in this shell region, good fits between the multilayer and core-shell resonances could be found. The values of m_1 and m_2 used in the calculations are listed in the caption of Fig. 5.7. Overall, the correspondence between the core-shell and multilayer resonance positions is quite good from $\alpha = 0.7$ to 1. Below $\alpha = 0.7$, the resonances change very little as a function of α and they are not plotted in Fig. 5.7. The lack of sensitivity of MDR positions for $\alpha < 0.7$ means that tracking the diffusion front using the mode orders listed in Fig. 5.7 is not feasible.

In Section 5.2.1.2, we discussed how plateaus occur in the core-shell resonances when they are plotted as a function of α. In Fig. 5.7, the plateaus are seen in the core-shell resonances and in some of sorption resonances. Specifically, they are clearly observed in the TE modes of the sorption resonances in Fig. 5.7a to d. However, the plateaus are absent in sorption resonances in Fig. 5.7e and f (where the final RH was 35%). As was discussed, the corresponding time-dependent refractive index curves (Fig. 5.6c) for this system were poorly described using a traveling step-function. Therefore, it is not surprising that this characteristic behavior of core-shell resonances is absent in these sorption resonances.

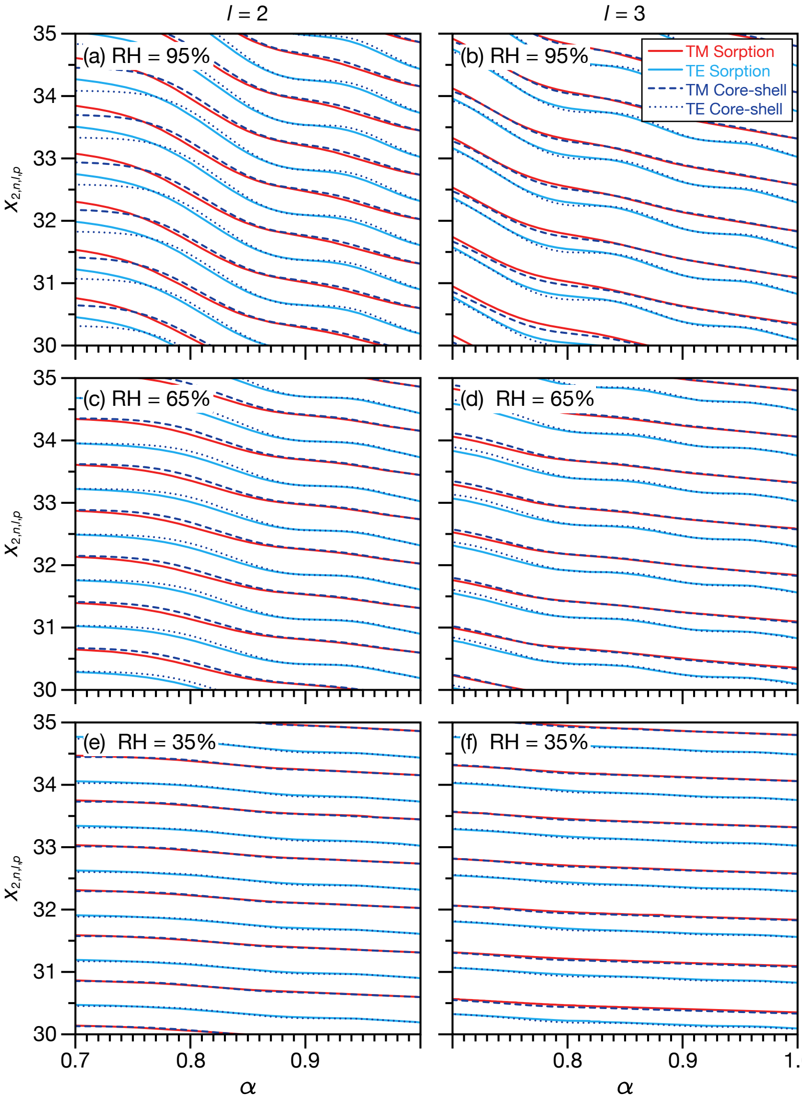

Figure 5.7: Comparison between MDR positions calculated for a particle during water sorption (solid lines) and a spherical core-shell model (dashed lines). For a particle during sorption, α is the position of the diffusion front at t divided by $s(t)$. For the core-shell particle, α is the ratio between the size parameter of the inner and outer sphere (see Fig. 5.2). For the core-shell MDR calculations, m_1 was set to 1.544 in all cases and m_2 was set to either 1.46 (a and b), 1.50 (c and d), or 1.53 (e and f). The mode numbers, n, are not listed on the plots. The mode orders, l, plotted here are $l = 2$ (a, c, and e) and $l = 3$ (b, d, and f)

5.3.2 Tracking the Diffusion Front Using Measured Optical Spectra

Fig. 5.7 illustrates that the correspondence between sorption and core-shell MDR positions can be quite good. However, there are two issues when extending this result to a sorption experiment: First, MDR positions are not measured directly and instead they are found using peak positions in optical spectra. Fortunately, most measured spectra contain narrow peaks whose positions will be nearly identical to MDR positions. Second, during a sorption experiment, the changing radius of the particle will not typically be known. Therefore, spectra (and peaks positions) are not directly measured in dimensionless size parameters. This means that analysis requires the additional parameter of the particle radius in order to compare peak positions to calculated MDRs.

We have previously reported an algorithm that can be used to fit observed peaks in the spectrum of a core-shell particle to calculated MDRs for a spherical core-shell particle.[101] In that work, the fitting algorithm was applied to core-shell particles that had undergone liquid-liquid phase separation. Here, we will apply the same algorithm to simulated sorption experiments. Fig. 5.8 shows extinction spectra at various times for a simulated sorption experiment. In this example, the RH is changed from zero to 95% at $t = 0$. Peak positions (in wavelength) extracted from these extinction spectra are fitted using our core-shell fitting algorithm. This was repeated for spectra calculated using changes in RH from zero to either 35 or 65%.

Fig. 5.9 compares α obtained through the peak position fitting process to α obtained by examining the mole fraction profiles. The mode order of all the fitted peaks was $l = 2$. In Fig. 5.9, the range of α shown is 0.75 to 1.0. Below $\alpha = 0.75$, the fits no longer accurately track the position of the diffusion front as the MDRs become insensitive to changes in α (as was discussed in Section 5.3.1). For the fits where the final RH is either 95% (Fig. 5.9a) or 65% (Fig. 5.9b), the correlation of α determined using the core-shell model to α determined from the front positions in the mole fraction profiles are good, although the 95% fit contains scattered points between $t = 0.15\tau$ and 0.175τ. Overall, for these cases it should be possible to track the diffusion front for values of α between 0.8 and 1.0 using measured optical spectra when using $l = 2$ modes during analysis. Finally, the accuracy of the fit where the final RH is

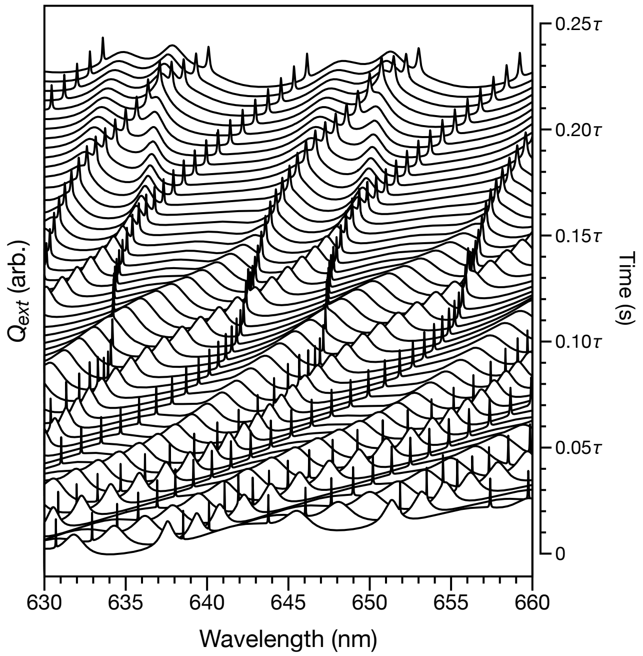

Figure 5.8: Calculated extinction efficiency, Q_{ext}, across a range of wavelengths at various times for a particle where the RH is changed from zero to 95% at $t = 0$. The initial radius, s_0, is 3.5 μm. The plots have been offset for clarity and the Q_{ext} scale is not shown. The characteristic times, τ, is discussed in Section 5.2.2.

35% is poor (Fig. 5.9c). This may initially seem surprising because the sorption and core-shell MDR positions for this case showed excellent agreement in Fig. 5.7e and f. However, the refractive index profile does not resemble a step-function (Fig. 5.6c). Additionally, Fig. 5.7e and f also demonstrate that the MDR positions change little with α. This lack of sensitivity to α means that using a core-shell model to fit measurements for this particular case will be prone to large errors and this is seen in the poor fits presented in Fig. 5.9c. Therefore, we can conclude that tracking is possible if (i) the refractive index profile can accurately be described by a step-function and (ii) the MDRs are sensitive to the moving diffusion front.

5.4 Conclusion

A method for tracking water uptake in high viscosity aerosols using MDR positions was presented. By approximating the time-dependent refractive index profile as a step-function, a core-shell model can be used to fit observed MDRs and track the position of the corresponding diffusion front. In Section 5.2.1.2, the characteristic equation for the MDRs of two concen-

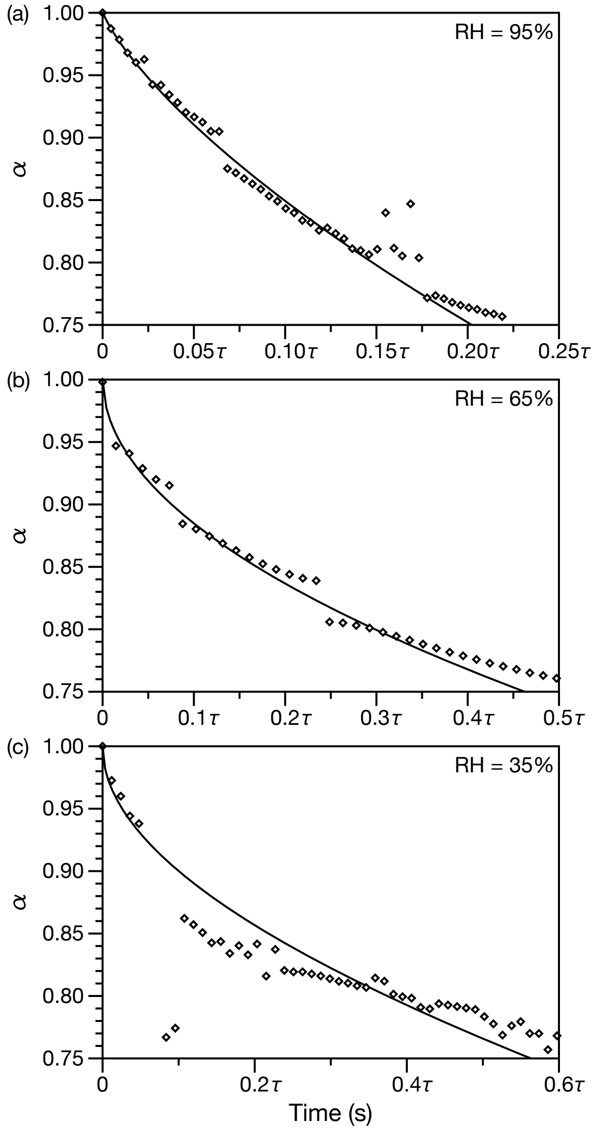

Figure 5.9: Comparison between α found by (i) taking the position of the diffusion front at t divided by $s(t)$ (solid lines) and (ii) fitting the MDR positions from sorption simulations using a core-shell model (points). In the core-shell model, α is the ratio between the size parameter of the inner and outer sphere (see Fig. 5.2). At $t = 0$ the RH is changed from zero to the final values of either (a) 95, (b) 65, or (c) 35%. The associated characteristic times, τ, are discussed in Section 5.2.2.

tric spheres was given (Eq. 5.2) and methods for calculating MDRs using this equation were discussed. In Section 5.3.1, calculated core-shell MDRs were compared to MDRs calculated for sorption simulations and the correlation was quite good (i.e. Fig. 5.7). In Section 5.3.2, MDR positions were taken from extinction plots for sorption simulations and fitted using the core-shell model. It was found that for systems where a sharp diffusion front existed, it is possible to track the front using observed MDRs and a core-shell model. However, when the refractive index profile was not well-described by a core-shell model the fit was not satisfactory. Furthermore, if the sensitivity of the MDRs to the position of the diffusion front was low then the fitting produced poor results. For the specific examples considered in Section 5.3.2 (i.e. particles whose second order modes had narrow peaks), this means that the front could not be tracked below $\alpha \sim 0.8$ as the sensitivity of the MDRs to α was very low between $\alpha = 0$ to 0.8.

Chapter 6

Conclusion

This thesis has presented three distinct studies of atmospheric aerosol particles. The first study (Chapters 2 and 3) focused on atmospheric dust aerosols on the regional scale and the other two studies (Chapters 4 and 5) concentrated on the physical properties of viscous secondary organic aerosols (SOAs) on the microscale. Each work has its own separate methodology, unique challenges, and interesting outputs.

The importance of research on dust particles comes from the fact that they can significantly impact (i) the Earth's climate system by changing the radiation budget, cloud optical properties and lifetimes, precipitation processes; (ii) the Earths ecosystems through marine and terrestrial biogeochemical cycles, hydrologic processes and, of course, (iii) human health. By studying the interactions between desertification and dust storms, we are able to better understand the role human and natural induced factors play in the magnitude of dust storms. The Middle East region is estimated to be the source of approximately 25% of the Earth's global dust particle emissions. This region has been experiencing dust storms for a long time, but recently the intensity and frequency of these dust storms have been touching areas which were not traditionally subject to these emissions. Yet, there is little known about sources, their location, intensity and evolution.

The aim of the first part of this thesis was then to answer two main questions: (1) where the dust source points are in the Middle East, (2) how the recent desertification can influence dust source activity and magnitude. This study combined satellite and ground-based remote sensing measurements, meteorological observations, image processing techniques, and model comparison to find the solutions.

In Chapters 2 and 3, we tried to respond to the two above questions respectively. Using the newly developed Middle East Dust Index applied to MODIS satellite data, we found that 247 different source points during the period of 2001-2012 have participated in dust storm generation in the Middle East region. We then considered a relationship between the recent desertified regions, over the past three decades, and the identified dust source points. We showed that major source points are located in Iraq and Syria, and by implementing the spectral mixture analysis on the Landsat TM images, a novel desertification map was extracted for these zones. It is found that 39% of all detected source points are located in this newly anthropogenically desertified area. The findings also indicated that identified severely desertified regions have intensified the number and the intensity of dust storms in the region, which require immediate concern at a global scale.

The second study of this thesis investigated diffusion in SOA particles. Recent studies have shown that these particles can exist in an amorphous state at very low relative humidities or temperatures. This is quite important because the resulting high viscosity substantially slows down the uptake of water by the particles as it impedes condensed phase diffusion. Current discrepancies in estimating SOA hygroscopicity limit us in understanding the magnitude of their influence on climate and air quality. This study aims to find an answer to the observed discrepancies in the context of isotopic water exchange.

In Chapter 4, a mathematical diffusion model was developed to examine the effect of surface boundary conditions on D_2O uptake during a water exchange experiment. The main goal of this study is to investigate water exchange in droplets using two different boundary conditions: (1) liquid and water at equilibrium at the surface and (2) a fixed surface concentration. Two analytical solutions were derived. To scrutinize the differences between these solutions, we introduced nondimensionalized variables of time, radial position, concentration, and sorption. Results showed that for any given dimensionless time, the dimensionless sorption with constant boundary condition is always greater or approximately equal to dimensionless sorption with equilibrium boundary condition. Our findings suggest that there are a wide range of physically applied cases where the type of analytical solution when fitting data can be insignificant. Comparing concentration profiles, we analogously observed that the nondimensionalized equilibrium concentration is always less than the equilibrium one. The reason is that in the constant condition, the concentration at the surface starts at the final RH. To explore this further, we studied water exchange of aqueous sucrose, aqueous citric acid, and aqueous shikimic acid droplets. Results are presented which illustrate the influence of high RH on increasing the discrepancies between corresponding constant lifetime and equilibrium lifetime in all cases. Our study showed that the type of boundary condition has a negligible effect on the calculated amount of D_2O in the droplet for low RH.

In the third study of this thesis, we investigated the optical characteristics of viscous particles during the diffusion process. We modeled the changes in the composition of a particle during the condensation process under varying RHs. We were interested to find out how the gradients in composition can change the scattering of electromagnetic radiation by particle. This is very important as models that link optical properties to hygroscopicity are highly desirable in the atmospheric chemistry community.

In Chapter 5, a characteristic equation to obtain the morphology dependent resonances (MDRs) of an aerosol particle with core-shell morphology was then presented. The main advantage of this equation is that it allows us to rapidly calculate the radiation scattering coefficients and hence the position of MDRs associated with a particle. The motivation of this work was the identification of the position of the diffusion front from experimental aerosol spectroscopy measurements. To test the MDRs predicted by the core-shell model, first we performed simulations for a dry sucrose particle during water uptake with varying ambient conditions. Then we used multilayer Mie theory to simulate the MDRs and extinction profile of the particle. We conclude that there is a good agreement between the predictions by the core-shell model and the simulations involving the sorption model. It is noted that the diffusion front does not have a sharp boundary between the core and the shell at low RHs. As a result, the characteristic behavior of the core-shell resonances are less observable or sometimes not identifiable. Finally, we performed simulations to test how deep a diffusion front could be tracked using MDRs. Near the beginning of water uptake, the front could be accurately tracked using the core-shell model.

Future Work

Dust aerosols have wide ranging complex physical and chemical properties that can also undergo atmospheric (photo) chemical aging and cloud nucleation processes. The Middle East is a high petroleum-producing hub, which generates substantial waste in air, water and soil, and thus the produced dust particles may have added chemical composition complexity as well as physical and radiative properties. Further integrated research (measurement and observation, laboratory and modeling) is needed to evaluate the local, regional and global impact of these new and mostly anthropogenic sources of dust aerosols on human health, air quality, extreme weather, hydrological cycle, radiation, cloud physics and Earth's biogeochemical cycles. Further international collaboration is also required in order to transfer knowledge into action towards the remediation and prevention of additional drastic desertification.

Further research is required to better understand the effect of viscosity on diffusion in viscous aerosols. One important focus can be on mathematical physics of diffusion and finding a relationship between diffusion coefficient and front position. Although the viscosity parameter is not directly utilized, use of diffusion coefficient can describe the particle state (e.g. solid or semi-solid) since it is a function of composition and temperature as well.

Present 3D atmospheric-chemistry transport models suffer from no representation or simplified parameterization of aerosol hygroscopisity in regional and global scales. For example, the Community Multi-scale Air Quality (CMAQ) modeling system that has only limited number of hypothetical lumped compounds (anonymized view) with no polarity, precludes consideration of water uptake of organic particulate matter.[227] Depending on aerosol microphysical scheme, Weather and Research Forecasting/Chemistry (WRF-Chem) model can have different aerosol water uptake treatment. The Georgia Tech/Goddard Global Ozone Chemistry Aerosol Radiation and Transport (GOCART) model and also The Modal Aerosol Model (MAM) use hygroscopicity parameter κ based on Kohler theory to explain the water content of aerosols. The other WRF-Chem schemes, Modal Aerosol Dynamic Model/Secondary Organic Aerosol Module (MADE/SORGAM) which is a modal approach for the aerosol size distribution with an equilibrium treatment for gas-particle partitioning, and also Model for Simulating Aerosol Interactions and Chemistry (MOSAIC) which is a sectional approach for the size distribution with a dynamic treatment for gas-particle partitioning, both treat only water uptake of inorganic constituents of aerosol. In Goddard Earth Observing System coupled with chemistry (GEOS-Chem) the calculation of water content of organic aerosols is be based on a relationship between relative humidity and growth factor of organic compounds. Therefore, in large scale atmospheric chemistry models, estimating water uptake by both organic and inorganic aerosols using the assumption of external mixing or average water contents of all simulated components fails to explain the potential effects of particle missing state and particle-phase morphology on aerosol water uptake and optical characteristics.[228] In order to see the possible impacts of these assumptions, there should be more sophisticated parameterizations of aerosol water uptake in aerosol microphysics schemes in the present atmospheric-chemistry models. The viscosity of organic aerosols needs to be addressed in calculating the aerosol water uptake. This would help to better understand part of current uncertainties in aerosol-cloud-radiation interactions.

Bibliography

[1] Ahrens, C. D. *Meteorology Today,* 9th ed.; Brooks/Col: Belmont, 2009.

[2] Pruppacher, H. R.; Klett, J. D. *Microphysics of Clouds and Precipitation*, 2nd ed.; Springer: Netherlands, 2010.

[3] Liou, K. N. *An Introduction to Atmospheric Radiation,* 2nd ed.; Academic Press: USA, 2002.

[4] Seinfeld, J. H.; Pandis, S. N. *Atmospheric Chemistry and Physics,* 2nd ed.; John Wiley & Sons: New York, 2006.

[5] Soden, B. J.; Wetherald, R. T.; Stenchikov, G. L.; Robock, A. Global Cooling after the Eruption of Mount Pinatubo: A Test of Climate Feedback by Water Vapor. *Science* **2002**, *296*, 727-730.

[6] Schneider, T.; O'Gorman, P. A.; Levine, X. J. Water Vapor and the Dynamics of Climate Changes. *Rev. Geophys.* **2010**, *48.*

[7] Bevis, M.; Businger, S.; Herring, T. A.; Rocken, C.; Anthes, R. A.; Ware, R. H. GPS Meteorology: Remote Sensing of Atmospheric Water Vapor using the Global Positioning System. *J. Geophys. Res. Atmos.* **1992**, *97*, 15787-15801.

[8] Shuttleworth, W. J. *Water Vapor in the Atmosphere, in Terrestrial Hydrometeorology*, John Wiley & Sons: West Sussex, 2012.

[9] Boucher, O.; Randall, D.; Artaxo, P.; Bretherton, C.; Feingold, G.; Forster, P.; Kerminen, V.-M.; Kondo, Y.; Liao, H.; Lohmann, U.; et al. *Clouds and Aerosols. In: Climate Change 2013: The Physical Science Basis. Contribution of Working Group I to the Fifth Assessment Report of the Intergovernmental Panel on Climate Change,* edited by: Stocker, T. F., Qin, D., Plattner, G.-K., Tignor, M., Allen, S. K., Boschung, J., Nauels, A., Xia, Y., Bex V., Midgley, P. M., Eds.; Cambridge University Press; Cambridge, U.K., and New York, 2013.

[10] Zhang, R.; Khalizov, A.; Wang, L.; Hu, M.; Xu, W. Nucleation and Growth of Nanoparticles in the Atmosphere. *Chem. Rev.* **2011**, *112*, 1957-2011.

[11] Kulmala, M.; Petaja, T.; Ehn, M.; Thornton, J.; Sipila, M.; Worsnop, D. R.; Kerminen, V. M. Chemistry of Atmospheric Nucleation: on the Recent Advances on Precursor Characterization and Atmospheric Cluster Composition in Connection with Atmospheric New Particle Formation. *Annu. Rev. Phys. Chem.* **2014**, *65*, 21-37.

[12] Jacob, D. *Introduction to Atmospheric Chemistry*, Princeton University Press; Princeton, 1999.

[13] Stock, M.; Cheng, Y. F.; Birmili, W.; Massling, A.; Wehner, B.; Mller, T.; Leinert, S.; Kalivitis, N.; Mihalopoulos, N.; Wiedensohler, A. Hygroscopic Properties of Atmospheric Aerosol Particles over the Eastern Mediterranean: Implications for Regional Direct Radiative Forcing under Clean and Polluted Conditions. *Atmos. Chem. Phys.* **2011**, *11*, 4251-4271.

[14] Pajunoja, A.; Lambe, A. T.; Hakala, J.; Rastak, N.; Cummings, M. J.; Brogan, J. F.; Hao, L.; Paramonov, M.; Hong, J.; Prisle, N. L.; Malila, J. Adsorptive Uptake of Water by Semisolid Secondary Organic Aerosols. *Geophys. Res. Lett.* **2015**, *42*, 3063-3068.

[15] Zobrist, B.; Soonsin, V.; Luo, B. P.; Krieger, U. K.; Marcolli, C.; Peter, T.; Koop, T. Ultra-Slow Water Diffusion in Aqueous Sucrose Glasses. *Phys. Chem. Chem. Phys.* **2011**, *13*, 3514-3526.

[16] Tong, H.-J.; Reid, J. P.; Bones, D. L.; Luo, B. P.; Krieger, U. K. Measurements of the Timescales for the Mass Transfer of Water in Glassy Aerosol at Low Relative Humidity and Ambient Temperature. *Atmos. Chem. Phys.* **2011**, *11*, 4739-4754.

[17] Kreisberg, N. M.; Stolzenburg, M. R.; Hering, S. V.; Dick, W. D.; McMurry, P. H. A New Method for Measuring the Dependence of Particle Size Distributions on Relative Humidity, with Application to the Southeastern Aerosol and Visibility Study, *J. Geophys. Res.* **2001**, *106*, 935-14.

[18] Hegg, D. A.; Covert, D. S.; Crahan, K. K.; Jonsson, H. H.; Liu, Y. Measurements of Aerosol SizeResolved Hygroscopicity at Sub and Supermicron Sizes. *Geophys. Res. Lett.* **2006**, *33*.

[19] Hersey, S. P.; Sorooshian, A.; Murphy, S. M.; Flagan, R. C.; Seinfeld, J. H. Aerosol Hygroscopicity in the Marine Atmosphere: a Closure Study using High-Time-Resolution, Multiple-RH DASH-SP and Size-Resolved C-ToF-AMS Data. *Atmos. Chem. Phys.* **2009**, *9*, 2543-2554.

[20] Fierz-Schmidhauser, R.; Zieger, P.; Wehrle, G.; Jefferson, A.; Ogren, J. A.; Baltensperger, U.; Weingartner, E. Measurement of Relative Humidity Dependent Light Scattering of Aerosols. *Atmos. Meas. Tech.* **1010**, *3*, 39-50.

[21] Day, D. E.; Malm, W. C. Aerosol Light Scattering Measurements as a Function of Relative Humidity: a Comparison Between Measurements Made at Three Different Sites. *Atmos. Environ.* **2001**, *35*, 5169-5176.

[22] Zieger, P.; Fierz-Schmidhauser, R.; Weingartner, E.; Baltensperger, U. Effects of Relative Humidity on Aerosol Light Scattering: Results from Different European Sites. *Atmos. Chem. Phys.* **2013**, *13*, 10609-10631.

[23] Ghan, S. J.; AbdulRazzak, H.; Nenes, A.; Ming, Y.; Liu, X.; Ovchinnikov, M.; Shipway, B.; Meskhidze, N.; Xu, J.; Shi, X. Droplet Nucleation: PhysicallyBased Parameterizations and Comparative Evaluation. *J. Adv. Model. Earth Syst.* **2011**, *3*.

[24] Twomey, S. The Nuclei of Natural Cloud Formation Part II: The Supersaturation in Natural Clouds and the Variation of Cloud Droplet Concentration. *Pure Appl. Geophys.* **1959**, *43*, 243-249.

[25] AbdulRazzak, H.; Ghan, S. J. A Parameterization of Aerosol Activation 3. Sectional Representation. *J. Geophys. Res. Atmos.* **2002**, *107*.

[26] Nenes, A.; Seinfeld, J. H. Parameterization of Cloud Droplet Formation in Global Climate Models. *J. Geophys. Res. Atmos.* **2003**, *108*.

[27] Ming, Y.; Ramaswamy, V.; Donner, L. J.; Phillips, V. T. A New Parameterization of Cloud Droplet Activation Applicable to General Circulation Models. *J. Atmos. Sci.* **2006**, *63*, 1348-1356.

[28] Fountoukis, C.; Nenes, A. Continued Development of a Cloud Droplet Formation Parameterization for Global Climate Models. *J. Geophys. Res. Atmos.* **2005**, *110*.

[29] Feingold, G. Modeling of the First Indirect Effect: Analysis of Measurement Requirements. *Geophys. Res. Lett.* **2003**, *30*.

[30] McFiggans, G.; Artaxo, P.; Baltensperger, U.; Coe, H.; Facchini, M. C.; Feingold, G.; Fuzzi, S.; Gysel, M.; Laaksonen, A.; Lohmann, U.; Mentel, T. F. The Effect of Physical and Chemical Aerosol Properties on Warm Cloud Droplet Activation. *Atmos. Chem. Phys.* **2006**, *6*, 2593-2649.

[31] Asmi, A.; Wiedensohler, A.; Laj, P.; Fjaeraa, A. M.; Sellegri, K.; Birmili, W.; Weingartner, E.; Baltensperger, U.; Zdimal, V.; Zikova, N.; Putaud, J. P. Number Size Distributions and Seasonality of Submicron Particles in Europe 2008-2009. *Atmos. Chem. Phys.* **2011**, *11*, 5505-5538.

[32] Petters, M. D.; Kreidenweis, S. M. A Single Parameter Representation of Hygroscopic Growth and Cloud Condensation Nucleus Activity, *Atmos. Chem. Phys.* **2007**, *7*, 1961-1971

[33] Kumar, P.; Sokolik, I. N.; Nenes, A. Measurements of Cloud Condensation Nuclei Activity and Droplet Activation Kinetics of Fresh Unprocessed Regional Dust Samples and Minerals. *Atmos. Chem. Phys.* **2011**, *11*, 3527-3541.

[34] Zhang, Y.; Zhang, X.; Wang, K.; He, J.; Leung, L. R.; Fan, J.; Nenes, A. Incorporating an Advanced Aerosol Activation Parameterization into WRFCAM5: Model Evaluation and Parameterization Intercomparison. *J. Geophys. Res. Atmos.* **2015**, *120*, 6952-6979.

[35] Köhler, H. Zur Thermodynamic der Kondensation an Hygroskopischen Kernen un Bemerkungen uber das Zusammenfliessen der Tropfen. *Medd. Met. Hydro. Anst. Stockholm* **1926**.

[36] Yau, M. K.; Rogers, R. R. *A Short Course in Cloud Physics*, Butterworth-Heinemann: USA, 1996.

[37] Thomson, W. 4. On the Equilibrium of Vapour at a Curved Surface of Liquid. *Proc. R. Soc. Edinburgh*, **1872**, *7*, 63-68.

[38] Hoose, C.; Mohler, O. Heterogeneous Ice Nucleation on Atmospheric Aerosols: A Review of Results from Laboratory Experiments. *Atmos. Chem. Phys.* **2012**, *12*, 9817-9854.

[39] Murray, B. J.; O'sullivan, D.; Atkinson, J. D.; Webb, M. E. Ice Nucleation by Particles Immersed in Supercooled Cloud Droplets. *Chem. Soc. Rev.*, **2012**, *41*, 6519-6554.

[40] Bohren, C. F.; Huffman, D. R. *Absorption and Scattering of Light by Small Particles*, Wiley: New York, 1983.

[41] Symes, R.; Sayer, R. M.; Reid, J. P. Cavity Enhanced Droplet Spectroscopy: Principles, Perspectives and Prospects. *Phys. Chem. Chem. Phys.* **2004**, *6*, 474-487.

[42] Ghan, S.; Penner, J. E. ARM-Led Improvements in Aerosols in Climate and Climate Models. *Meteorol. Monogr.* **2016**, *57*, 27-1.

[43] Fan, J.; Wang, Y.; Rosenfeld, D.; Liu, X. Review of Aerosol-Cloud Interactions: Mechanisms, Significance, and Challenges. *J. Atmos. Sci.* **2016**, *73*, 4221-4252.

[44] Kaufman, Y. J.; Tanré, D.; Gordon, H. R.; Nakajima, T.; Lenoble, J.; Frouin, R.; Grassl, H.; Herman, B. M.; King, M. D.; Teillet, P. M. Passive Remote Sensing of Tropospheric Aerosol and Atmospheric Correction for the Aerosol Effect. *J. Geophys. Res. Atmos.* **1997**, *102*, 16815-16830.

[45] Burrows, J. P.; Platt, U.; Borrell, P. Tropospheric Remote Sensing from Space. In *The Remote Sensing of Tropospheric Composition from Space*, Springer: Berlin Heidelberg, 2011.

[46] Satheesh, S. K.; Ramanathan, V. Large Differences in Tropical Aerosol Forcing at the Top of the Atmosphere and Earth's Surface. *Nature* **2000**, *405*, 60-63.

[47] Pöschl, U.; Shiraiwa, M. Multiphase Chemistry at the Atmosphere-Biosphere Interface Influencing Climate and Public Health in the Anthropocene. *Chem. Rev.* **2015**, *115*, 4440-4475.

[48] Wang, K.; Dickinson, R. E.; Liang, S. Clear Sky Visibility Has Decreased over Land Globally from 1973 to 2007. *Science* **2009**, *323*, 1468-1470.

[49] Sokolik, I. N.; Toon, O. B. Incorporation of Mineralogical Composition into Models of the Radiative Properties of Mineral Aerosol from UV to IR Wavelengths. *J. Geophys. Res.* **1999**, *104*, 9423-9444.

[50] Nickovic, S.; Vukovic, A.; Vujadinovic, M.; Djurdjevic, V.; Pejanovic, G. Technical Note: High-resolution Mineralogical Database of Dust-Productive Soils for Atmospheric Dust Modeling. *Atmos. Chem. Phys.* **2012**, *12*, 845-855.

[51] Formenti, P.; Schütz, L.; Balkanski, Y.; Desboeufs, K.; Ebert, M.; Kandler, K.; Petzold, A.; Scheuvens, D.; Weinbruch, S.; Zhang, D. Recent Progress in Understanding Physical and Chemical Properties of African and Asian Mineral Dust. *Atmos. Chem. Phys.* **2011**, *11*, 8231-8256.

[52] Jimenez, J. L.; Canagaratna, M. R.; Donahue, N. M.; Prevot, A. S. H.; Zhang, Q.; Kroll, J. H.; DeCarlo, P. F.; Allan, J. D.; Coe, H.; Ng, N. L; Aiken, A. C. Evolution of Organic Aerosols in the Atmosphere. *Science*, **2009**, *326*, 1525-1529.

[53] Hallquist, M.; Wenger, J. C.; Baltensperger, U.; Rudich, Y.; Simpson, D.; Claeys, M.; Dommen, J.; Donahue, N. M.; George, C.; Goldstein A. H.; Hamilton, J. F. The formation, Properties and Impact of Secondary Organic Aerosol: Current and Emerging Issues. *Atmos. Chem. Phys.* **2009**, *9*, 5155-5236.

[54] Kroll, J. H.; Seinfeld, J. H. Chemistry of Secondary Organic Aerosol: Formation and Evolution of Low-Volatility Organics in the Atmosphere. *Atmos. Environ.* **2008**, *42*, 3593-3624.

[55] Li, Y., Pöschl, U.; Shiraiwa, M. Molecular Corridors and Parameterizations of Volatility in the Chemical Evolution of Organic Aerosols.*Atmos. Chem. Phys.* **2016**, *16*, 3327-3344.

[56] Denjean, C.; Formenti, P.; Picquet-Varrault, B.; Pangui, E.; Zapf, P.; Katrib, Y.; Giorio, C.; Tapparo, A.; Monod, A.; Temime-Roussel, B; Decorse, P. Relating Hygroscopicity and Optical Properties to Chemical Composition and Structure of Secondary Organic Aerosol Particles Generated from the Ozonolysis of α-pinene. *Atmos. Chem. Phys.* **2015**, *15*, 3339-3358.

[57] Li, K.; Li, J.; Liggio, J.; Wang, W.; Ge, M.; Liu, Q.; Guo, Y. C.; Tong, S.; Li, J.; Peng, C; Jing, B. Enhanced Light-scattering of Secondary Organic Aerosols by Multiphase Reactions. *Environ. Sci. Technol.* **2017**, DOI: 10.1021/acs.est.6b03229

[58] Moise, T.; Flores, J. M.; Rudich, Y. Optical Properties of Secondary Organic Aerosols and their Changes by Chemical Processes. *Chem. Rev.* **2015**, *115*, 4400-4439.

[59] Laskin, A.; Laskin, J.; Nizkorodov, S. A. Chemistry of Atmospheric Brown Carbon. *Chem. Rev.* **2015**, *115*, 4335-4382.

[60] Mikhailov, E.; Vlasenko, S.; Martin, S. T. Amorphous and Crystalline Aerosol Particles Interacting with Water Vapor: Conceptual Framework and Experimental Evidence for Restructuring, Phase Transitions. *Atmos. Chem. Phys.* **2009**, *9*, 9491-9522.

[61] Renbaum-Wolff, L.; Grayson, J. W.; Bateman, A. P.; Kuwata, M.; Sellier, M.; Murray, B. J.; Shilling, J. E.; Martin, S. T.; Bertram, A. K. Viscosity of α-Pinene Secondary Organic Material and Implications for Particle Growth and Reactivity. *Proc. Natl. Acad. Sci.* **2013**, *110*, 8014-8019.

[62] Power, R. M.; Simpson, S. H.; Reid, J. P.; Hudson, A. J. The Transition From Liquid to Solid-Like Behaviour in Ultrahigh Viscosity Aerosol Particles. *Chem. Sci.* **2013**, *4*, 2597-2604.

[63] Abramson, E.; Imre, D.; Bernek, J.; Wilson, J.; Zelenyuk, A. Experimental Determination of Chemical Diffusion Within Secondary Organic Aerosol Particles. *Phys. Chem. Chem. Phys.*, **2013**, *15*, 2983-2991.

[64] Booth, A. M.; Murphy, B.; Riipinen, I.; Percival, C. J.; Topping, D. O. Connecting Bulk Viscosity Measurements to Kinetic Limitations on Attaining Equilibrium for a Model Aerosol Composition. *Environ. Sci. Technol.* **2014**, *48*, 9298-9305.

[65] Zhang, Y.; Sanchez, M. S.; Douet, C.; Wang, Y.; Bateman, A. P.; Gong, Z.; Kuwata, M.; Renbaum-Wolff, L.; Sato, B. B.; Liu, P. F.; et al. Changing Shapes and Implied Viscosities of Suspended Submicron Particles. *Atmos. Chem. Phys.*, **2015**, *15*, 7819-7829.

[66] Marcolli, C.; Luo, B.; Peter, T. Mixing of the Organic Aerosol Fractions: Liquids as the Thermodynamically Stable Phases. *J. Phys. Chem. A*, **2004**, *108*, 2216-2224.

[67] Angell, C. A. Formation of Glasses from Liquids and Biopolymers. *Science*, **1995**, *267*, 1924.

[68] Berthier, L.; Biroli, G. Theoretical Perspective on the Glass Transition and Amorphous Materials. *Rev. Mod. Phys.* **2011**, *83*, 587.

[69] Struik, L. C. E. Physical Aging in Plastics and other Glassy Materials. *Polym. Eng. Sci.* **1977**, *17*, 165-173.

[70] Angell, C. A. Insights into Phases of Liquid Water from Study of its Unusual Glass-Forming Properties. *Science* **2008** *319*, 582-587.

[71] Shiraiwa, M.; Ammann, M.; Koop, T.; Pöschl, U. Gas Uptake and Chemical Aging of Semisolid Organic Aerosol Particles. *Proc. Natl. Acad. Sci.* **2011**, *108*, 11003-11008.

[72] Zobrist, B.; Marcolli, C.; Pedernera, D. A.; Koop, T. Do Atmospheric Aerosols Form Glasses? *Atmos. Chem. Phys.* **2008**, *8*, 5221-5244.

[73] Berkemeier, T.; Shiraiwa, M.; Pöschl, U.; Koop, T. Competition Between Water Uptake and Ice Nucleation by Glassy Organic Aerosol Particles. *Atmos. Chem. Phys.* **2014**, *14*, 12513-12531.

[74] Kanakidou, M.; Seinfeld, J. H.; Pandis, S. N.; Barnes, I.; Dentener, F. J.; Facchini, M. C.; Dingenen, R. V.; Ervens, B.; Nenes, A. N.; Nielsen, C. J.; Swietlicki, E. Organic Aerosol and Global Climate Modelling: A Review. *Atmos. Chem. Phys.* **2005**, *5*, 1053-1123.

[75] Myhre, G.; Samset, B. H.; Schulz, M.; Balkanski, Y.; Bauer, S.; Berntsen, T. K.; Bian, H.; Bellouin, N.; Chin, M.; Diehl, T.; Easter, R. C. Radiative Forcing of the Direct Aerosol Effect from AeroCom Phase II Simulations. *Atmos. Chem. Phys.* **2013**, *13*, 1853.

[76] Baustian, K. J.; Wise, M. E.; Jensen, E. J.; Schill, G. P.; Freedman, M. A.; Tolbert, M. A. State Transformations and Ice Nucleation in Amorphous (Semi-) Solid Organic Aerosol. *Atmos. Chem. Phys.* **2013**, *13*, 5615.

[77] Murray, B. J.; Wilson, T. W.; Dobbie, S.; Cui, Z.; Al-Jumur, S. M.; Möhler, O.; Schnaiter, M.; Wagner, R.; Benz, S.; Niemand, M.; Saathoff, H. Heterogeneous Nucleation of Ice Particles on Glassy Aerosols Under Cirrus Conditions. *Nat. Geosci.* **2010**, *3*, 233-237.

[78] Wilson, T. W.; Murray, B. J.; Wagner, R.; Möhler, O.; Saathoff, H.; Schnaiter, M.; Skrotzki, J.; Price, H. C.; Malkin, T. L.; Dobbie, S.; Al-Jumur, S. M. R. K. Glassy Aerosols with a Range of Compositions Nucleate Ice Heterogeneously at Cirrus Temperatures. *Atmos. Chem. Phys.* **2012**, *12*, 8611-8632.

[79] Murray, B. J.; Haddrell, A. E.; Peppe, S.; Davies, J. F.; Reid, J. P.; O'Sullivan, D.; Price, H. C.; Kumar, R.; Saunders, R. W.; Plane, J. M. C.; Umo, N. S. Glass Formation and Unusual Hygroscopic Growth of Iodic Acid Solution Droplets with Relevance for Iodine Mediated Particle Formation in the Marine Boundary Layer. *Atmos. Chem. Phys.* **2012**, *12*, 8575-8587.

[80] Lienhard, D. M.; Huisman, A. J.; Bones, D. L.; Te, Y. F.; Luo, B. P.; Krieger, U. K.; Reid, J. P. Retrieving the Translational Diffusion Coefficient of Water from Experiments on Single Levitated Aerosol Droplets. *Phys. Chem. Chem. Phys.* **2014**, *16*, 16677-16683.

[81] Lienhard, D. M.; Huisman, A. J.; Krieger, U. K.; Rudich, Y.; Marcolli, C.; Luo, B. P.; Bones, D. L.; Reid, J. P.; Lambe, A. T.; Canagaratna, M. R.; et al. Viscous Organic Aerosol Particles in the Upper Troposphere: Diffusivity-Controlled Water Uptake and Ice Nucleation? *Atmos. Chem. Phys.* **2015**, *15*, 13599-13613.

[82] Corti, H. R.; Frank, G. A.; Marconi, M. C. Diffusion-Viscosity Decoupling in Supercooled Aqueous Trehalose Solutions. *J. Phys. Chem. B* **2008**, *112*, 12899-12906.

[83] Steimer, S. S.; Krieger, U. K.; Te, Y. F.; Lienhard, D. M.; Huisman, A. J.; Luo, B. P.; Ammann, M.; Peter, T. Electrodynamic Balance Measurements of Thermodynamic, Kinetic, and Optical Aerosol Properties Inaccessible to Bulk Methods. *Atmos. Meas. Tech.* **2015**, *8*, 2397-2408.

[84] Vaughn, B. S.; Tracey, P. J.; Trevitt, A. J. Laser-initiated Iodine Radical Chemistry in Single Microdroplets. *Chem. Phys. Lett.* **2012**, *551*, 134-138.

[85] Krieger, U. K.; Marcolli, C.; Reid, J. P. Exploring the Complexity of Aerosol Particle Properties and Processes using Single Particle Techniques. *Chem. Soc. Rev.* **2012**, *41*, 6631-6662.

[86] Preston, T. C.; Reid, J. P. Accurate and Efficient Determination of the Radius, Refractive Index, and Dispersion of Weakly Absorbing Spherical Particle using Whispering Gallery Modes. *J. Opt. Soc. Am. B* **2013**, *30*, 2113-2122.

[87] Cai, C.; Stewart, D. J.; Preston, T. C.; Walker, J. S.; Zhang, Y. H.; Reid, J. P. A New Approach to Determine Vapour Pressures and Hygroscopicities of Aqueous Aerosols Containing Semi-volatile Organic Compounds. *Phys. Chem. Chem. Phys.* **2014**, *16*, 3162-3172.

[88] Preston, T. C.; Reid, J. P. Determining the Size and Refractive Index of Microspheres using the Mode Assignments from Mie Resonances. *J. Opt. Soc. Am. A* **2015**, *32*, 2110-2117.

[89] Vaughn, B. S.; Tracey, P. J.; Trevitt, A. J. Drop-on-demand Microdroplet Generation: a Very Stable Platform for Single-droplet Experimentation. *RSC Adv.* **2016**, *6*, 60215-60222.

[90] Bones, D. L.; Reid, J. P.; Lienhard, D. M.; Krieger, U. K. Comparing the Mechanism of Water Condensation and Evaporation in Glassy Aerosol. *Proc. Natl. Acad. Sci.* **2012**, *109*, 11613-11618.

[91] Lu, J. W.; Rickards, A. M. J.; Walker, J. S.; Knox, K. J.; Miles, R. E. H.; Reid, J. P.; Signorell, S. Timescales of Water Transport in Viscous Aerosol: Measurements on Sub-Micron Particles and Dependence on Conditioning History. *Phys. Chem. Chem. Phys.* **2014**, *16*, 9819-9830.

[92] Rickards, A. M.; Song, Y. C.; Miles, R. E.; Preston, T. C.; Reid, J. P. Variabilities and Uncertainties in Characterising Water Transport Kinetics in Glassy and Ultraviscous Aerosol. *Phys. Chem. Chem. Phys.* **2015**, *17*, 10059-10073.

[93] Price, H. C.; Murray, B. J.; Mattsson, J.; O'Sullivan, D.; Wilson, T. W.; Baustian, K. J.; Benning, L. G. Quantifying Water Diffusion in High-Viscosity and Glassy Aqueous Solutions Using a Raman Isotope Tracer Method. *Atmos. Chem. Phys.* **2014**, *14*, 3817-3830.

[94] Price, H. C.; Mattsson, J.; Zhang, Y.; Bertram, A. K.; Davies, J. F.; Grayson, J. W.; Martin, S. T.; O'Sullivan, D.; Reid, J. P.; Rickards, A. M. J.; et al. Water Diffusion in Atmospherically Relevant α-Pinene Secondary Organic Material. *Chem. Sci.* **2015**, *6*, 4876-4883.

[95] Davies, J. F.; Wilson, K. R. Raman Spectroscopy of Isotopic Water Diffusion in Ultraviscous, Glassy, and Gel States in Aerosol by Use of Optical Tweezers. *Anal. Chem.* **2016**, *88*, 2361-2366.

[96] Smith, G. D.; Woods, E.; Baer, T.; Miller, R. E. Aerosol Uptake Described by Numerical Solution of the Diffusion-Reaction Equations in the Particle. *J. Phys. Chem. A* **2003**, *107*, 9582-9587.

[97] Shiraiwa, M.; Pfrang, C.; Pöschl, U.; Kinetic Multi-Layer Model of Aerosol Surface and Bulk Chemistry (KM-SUB): the Influence of Interfacial Transport and Bulk Diffusion on the Oxidation of Oleic Acid by Ozone. *Atmos. Chem. Phys.* **2010**, *10*, 3673-3691.

[98] Shiraiwa, M.; Pfrang, C.; Koop, T.; Pöschl, U. Kinetic Multi-Layer Model of Gas-Particle Interactions in Aerosols and Clouds (KM-GAP): Linking Condensation, Evaporation and Chemical Reactions of Organics, Oxidants and Water. *Atmos. Chem. Phys.* **2012**, *12*, 2777-2794.

[99] Berkemeier, T.; Steimer, S. S.; Krieger, U. K.; Peter, T.; Pschl, U.; Ammann, M.; Shiraiwa, M. Ozone Uptake on Glassy, Semi-Solid and Liquid Organic Matter and the Role of Reactive Oxygen Intermediates in Atmospheric Aerosol Chemistry. *Phys. Chem. Chem. Phys.* **2016**, *18*, 12662-12674.

[100] Moridnejad, A.; Preston, T. C. Models of Isotopic Water Diffusion in Spherical Aerosol Particles. *J. Phys. Chem. A* **2016**, *8*, 1251-1256.

[101] Stewart, D. J.; Cai, C.; Nayler, J.; Preston, T. C.; Reid, J. P.; Krieger, U. K.; Marcolli, C.; Zhang, Y. H. Liquid-Liquid Phase Separation in Mixed Organic/Inorganic Single Aqueous Aerosol Droplets. *J. Phys. Chem. A* **2015**, *119*, 4177-4190.

[102] Koop, T.; Bookhold, J.; Shiraiwa, M.; Pöschl, U. Glass Transition and Phase State of Organic Compounds: Dependency on Molecular Properties and Implications for Secondary Organic Aerosols in the Atmosphere. *Phys. Chem. Chem. Phys.* **2011**, *13*, 19238-19255.

[103] Schepanski, K.; Tegen, I.; Macke, A. Comparison of Satellite Based Observations of Saharan Dust Source Areas. *Remote Sens. Environ.* **2012**, *123*, 90-97.

[104] Xuan, J.; Sokolik, I. N.; Hao, J.; Guo, F.; Mao, H.; Yang, G. Identification and Characterization of Sources of Atmospheric Mineral Dust in East Asia. *Atmos. Environ.* **2004**, *38*, 6239-6252.

[105] Ginoux, P.; Garbuzov, D.; Hsu, N. C. Identification of Anthropogenic and Natural Dust Sources using Moderate Resolution Imaging Spectroradiometer (MODIS) Deep Blue Level 2 Data. *J. Geophys. Res. Atmos.* **2010**, *115*, D05204.

[106] Herman, J. R.; Bhartia, P. K.; Torres, O.; Hsu, C.; Seftor, C.; Celarier, E. Global Distribution of UVAbsorbing Aerosols from Nimbus 7/TOMS Data. *J. Geophys. Res. Atmos.* **1997**, 102(D14), 16911-16922.

[107] Prospero, J. M.; Ginoux, P.; Torres, O.; Nicholson, S. E.; Gill, T. E. Environmental Characterization of Global Sources of Atmospheric Soil Dust Identified with the Nimbus 7 Total Ozone Mapping Spectrometer (TOMS) Absorbing Aerosol Product. *Rev. Geophys.* **2002**, *40*, 1002.

[108] Torres, O.; Tanskanen, A.; Veihelmann, B.; Ahn, C.; Braak, R.; Bhartia, P. K.; Veefkind, P.; Levelt, P. Aerosols and Surface UV Products from Ozone Monitoring Instrument Observations: An Overview. *J. Geophys. Res. Atmos.* **2007**, *112*, D24S47.

[109] Schepanski, K.; Tegen, I.; Laurent, B.; Heinold, B.; Macke, A. A New Saharan Dust Source Activation Frequency Map Derived from MSG-SEVIRI IR-Channels. *Geophys. Res. Lett.* **2007**, *34*, L18803.

[110] Brooks, N.; Legrand, M. Dust Variability over Northern Africa and Rainfall in the Sahel, in *Linking Climate Change to Land Surface Change*, edited by S. J. McLaren and D. Kniveton, Kluwer Academic Publishers: Dordecht, The Netherlands, 2000, pp 1-25.

[111] Legrand, M.; Plana-Fattori, A.; and N'doume, C. Satellite Detection of Dust using the IR Imagery of Meteosat. I- Infrared Difference Dust Index. *J. Geophys. Res.* **2001**, *106*, 18251-18274.

[112] Walker, A. L.; Liu, M.; Miller, S. D.; Richardson, K. A; Westphal, D. L. Development of a Dust Source Database for Mesoscale Forecasting in Southwest Asia. *J. Geophys. Res. Atmos.* **2009**, *114*, D18207.

[113] Karimi, N.; Moridnejad, A.; Golian, S.; Samani; J. M. V., Karimi, D.; Javadi, S. Comparison of Dust Source Identification Techniques over Land in the Middle East Region using MODIS data. *Can. J. Remote Sens.* **2012**, *38*, 586-599.

[114] Shao, Y. *Physics and Modelling of Wind Erosion*, Atmospheric and Oceanographic Sciences Library Series, vol 37, Springer: Heidelberg, Germany, 2008.

[115] Bryson, R. A.; Baerreis, D. A. Possibilities of Major Climatic Modification and Their Implications: Northwest India, a Case for Study. *Bull. Am. Meteorol. Soc.* **1967**.

[116] Grigoryev, A. A.; Kondratyev, K. J. Atmospheric Dust Observed from Space. Part 2. *Wmo Bull.* **1981**, *30*, 3-9.

[117] Hamidi, M.; Kavianpour, M. R.; Shao, Y. Synoptic Analysis of Dust Storms in the Middle East. *Asia-Pac. J. Atmos. Sci.* **2013**, *49*, 279-286.

[118] Wilkerson W. D. Dust and Sand Forecasting in Iraq and Adjoining Countries, Tech. Rep., 62225-5008, Air Weather Service, Scott AFB (AWS/XTX), Illinois, USA, 1991.

[119] Kaufman, Y. J.; Tanré, D.; Remer, L. A.; Vermote, E. F.; Chu, A.; Holben, B. N. Operational Remote Sensing of Tropospheric Aerosol over Land from EOS Moderate Resolution Imaging Spectroradiometer. *J. Geophys. Res. Atmos.* **1997**, *102*, 17051-17067.

[120] Hsu, N. C.; Tsay, S. C.; King, M. D. Deep Blue Retrievals of Asian Aerosol Properties During ACE-Asia. *IEEE Trans. Geosci. Remote Sens.* **2006**, *44*, 3180-3195.

[121] Ackerman, S. A. Using the Radiative Temperature Difference at 3.7 and 11 mum to Tract Dust Outbreaks. *Remote Sens. Environ.* **1989**, *27*, 129-133.

[122] Miller, S. D. A Consolidated Technique for Enhancing Desert Dust Storms with MODIS. *Geophys. Res. Lett.* **2003**, *30*, 2071.

[123] Roskovensky, J. K.; Liou, K. N. Detection of Thin Cirrus from 1.38 mm/0.65 mm Reflectance Ratio Combined with 8.6_11 mm Brightness Temperature Difference. *Geophys. Res. Lett.* **2003**, *30*, 1985.

[124] Roskovensky, J. K.; Liou, K. N. Differentiating Airborne Dust from Cirrus Clouds using MODIS Data. *Geophys. Res. Lett.* **2005**, *32*, L12809.

[125] Darmenov, A.; Sokolik, I. N. Identifying the Regional ThermalIR Radiative Signature of Mineral Dust with MODIS. *Geophys. Res. Lett.* **2005**, *32*, L16803.

[126] Ginoux, P.; Torres, O. Empirical TOMS Index for Dust Aerosol: Application to Model Validation and Source Characterization. *J. Geophys. Res. Atmos.* **2003**, *108*, 4534.

[127] Mahowald, N. M.; Ballantine, J. A.; Feddema, J., Ramankutty, N. Global Trends in Visibility: Implications for Dust Sources. *Atmos. Chem. Phys.* **2007**, *7*, 3309-3339.

[128] Ginoux, P.; Prospero, J. M.; Gill, T. E.; Hsu, N. C.; Zhao, M. GlobalScale Attribution of Anthropogenic and Natural Dust Sources and Their Emission Rates Based on MODIS Deep Blue Aerosol Products. *Rev. Geophys.* **2012**, *50*, RG3005.

[129] Grini, A. Natural Aerosols in the Global Atmosphere, Ph.D. Dissertation, Department of Geoscience., University of Oslo, Norway, 2004.

[130] Mahowald, N.; Albani, S.; Kok, J. F.; Engelstaeder, S.; Scanza, R.; Ward, D. S.; Flanner, M. G. The Size Distribution of Desert Dust Aerosols and its Impact on the Earth System. *Aeolian Res.* **2014**, *15*, 53-71.

[131] Choobari, O. A.; Zawar-Reza, P.; Sturman, A. The Global Distribution of Mineral Dust and its Impacts on the Climate System: A Review. *Atmos. Res.* **2014**, *138*, 152-165.

[132] Sokolik, I. N.; Toon, O. B. Direct Radiative Forcing by Anthropogenic Airborne Mineral Aerosols. *Nature* **1996**, *381*, 681-683.

[133] Hansell, R. A.; Tsay, S. C.; Ji, Q.; Hsu, N. C.; Jeong, M. J.; Wang, S. H.; Reid, J. S.; Liou, K. N.; Ou, S. C. An Assessment of the Surface Longwave Direct Radiative Effect of Airborne Saharan Dust During the NAMMA Field Campaign. *J. Atmos. Sci.* **2010**, *67*, 1048-1065,

[134] Hansell, R. A.; Tsay, S. C.; Hsu, N. C.; Ji, Q.; Bell, S. W.; Holben, B. N.; Welton, E. J.; Roush, T. L.; Zhang, W.; Huang, J.; Li, Z. An Assessment of the Surface Longwave Direct Radiative Effect of Airborne Dust in Zhangye, China, during the Asian Monsoon Years Field Experiment (2008). *J. Geophys. Res.* **2012**, *117*, D00K39.

[135] Valenzuela, A.; Olmo, F. J.; Lyamani, H.; Antón, M.; Quirantes, A.; Alados-Arboledas, L. Aerosol Radiative Forcing During African Desert Dust Events (2005-2010) over Southeastern Spain. *Atmos. Chem. Phys.* **2012**, *12*, 10331-10351,

[136] Mahowald, N.; Kiehl, L. Mineral Aerosol and Cloud Interactions. *Geophys. Res. Lett.* **2003**, *30*, 1475.

[137] Ou, S. C.; Liou, K. N.; Hsu, N. C.; Tsay, S. C. Satellite Remote Sensing of Dust Aerosol Indirect Effects on Cloud Formation over Eastern Asia. *Int. J. Remote Sens.* **2012**, *33*, 7257-7272.

[138] Solomos, S.; Kallos, G.; Kushta, J.; Astitha, M.; Tremback, C.; Nenes, A.; Levin, Z. An Integrated Modeling Study on the Effects of Mineral Dust and Sea Salt Particles on Clouds and Precipitation. *Atmos. Chem. Phys.* **2011**, *11*, 873-892,

[139] Creamean, J. M.; Suski, K. J.; Rosenfeld, D.; Cazorla, A.; DeMott, P. J.; Sullivan, R. C.; White, A. B.; et al. Dust and Biological Aerosols from the Sahara and Asia Influence Precipitation in the Western US, *Science*, **2013**, *339*, 1572-1578.

[140] Jickells, T. D.; An, Z. S.; Andersen, K. K.; Baker, A. R.; Bergametti, G.; Brooks, N.; Cao, J. J.; Boyd, P. W.; Duce, R. A.; Hunter, K. A.; Kawahata, H. Global Iron Connections Between Desert Dust, Ocean Biogeochemistry, and Climate. *Science*, **2005**, *308*, 67-7.

[141] Mahowald, N. M.; Baker, A. R.; Bergametti, G.; Brooks, N.; Duce, R. A.; Jickells, T. D.; Kubilay, N.; Prospero, J. M.; Tegen, I. Atmospheric Global Dust Cycle and Iron Inputs to the Ocean. *Glob. Biogeochem. Cycles* **2005**, *19*, GB4025.

[142] Okin, G. S.; Mladenov, N.; Wang, L.; Cassel, D.; Caylor, K. K.; Ringrose, S.; Macko, S. A. Spatial Patterns of Soil Nutrients in two Southern African Savannas, *J. Geophys. Res.* **2008**, *113*, G02011.

[143] Painter, T. H.; Barrett, A. P.; Landry, C. C.; Neff, J. C.; Cassidy, M. P.; Lawrence, C. R.; McBride, K. E.; Farmer, G. L. Impact of Disturbed Desert Soils on Duration of Mountain Snow Cover. *Geophys. Res. Lett.* **2007**, *34*, L12502.

[144] Neff, J. C.; Ballantyne, A. P.; Farmer, G. L.; Mahowald, N. M.; Conroy, J. L.; Landry, C. C.; Overpeck, J. T.; Painter, T. H.; Lawrence, C. R.; Reynolds, R. L. Increasing Eolian Dust Deposition in the Western United States Linked to Human Activity, *Nature Geosci.* **2008**, *1*, 189-195.

[145] Griffin, D. W. Atmospheric Movement of Microorganisms in Clouds of Desert Dust and Implications for Human Health, *Clin. Microbiol. Rev.* **2007**, *20*, 459-477.

[146] Okin, G. S.; Parsons, A. J.; Wainwright, J.; Herrick, J. E.; Bestelmeyer, B. T.; Peters, D. C.; Fredrickson, E. L. Do Changes in Connectivity Explain Desertification? *BioScience*, **2009**, *59*, 237-244.

[147] Rashki, A.; Kaskaoutis, D. G.; Goudie, A. S.; Kahn, R. A. Dryness of Ephemeral Lakes and Consequences for Dust Activity: the Case of the Hamoun Drainage Basin, Southeastern Iran. *Sci. Total. Environ.* **2013**, *463*, 552-564,

[148] Okin, G. S.; Murray, B.; Schlesinger, W. H. Degradation of Sandy arid Shrubland Environments: Observations, Process modelling, and Management Implications, *J. Arid. Environ.* **2001**, *47*, 123-144.

[149] Okin, G. S.; Painter, T. H. Effect of Grain Size on Remotely Sensed Spectral Reflectance of Sandy Desert Surfaces. *Remote Sens. Environ.* **2004**, *89*, 272-280.

[150] Tegen, I.; Lacis, A. A. Modeling of Particle Size Distribution and its Influence on the Radiative Properties of Mineral Dust Aerosol. *J. Geophys. Res.* **1996**, *101*, 19237-19244

[151] Mahowald, N. M.; Kloster, S.; Engelstaedter, S.; Moore, J. K.; Mukhopadhyay, S.; McConnell, J. R.; Albani, S.; Doney, S. C.; Bhattacharya, A.; Curran, M. A. J.; Flanner, M. G.; Hoffman, F. M.; Lawrence, D. M.; Lindsay, K.; Mayewski, P. A.; Neff, J.; Rothenberg, D.; Thomas, E.; Thornton, P. E.; Zender, C. S. Observed 20th Century Desert Dust Variability: Impact on Climate and Biogeochemistry. *Atmos. Chem. Phys.* **2010**, *10*, 10875-10893,

[152] Mahowald, N. M.; Zender, C. S.; Luo, C.; Savoie, D.; Torres, O.; del Corral, J. Understanding the 30-year Barbados Desert Dust Record. *J. Geophys. Res.* **2002**, *107*, 4561.

[153] Luo, C., Mahowald, N., Corral, J. Sensitivity Study of Meteorological Parameters on Mineral Aerosol Mobilization, Transport and Distribution, *J. Geophys. Res.* **2003**, *108*, 4447.

[154] Tegen, I.; Werner, M.; Harrison, S. P.; Kohfeld, K. E. Relative Importance of Climate and Land Use in Determining Present and Future Global Soil Dust Emission. *Geophys. Res. Lett.* **2004**, *31*, L05105.

[155] Zender, C. S.; Bian, H.; Newman, D. Mineral Dust Entrainment and Deposition (DEAD) Model: Description and 1990s Dust Climatology. *J. Geophys. Res.* **2003**, *108*, 4416.

[156] Ginoux, P.; Prospero, J. M.; Torres, O.; Chin, M. Long-term Simulation of Global Dust Distribution with the GOCART Model: Correlation with North Atlantic Oscillation, *Environ. Model Soft.* **2004**, *19*, 113-128.

[157] UN Sand and Dust Storm Fact Sheet, 2013. http://reliefweb.int/report/iraq/sand-and-dust-storm-fact-sheet.

[158] Al-Ansari, N. A. Management of Water Resources in Iraq: Perspectives and Prognoses. *Engineering* **2013**, *5*, 667-684.

[159] Gibson, G. R. War and Agriculture: Three Decades of Agricultural Land Use and Land Cover Change in Iraq, Dissertation, Virginia Polytechnic Institute and State University, 2012.

[160] Sissakian, V.; Al-Ansari, N.; Knutsson, S. Sand and Dust Storm Events in Iraq. *Nat. Sci.* **2013**, *5*, 1084-1094.

[161] Idso, S. B. Dust Storms. *Sci. Am.* **1976**, *235*, 108-11, 113-14.

[162] Middleton, N. J. Dust Storms in the Middle East, *J. Arid. Environ.* **1986**, *10*, 83-96.

[163] Safar, M. I. Frequency of Dust in Day Time Summer in Kuwait, pp. 107- 119, Directorate of Civil Aviation, Meteorological Dept., Climatological Section, State of Kuwait, 1980.

[164] Tindale, N. W.; Pease, P. P., Aerosols over the Arabian Sea: Atmospheric Transport Pathways and Concentrations of Dust and Sea Salt, *Deep-Sea Res. II.* **1999**, *46*, 1577-1595,

[165] Prospero, J. M.; Carlson, T. N. Saharan Air Outbreaks over the Tropical North Atlantic, *Pure Appl. Geophys.* **1981**, *119*, 677-91.

[166] Tucker, C. J. Red and Photographic Infrared Linear Combinations for Monitoring Vegetation. *Remote. Sens. Environ.* **1979**, *8*, 127-150.

[167] Dawelbait M.; Morari F. Monitoring Desertification in a Savannah Region in Sudan using Landsat Images and Spectral Mixture Analysis, *J. Arid Environ.* **2012**, *80*, 45-55.

[168] Okin, G. S.; Robert, D. A. Remote Sensing in Arid Regions: Challenges and Opportunities. In: Ustin, S. L. (Ed.), *Remote Sensing for Natural Resources Management and Environmental Monitoring*, third ed; Hoboken, New Jersey, pp 111-145, 2004.

[169] Tompkins, S.; Mustard, J. F.; Pieters, C. M.; Forsyth, D. W. Optimization of Endmembers for Spectral Mixture Analysis. *Remote. Sens. Environ.* **1997**, *59*, 472-489.

[170] Elmore, A. J.; Mustard, J. F.; Manning, S. J.; Lobell, D. B. Quantifying Vegetation Change in Semiarid Environments. *Remote. Sens. Environ.* **2000**, *73*, 87-102,

[171] Bateson, C. A.; Curtiss, B. A Method for Manual Endmember Selection and Spectral Unmixing. *Remote. Sens. Environ.* **1996**, *55*, 229-243.

[172] Bateson, C. A.; Asner, G. P.; Wessman, C. A. Endmember Bundles: A New approach to Incorporating Endmember Variability into Spectral Mixture Analysis. *IEEE Trans. Geosci. Remote Sens.* **2000**, *38*, 1083-1094.

[173] Asner, G. P. Biophysical Remote Sensing Signatures of Arid and Semiarid Ecosystem. In: Ustin, S.L. (Ed.), *Remote Sensing for Natural Resources Management and Environmental Monitoring*, third ed.; Hoboken, New Jersey, pp 53-109, 2004.

[174] Richardson, C. J.; Reiss, P.; Hussain, N. A.; Alwash, A. J.; Pool, D. J. The Restoration Potential of the Mesopotamian Marshes of Iraq. *Science* **2005**, *307*, 1307-1311.

[175] Twomey, S. Pollution and the Planetary Albedo. *Atmos. Environ. (1967).* **1974**, *8*, 1251-1256.

[176] Chand, D.; Wood, R.; Anderson, T. L.; Satheesh, S. K.; Charlson, R. J. Satellite-Derived Direct Radiative Effect of Aerosols Dependent on Cloud Cover. *Nat. Geosci.* **2009**, *2*, 181-184.

[177] Kaufman, Y. J.; Tanr, D.; Boucher, O. A. Satellite View of Aerosols in the Climate System. *Nature* **2002**, *419*, 215-223.

[178] Ramanathan, V. C.; Crutzen, P. J.; Kiehl, J. T.; Rosenfeld, D. Aerosols, Climate, and the Hydrological Cycle. *Science* **2001**, 294, 2119-2124.

[179] Aiken, A. C.; Decarlo, P. F.; Kroll, J. H.; Worsnop, D. R.; Huffman, J. A.; Docherty, K. S.; Ulbrich, I. M.; Mohr, C.; Kimmel, J. R.; Sueper, D; et al. O/C and OM/OC Ratios of Primary, Secondary, and Ambient Organic Aerosols with High-Resolution Time-of-Flight Aerosol Mass Spectrometry. *Environ. Sci. Technol.* **2008**, *42*, 4478-4485.

[180] Volkamer, R.; Jimenez, J. L.; San Martini, F.; Dzepina, K.; Zhang, Q.; Salcedo, D.; Molina, L. T.; Worsnop, D. R.; Molina, M. J.; Secondary Organic Aerosol Formation from Anthropogenic Air Pollution: Rapid and Higher than Expected. *Geophys. Res. Lett.* **2006**, *33*, L17811.

[181] Ng, N. L.; Canagaratna, M. R.; Zhang, Q.; Jimenez, J. L.; Tian, J.; Ulbrich, I. M.; Kroll, J. H.; Docherty, K. S.; Chhabra, P. S.; Bahreini, R.; et al. Organic Aerosol Components Observed in Northern Hemispheric Datasets from Aerosol Mass Spectrometry. *Atmos. Chem. Phys.* **2010**, 10, 4625-4641.

[182] Lin, G.; Penner, J. E.; Zhou, C. How Will SOA Change in the Future? *Geophys. Res. Lett.* **2016**, *43*, 1718-1726.

[183] Fry, J. L.; Draper, D. C.; Barsanti, K. C.; Smith, J. N.; Ortega, J.; Winkler, P. M.; Lawler, M. J.; Brown, S. S.; Edwards, P. M.; Cohen, R. C.; et al. Secondary Organic Aerosol Formation and Organic Nitrate Yield From NO_3 Oxidation of Biogenic Hydrocarbons. *Environ. Sci. Technol.* **2014**, *48*, 11944-11953.

[184] Zhang, X.; McVay, R. C.; Huang, D. D.; Dalleska, N. F.; Aumont, B.; Flagan, R. C.; Seinfeld, J. H. Formation and Evolution of Molecular Products in α-Pinene Secondary Organic Aerosol. *Proc. Natl. Acad. Sci.* **2015**, *112*, 14168-14173.

[185] Glasius, M.; Goldstein, A. H. Recent Discoveries and Future Challenges in Atmospheric Organic Chemistry. *Environ. Sci. Technol.* **2016**, *50*, 2754-2764.

[186] Hodzic, A.; Kasibhatla, P. S.; Jo, D. S.; Cappa, C.; Jimenez, J. L.; Madronich, S.; Park, R. J. Rethinking the Global Secondary Organic Aerosol (SOA) Budget: Stronger Production, Faster Removal, Shorter Lifetime. *Atmos. Chem. Phys. Discuss.* **2016**, *16*, 7917-7941.

[187] Beardsley, R. L.; Jang, M. Simulating the SOA Formation of Isoprene from Partitioning and Aerosol Phase Reactions in the Presence of Inorganics. *Atmos. Chem. Phys.* **2016**, *16*, 5993-6009.

[188] Marais, E. A.; Jacob, D. J.; Jimenez, J. L.; Campuzano-Jost, P.; Day, D. A.; Hu, W.; Krechmer, J.; Zhu, L.; Kim, P. S.; Miller, C. C.; et al. Aqueous-Phase Mechanism for Secondary Organic Aerosol Formation from Isoprene: Application to the Southeast United States and Co-Benefit of SO_2 Emission Controls. *Atmos. Chem. Phys.* **2016**, *16*, 1603-1618.

[189] Zhao, Y.; Wingen, L. M.; Perraud, V.; Finlayson-Pitts, B. J. Phase, Composition, and Growth Mechanism for Secondary Organic Aerosol from the Ozonolysis of α-Cedrene. *Atmos. Chem. Phys.* **2016**, *16*, 3245-3264.

[190] Vaden, T. D.; Imre, D.; Beránek, J. Evaporation Kinetics and Phase of Laboratory and Ambient Secondary Organic Aerosol. *Proc. Natl. Acad. Sci.* **2011**, *108*, 2190-2195.

[191] Shiraiwa, M.; Seinfeld, J. H. Equilibration Timescale of Atmospheric Secondary Organic Aerosol Partitioning. *Geophys. Res. Lett.* **2012**, *39*, L24801.

[192] Virtanen, A.; Joutsensaari, J.; Koop, T.; Kannosto, J.; Yli-Pirilä, P.; Leskinen, J.; Mäkelä, J. M.; Holopainen, J. K.; Pschl, U.; Kulmala, M.; et al. An Amorphous Solid State of Biogenic Secondary Organic Aerosol Particles. *Nature* **2010**, *467*, 824-827.

[193] Debenedetti, P. G.; Stillinger, F. H. Supercooled Liquids and the Glass Transition. *Nature* **2001**, *410*, 259-267.

[194] Pajunoja, A.; Malila, J.; Hao, L.; Joutsensaari, J. Estimating the Viscosity Range of SOA Particles Based on Their Coalescence Time. *Aerosol Sci. Technol.*, **2014**, *48*, i-iv.

[195] Lienhard, D. M.; Bones, D. L.; Zuend, A.; Krieger, U. K.; Reid, J. P.; Peter, T. Measurements of Thermodynamic and Optical Properties of Selected Aqueous Organic and Organic-Inorganic Mixtures of Atmospheric Relevance. *J. Phys. Chem. A* **2012**, *116*, 9954-9968.

[196] Alfrey, T.; Gurnee, E. F.; Lloyd, W. G. Diffusion in glassy polymers. *J. Polym. Sci., Part C: Polym. Symp.* **1966**, *12*, 249-261.

[197] Astaluta, G.; Sarti, G. C. A class of mathematical models for sorption of swelling solvents in glassy polymers. *Polym. Eng. Sci.* **1978**, *18*, 388-395.

[198] Thomas, N. L.; Windle, A. H. A theory of case II diffusion. *Polymer* **1982**, *23*, 529-542.

[199] Hui, C. Y.; Wu, K. C.; Lasky, R. C.; Kramer, E. J. CaseII diffusion in polymers. II. Steadystate front motion. *J. Appl. Phys.* **1987**, *61*, 5137-5149.

[200] Lee, P. I.; Kim, C. J. Effect of geometry on solvent front penetration in glassy polymers. *J. Membr. Sci.* **1992**, *65*, 77-92.

[201] Wu, J. C.; Peppas, N. A. Modeling of penetrant diffusion in glassy polymers with an integral sorption Deborah number. *J. Polym. Sci., Part B: Polym. Phys.* **1993**, *31*, 1503-1518.

[202] Edwards, D. A.; Cohen, D. S. A mathematical model for a dissolving polymer. *AIChE J.*, **1995**, *41*, 2345-2355.

[203] Hallquist, M.; Wenger, J. C.; Baltensperger, U.; Rudich, Y.; Simpson, D.; Claeys, M.; Dommen, J.; Donahue, N. M.; George, C.; Goldstein A. H.; and Hamilton, J. F. The formation, properties and impact of secondary organic aerosol: current and emerging issues. *Atmos. Chem. Phys.* **2009**, *9*, 5155-5236.

[204] Shiraiwa, M.; Li, Y.; Tsimpidi, A. P.; Karydis, V. A.; Berkemeier, T.; Pandis, S. N.; Lelieveld, J.; Koop, T.; Pöschl, U. Global distribution of particle phase state in atmospheric secondary organic aerosols. *Nat. Commun.* **2017**, *8*, 1-7. http://doi.org/10.1038/ncomms15002

[205] Dette, H. P.; Koop, T. Glass formation processes in mixed inorganic/organic aerosol particles. *J. Phys. Chem. A* **2014,** *119*, 4552-4561.

[206] Preston, T. C., Davies, J. F., Wilson, K. R. The frequency-dependent response of single aerosol particles to vapour phase oscillations and its application in measuring diffusion coefficients. *Phys. Chem. Chem. Phys.* **2017**, *19*, 3922-3931.

[207] Järvinen, E.; Ignatius, K.; Nichman, L.; Kristensen, T. B.; Fuchs, C.; Hoyle, C. R.; Höppel, N.; Corbin, J. C.; Craven, J.; Duplissy, J.; and Ehrhart, S. Observation of viscosity transition in α-pinene secondary organic aerosol. *Atmos. Chem. Phys.* **2016**, *16*, 4423-4438.

[208] Vaden, T. D.; Song, C.; Zaveri, R. A.; Imre, D.; Zelenyuk, A. Morphology of mixed primary and secondary organic particles and the adsorption of spectator organic gases during aerosol formation. *Proc. Natl. Acad. Sci. U.S.A.*, **2010**, *107*, 6658-6663.

[209] Steimer, S. S.; Berkemeier, T.; Gilgen, A.; Krieger, U. K.; Peter, T.; Shiraiwa, M.; Ammann, M. Shikimic acid ozonolysis kinetics of the transition from liquid aqueous solution to highly viscous glass. *Phys. Chem. Chem. Phys.* **2015**, *17*, 31101-31109.

[210] Bohren, C. F.; Huffman, D. R. Absorption and scattering by a sphere. In *Absorption and Scattering of Light by Small Particles*, John Wiley & Sons, 1983, pp. 100-101.

[211] Lam, C. C.; Leung, P. T.; Young, K. Explicit asymptotic formulas for the positions, widths, and strengths of resonances in Mie scattering. *J. Opt. Soc. Am. B* **1992**, *9*, 1585-1592.

[212] Aden, A. L. Electromagnetic scattering from spheres with sizes comparable to the wavelength. *J. Appl. Phys.* **1951**, *22*, 601-605.

[213] Teraoka, I.; Arnold, S. Theory of resonance shifts in TE and TM whispering gallery modes by nonradial perturbations for sensing applications. *J. Opt. Soc. Am. B* **2006**, *23*, 1381-1389.

[214] Foreman, M. R.; Vollmer, F. Optical tracking of anomalous diffusion kinetics in polymer microspheres. *Phys. Rev. Lett.* **2015**, *114*, 118001.

[215] Bhandari, R. Scattering coefficients for a multilayered sphere: analytic expressions and algorithms. *Appl. Opt.* **1985**, *24*, 1960-1967.

[216] Wu, Z. S., and Wang, Y. P. Electromagnetic scattering for multilayered sphere: recursive algorithms. *Radio Sci.* **1991**, *26*, 1393-1401.

[217] Wu, Z. S., Guo, L. X., Ren, K. F., Gouesbet, G., and Grhan, G. Improved algorithm for electromagnetic scattering of plane waves and shaped beams by multilayered spheres. *Appl. Opt.*, **1997**, *36*, 5188-5198.

[218] Yang, W. Improved recursive algorithm for light scattering by a multilayered sphere. *Appl. Opt.* **2003**, *42*, 1710-1720.

[219] Peña, O.; Pal, U. Scattering of electromagnetic radiation by a multilayered sphere. *Comput. Phys. Commun.* **2009**, *180*, 2348-2354.

[220] Chýlek, P. Partial-wave resonances and the ripple structure in the Mie normalized extinction cross section. *J. Opt. Soc. Am.* **1976**, *66*, 285-287.

[221] Tong, H. J.; Reid, J. P.; Bones, D. L.; Luo, B. P.; Krieger, U. K. Measurements of the timescales for the mass transfer of water in glassy aerosol at low relative humidity and ambient temperature. *Atmos. Chem. Phys.* **2011**, *11*, 4739-4754.

[222] Tammann, G. H. W. Z.; Hesse, W. Die Abhängigkeit der Viscosität von der Temperatur bie unterkühlten Flssigkeiten. *Z. Anorg. Allg. Chem.*, **1926**, *156*, 245-257.

[223] Fulcher, G. S. Analysis of recent measurements of the viscosity of glasses. *J. Am. Ceram. Soc.* **1925**, *8*, 339-355.

[224] Scherer, G. W. Editorial comments on a paper by Gordon S. Fulcher. *J. Am. Ceram. Soc.* **1992**, *75*, 1060-1062.

[225] Lide, D. R. CRC *Handbook of Chemistry and Physics*, 79th ed.; CRC: Boca Raton, FL, 1998.

[226] International Organization of Legal Metrology, Refractometers for the measurement of the sugar content of fruit juices, International Recommendation OIML R 108 1993; Available from: `https://www.oiml.org/en/files/pdf_r/r108-e93.pdf/view`

[227] Pankow, J. F.; Marks, M. C.; Barsanti, K. C.; Mahmud, A.; Asher, W. E.; Li, J.; Ying, Q.; Jathar, S. H.; Kleeman, M. J. Molecular view modeling of atmospheric organic particulate matter: Incorporating molecular structure and co-condensation of water. *Atmos. Environ.* **2015**, *122*, 400-408.

[228] Hodas, N.; Zuend, A.; Mui, W.; Flagan, R. C.; and Seinfeld, J. H. Influence of particle-phase state on the hygroscopic behavior of mixed organicinorganic aerosols. *Atmos. Chem. Phys.* **2015,** *15*, 5027-5045.

[229] Vignes, A. Diffusion in Binary Solutions. Variation of Diffusion Coefficient with Composition. *Ind. Eng. Chem. Fund.* **1966**, *5*, 189-199.

[230] Smith, R. S.; Kay, B. D. The Existence of Supercooled Liquid Water at 150 K. *Nature* **1999**, *398*, 788-791.

[231] McGlashan, M. L. Deviations from Raoult's Law. *J. Chem. Educ.* **1963** *40*, 516.

[232] Fick, A. V. On liquid diffusion. *London Edinburgh Dublin Philos. Mag. J. Sci.*, **1855**, *10*, 30-39.

[233] Crank, John. *The mathematics of diffusion.* Oxford university press, **1979**, pp. 89.

[234] Hall, W. D., and Pruppacher, H. R. The survival of ice particles falling from cirrus clouds in subsaturated air. *J. Atmos. Sci.*, **1976**, *33*, 1995-2006.

Appendix A

Derivation of Diffusion Equation for Water Exchange Experiment

In Chapter 4, we presented analytical solution to the diffusion problem involving both constant and equilibrium boundary conditions. Here, the mathematical physics and the derivation of equilibrium solution is presented. The solution to the constant concentration on the surface is not presented as the methodology would be the same and more straightforward.

A.1 Problem Statement

Governing equations:

$$\frac{\partial c(r,t)}{\partial t} = \frac{D}{r^2}\frac{\partial}{\partial r}\left(r^2\frac{\partial c(r,t)}{\partial r}\right) \qquad \text{for} \qquad 0 < r < a, \quad t > 0, \tag{A.1}$$

$$\frac{\partial}{\partial r}\left(r^2\frac{\partial c_g(r,t)}{\partial r}\right) = 0 \qquad \text{for} \qquad a < r < \infty, \quad t > 0, \tag{A.2}$$

subject to the boundary conditions:

conservation of mass,

$$D\frac{\partial c}{\partial r} = D_g\frac{\partial c_g}{\partial r} \quad \text{at} \quad r = a, \quad t > 0, \tag{A.3}$$

symmetry,

$$\frac{\partial c}{\partial r} = 0 \quad \text{at} \quad r = 0, \quad t > 0, \tag{A.4}$$

equilibrium assumption,

$$c = kc_g \quad \text{at} \quad r = a, \quad t > 0, \quad \text{where} \quad k = RT(c_w + c_s)/(\gamma p_0) \tag{A.5}$$

the fixed RH at $r = \infty$,

$$c_g = c_\infty \quad \text{as} \quad r \to \infty, \quad t > 0, \tag{A.6}$$

and initial condition

$$c(r, 0) = c_0. \tag{A.7}$$

A.2 Changing Variables

In order to solve the problem, the following changing variable is needed:

$$U = rc \;\Rightarrow\; c = \frac{U}{r} \quad \text{and} \quad \frac{\partial c}{\partial r} = \frac{1}{r}\frac{\partial U}{\partial r} - \frac{U}{r^2}$$

Now, we can rewrite the governing equations and boundary conditions: Governing equations:

$$\frac{\partial U(r,t)}{\partial t} = D\frac{\partial^2 U(r,t)}{\partial r^2} \qquad \text{for} \qquad 0 < r < a, \quad t > 0, \tag{A.8}$$

$$\frac{\partial^2 (rc_g)}{\partial r^2} = 0 \qquad \text{for} \qquad a < r < \infty, \quad t > 0, \tag{A.9}$$

subject to the boundary conditions:

conservation of mass,

$$\frac{D}{a}\left(\frac{\partial U}{\partial r} - \frac{U}{a}\right) = D_g\frac{\partial c_g}{\partial r} \quad \text{at} \quad r = a, \quad t > 0, \tag{A.10}$$

symmetry,

$$U = 0 \quad \text{at} \quad r = 0, \quad t > 0, \tag{A.11}$$

equilibrium assumption,

$$\frac{U}{a} = kc_g \quad \text{at} \quad r = a, \quad t > 0, \tag{A.12}$$

the fixed RH at $r = \infty$,

$$c_g = c_\infty \quad \text{as} \quad r \to \infty, \quad t > 0, \tag{A.13}$$

and initial condition

$$U(r, 0) = rc_0. \tag{A.14}$$

A.3 Solving for Gas Phase Concentration

It is easier to start solving c_g first:

$$\frac{\partial^2(rc_g)}{\partial r^2} = 0 \Rightarrow \frac{\partial}{\partial r}\left(\frac{\partial(rc_g)}{\partial r}\right) = \frac{\partial}{\partial r}\left(c_g + r\frac{\partial c_g}{\partial r}\right) = \frac{\partial c_g}{\partial r} + \frac{\partial}{\partial r}\left(r\frac{\partial c_g}{\partial r}\right) = 2\frac{\partial c_g}{\partial r} + r\frac{\partial^2 c_g}{\partial r^2} = 0$$

Then, the following expression is derived for c_g:

$$c_g = -\frac{c_1}{r} + c_2 \tag{A.15}$$

where c_1 and c_2 are the coefficients in the solution equation. Applying the boundary conditions, it is found:

$$c_1 = ac_\infty - \frac{U}{k} \tag{A.16}$$

$$c_2 = c_\infty \tag{A.17}$$

Now mass continuity boundary condition becomes:

$$\frac{D}{a}\left(\frac{\partial U}{\partial r} - \frac{U}{a}\right) = \frac{D_g}{a^2}\left(ac_\infty - \frac{U}{k}\right) \quad \text{at} \quad r = a, \quad t > 0, \tag{A.18}$$

By doing more simplification, we obtain the following non-homogeneous boundary condition:

$$-\beta U + a\frac{\partial U}{\partial r} = \frac{aD_g c_\infty}{D} \quad \text{at} \quad r = a, \quad t > 0, \tag{A.19}$$

where $\beta = 1 - \alpha$ and $\alpha = D_g/(Dk)$.

A.4 Solving for Condense Phase Concentration

Let's rewrite the problem. The governing equation in liquid phase is:

$$\frac{\partial U(r,t)}{\partial t} = D\frac{\partial^2 U(r,t)}{\partial r^2} \quad \text{for} \quad 0 < r < a, \quad t > 0, \tag{A.20}$$

and the boundary conditions are

symmetry,

$$U = 0 \quad \text{at} \quad r = 0, \quad t > 0, \tag{A.21}$$

conservation of mass,

$$-\beta U + a\frac{\partial U}{\partial r} = \frac{aD_g c_\infty}{D} \quad \text{at} \quad r = a, \quad t > 0, \tag{A.22}$$

and initial condition is

$$U(r,0) = rc_0. \tag{A.23}$$

This problem involves a linear partial differential equation (PDE) with a non-homogeneous boundary condition. To solve this, we can assume:

$$U(r,t) = S(r,t) + V(r,t) \tag{A.24}$$

where $S(r,t)$ is the steady state part of the solution (one will remain for large time) and it satisfies non-homogeneous boundary condition of U(r,t). $V(r,t)$ is the part of the solution that depends on the initial condition and will eventually go to zero. In fact, $V(r,t)$ is a new initial boundary value problem with homogeneous boundary condition. The $S(r,t)$ is given by:

$$S(r,t) = A(t) + \frac{B(t) - A(t)}{a}r \tag{A.25}$$

where $A(t)$ and $B(t)$ are found by requiring that $S(r,t)$ satisfies boundary conditions. When $S(r,t)$ satifies boundary conditions, the new problem will surely have homogeneous boundary conditions. We test that here:

$$U(0,t) = S(0,t) + V(0,t) \tag{A.26}$$

$$U(a,t) = S(a,t) + V(a,t) \tag{A.27}$$

if $S(r,t)$ satisfies the non-homogeneous boundary conditions, then $V(0,t) = 0$. Now we can go ahead and find $A(t)$ and $B(t)$. $S(r,t)$ has to satisfy the boundary conditions, then:

$$S(0,t) = A(t) = 0 \tag{A.28}$$

and

$$-\beta S + a\frac{\partial S}{\partial r} = \frac{aD_g c_\infty}{D} \quad \text{at} \quad r = a, \quad t > 0, \tag{A.29}$$

It is also known that:

$$\frac{\partial S}{\partial r} = \frac{B(t) - A(t)}{a} \tag{A.30}$$

After simplification, $B(t) = aD_g c_\infty/(\alpha D)$. Then $S(r,t)$ becomes:

$$S(r,t) = \frac{B(t)}{a} r = \frac{D_g c_\infty}{\alpha D} r \tag{A.31}$$

and

$$U(r,t) = S(r,t) + V(r,t) = \frac{D_g c_\infty}{\alpha D} r + V(r,t) \tag{A.32}$$

To find the solution for $V(r,t)$, we need to build its PDE and boundary conditions. Using the above equation all derivative are found:

$$\frac{\partial U(r,t)}{\partial t} = \frac{\partial}{\partial t}\left(\frac{D_g c_\infty}{\alpha D} r + V(r,t)\right) = \frac{\partial V(r,t)}{\partial t} \tag{A.33}$$

$$\frac{\partial U(r,t)}{\partial r} = \frac{\partial}{\partial r}\left(\frac{D_g c_\infty}{\alpha D} r + V(r,t)\right) = \frac{D_g c_\infty}{\alpha D} + \frac{\partial V(r,t)}{\partial r} \tag{A.34}$$

$$\frac{\partial^2 U(r,t)}{\partial r^2} = \frac{\partial}{\partial r}\left(\frac{D_g c_\infty}{\alpha D} + \frac{\partial V(r,t)}{\partial r}\right) = \frac{\partial^2 V(r,t)}{\partial r^2} \tag{A.35}$$

Now the new PDE is:

$$\frac{\partial V(r,t)}{\partial t} = D\frac{\partial^2 V(r,t)}{\partial r^2} \tag{A.36}$$

subject to boundary conditions

$$V(0,t) = 0 \tag{A.37}$$

$$\frac{\partial V(r,t)}{\partial r} - \frac{\beta}{a}V(r,t) = 0 \tag{A.38}$$

and initial condition

$$V(r,0) = rc_0 - S(r,0) \tag{A.39}$$

to solve this PDE, we use method of separation of variables:

$$V(r,t) = R(r)\Gamma(t) \tag{A.40}$$

We now substitute equation into PDE equation and introduce a separation constant:

$$\frac{1}{R(r)}\frac{\partial^2 R(r)}{\partial r^2} = \frac{1}{D\Gamma(t)}\frac{\partial \Gamma(t)}{\partial t} = -\lambda^2 \tag{A.41}$$

This will produce two ordinary differential equations:

$$\frac{\partial^2 R(r)}{\partial r^2} + \lambda^2 R(r) = 0 \tag{A.42}$$

$$\frac{\partial \Gamma(t)}{\partial t} + D\lambda^2\Gamma(t) = 0 \tag{A.43}$$

Solving these equations yield

$$V(r,t) = c_3 e^{-D\lambda_n^2 t}(c_4 \cos\lambda_n r + c_5 \sin\lambda_n r) \tag{A.44}$$

where c_3, c_4, and c_5 are solution constants. Applying boundary conditions and raarranging again yield to the following transcendental eigenvalue λ_n equation:

$$\lambda_n \cot\lambda_n = \beta \quad \rightarrow \quad \lambda_n \quad \text{for } n = 1, 2, 3, ... \tag{A.45}$$

We introduce a new constant $B_n = c_3c_5$, to produce a solution of the original PDE of the form:

$$V_n(r,t) = B_n e^{-D\lambda_n^2 t} \sin \lambda_n r \tag{A.46}$$

Now we build the most general solution by adding all solutions together:

$$V(r,t) = \sum_{n=1}^{\infty} B_n e^{-D\lambda_n^2 t} \sin \lambda_n r \tag{A.47}$$

To define B_n, we need to apply nonhomogeneous initial condition. It yeilds

$$rc_0 - S(r,0) = \sum_{n=1}^{\infty} B_n \sin \lambda_n r \tag{A.48}$$

which is a Fourier since series expansion of $[rc_0 - S(r,0)]$ in terms of an orthogonal function over the interval of $0 \le r \le a$. Therefore, the coefficients are obtained through solving the equation below:

$$B_n = \frac{2}{a} \int_0^a (rc_0 - S(r,0)) \sin \lambda_n r \; dr \tag{A.49}$$

The Fourier coefficients are then

$$B_n = \frac{(\lambda_n^2 + \beta^2) \sin \lambda_n}{\lambda_n^2(\lambda_n^2 + \beta(\beta - 1))} \tag{A.50}$$

Combining all pieces together, the solution to the system will become:

$$c(r,t) = c_\infty k + \frac{2a}{r}(c_\infty k - c_0)(\beta - 1) \sum_{n=1}^{\infty} B_n \sin \frac{\lambda_n r}{a} \, e^{-D\lambda_n^2 t/a^2}. \tag{A.51}$$

The total sorption is yielded by integration the concentration equation inside the particle:

$$Q_e(t) = \frac{4\pi a^3}{3} c_\infty k - 8\pi a^3 (c_\infty k - c_0)(\beta - 1)^2 \sum_{n=1}^{\infty} \frac{B_n}{\lambda_n^2} \sin \lambda_n \, e^{-D\lambda_n^2 t/a^2}. \tag{A.52}$$

Appendix B

Parameterization of Binary Particles

In Chapter 4, diffusion lifetime of aqueous citric acid was calculated using the parameters presented by Refs. 80 and 195. For aqueous shikimic acid, parameters were obtained from the Ref. 83.

In all these studies, an empirical Vignes-type equation[229] was used to fit the measured diffusion coefficients of water to a wide range of concentration at different temperature:

$$D_{\mathrm{H_2O}} = \left(D^{\circ}_{\mathrm{H_2O}}\right)^{x_w \alpha} \left(D^{\circ}_{\mathrm{acid}}\right)^{1-x_w \alpha} \tag{B.1}$$

where x_w is the mole fraction of water, α is the correction parameter (activity coefficient), $D^{\circ}_{\mathrm{H_2O}}$ and $D^{\circ}_{\mathrm{acid}}$ are the diffusion coefficients of water in pure water and pure acid, respectively. The temperature dependance of these two coefficient is included using the VFT type equations. Data from Smith and Kay[230] is used to establish VFT relation for $D^{\circ}_{\mathrm{H_2O}}$:

$$\log_{10}\left(D^{\circ}_{\mathrm{H_2O}}\right) = -6.514 - \frac{387.4}{T - 118}. \tag{B.2}$$

B.1 Aqueous Citric Acid

For aqueous citric acid, $D^{\circ}_{\mathrm{acid}}$ is formulated as follows:[80]

$$\log_{10}\left(D^{\circ}_{\text{citric acid}}\right) = -15 - \frac{175}{T - 208}. \tag{B.3}$$

The expression for the activity coefficient becomes:[231]

$$\ln\alpha = (1 - x_w)^2[C + 3D - 4D(1 - x_w)], \tag{B.4}$$

where C and D are functions of temperature:

$$C = -41 + 0.143T, \tag{B.5}$$

$$D = -69 + 0.28T, \tag{B.6}$$

with $C(T > 265) = C(265)$ and $D(T > 255) = D(255)$.[80]

B.2 Aqueous Shikimic Acid

For aqueous shikimic acid, D°_{acid} is expressed as follows:[83]

$$\log_{10}\left(D^{\circ}_{\text{shikimic acid}}\right) = -9.35 - \frac{542.8}{T - 211}. \tag{B.7}$$

The expression for the activity coefficient becomes:[231]

$$\ln\alpha = (1 - x_w)^2[C + 3D - 4D(1 - x_w)], \tag{B.8}$$

where C and D are functions of temperature:

$$C = -6.55 + 0.025T, \tag{B.9}$$

$$D = 7.122 - 0.0261T, \tag{B.10}$$

with $C(T > 258K) = C(T = 258K)$ and $D(T > 273K) = D(T = 273K)$.[83]

Appendix C

Derivation of Core-shell Resonance Equation

C.1 Introducing Riccati-Bessel Functions

To start, it is convenient to introduce Riccati-Bessel functions:

$$\psi_n(\rho) = \rho \times j_n(\rho), \quad \chi_n(\rho) = -\rho \times y_n(\rho), \quad \xi_n(\rho) = \rho \times h_n^{(1)}(\rho)$$

where ρ is an arbitrary variable, j_n and y_n and $h_n^{(1)}$ are the spherical Bessel functions of first, second, and third kind respectively. $h_n^{(1)}$ is sometimes called spherical Hankel function.

C.2 Equations of Scattering Coefficient

For two concentric spheres of radii a and b with refractive indices of m_1 and m_2 and complex size parameters of z_1 and z_2, the Mie-Lorenz scattering coefficients (a_n, b_n) can be expressed using the following equations:[40]

$$a_n = \frac{\psi_n(z_2)[\psi_n'(m_2 z_2) - A_n \chi_n'(m_2 z_2)] - m_2 \psi_n'(z_2)[\psi_n(m_2 z_2) - A_n \chi_n(m_2 z_2)]}{\xi_n(z_2)[\psi_n'(m_2 z_2) - A_n \chi_n'(m_2 z_2)] - m_2 \xi_n'(z_2)[\psi_n(m_2 z_2) - A_n \chi_n(m_2 z_2)]} \tag{C.1}$$

$$b_n = \frac{m_2 \psi_n(z_2)[\psi_n'(m_2 z_2) - B_n \chi_n'(m_2 z_2)] - \psi_n'(z_2)[\psi_n(m_2 z_2) - B_n \chi_n(m_2 z_2)]}{m_2 \xi_n(z_2)[\psi_n'(m_2 z_2) - B_n \chi_n'(m_2 z_2)] - \xi_n'(z_2)[\psi_n(m_2 z_2) - B_n \chi_n(m_2 z_2)]} \tag{C.2}$$

where

$$A_n = \frac{m_2\psi_n(m_2z_1)\psi_n'(m_1z_1) - m_1\psi_n'(m_2z_1)\psi_n(m_1z_1)}{m_2\chi_n(m_2z_1)\psi_n'(m_1z_1) - m_1\chi_n'(m_2z_1)\psi_n(m_1z_1)} \tag{C.3}$$

$$B_n = \frac{m_2\psi_n(m_1z_1)\psi_n'(m_2z_1) - m_1\psi_n(m_2z_1)\psi_n'(m_1z_1)}{m_2\chi_n'(m_2z_1)\psi_n(m_1z_1) - m_1\psi_n'(m_1z_1)\chi_n(m_2z_1)} \tag{C.4}$$

C.3 Solving for Concentric Spheres

In order to normal mode dominate the scattered field, a particular frequency or radius needs to be found such that the denominators of a_n and b_n be very small. In other words, the following conditions need to be satisfied:

$$\xi_n(z_2)[\psi_n'(m_2z_2) - A_n\chi_n'(m_2z_2)] = m_2\xi_n'(z_2)[\psi_n(m_2z_2) - A_n\chi_n(m_2z_2)] \tag{C.5}$$

$$m_2\xi_n(z_2)[\psi_n'(m_2z_2) - B_n\chi_n'(m_2z_2)] = \xi_n'(z_2)[\psi_n(m_2z_2) - B_n\chi_n(m_2z_2)] \tag{C.6}$$

Expanding these two conditions will give the following long expression;

for a_n, it is:

$$h_n^{(1)}(z_2)\Bigg(- j_n(m_2z_2) - m_2z_2j_n'(m_2z_2) - \frac{\Big(y_n(m_2z_2) + m_2z_2y_n'(m_2z_2)\Big)N_{a_n}}{D_{a_n}}\Bigg) = m_2^2\Big(h_n^{(1)}(z_2) + z_2h_n^{(1)'}(z_2)\Big)\Bigg(j_n(m_2z_2) - \frac{y_n(m_2z_2)N_{a_n}}{D_{a_n}}\Bigg) \tag{C.7}$$

where

$$N_{a_n} = (m_2^2 - m_1^2)j_n(m_1z_1)j_n(m_2z_1) - m_1^2m_2z_1j_n(m_1z_1)j_n'(m_2z_1) + m_1m_2^2z_1j_n(m_2z_1)j_n'(m_1z_1) \tag{C.8}$$

$$D_{a_n} = (m_2^2 - m_1^2)j_n(m_1z_1)y_n(m_2z_1) - m_1^2m_2z_1j_n(m_1z_1)y_n'(m_2z_1) + m_1m_2^2z_1y_n(m_2z_1)j_n'(m_1z_1) \tag{C.9}$$

for b_n, the expression becomes:

$$\begin{aligned} h_n^{(1)}(z_2)\Big(- j_n(m_2z_2) - m_2z_2j_n'(m_2z_2) - \frac{\Big(y_n(m_2z_2) + m_2z_2y_n'(m_2z_2)\Big)N_{b_n}}{D_{b_n}}\Big) &= \\ \Big(h_n^{(1)}(z_2) + z_2h_n^{(1)'}(z_2)\Big)\Big(j_n(m_2z_2) - \frac{y_n(m_2z_2)N_{b_n}}{D_{b_n}}\Big) & \end{aligned} \tag{C.10}$$

where

$$N_{b_n} = 0 - m_1m_2^2z_1j_n(m_1z_1)j_n'(m_2z_1) + m_1^2m_2z_1j_n(m_2z_1)j_n'(m_1z_1) \tag{C.11}$$

$$D_{b_n} = 0 - m_1m_2^2z_1j_n(m_1z_1)y_n'(m_2z_1) + m_1^2m_2z_1y_n(m_2z_1)j_n'(m_1z_1). \tag{C.12}$$

By doing further simplifications and then rearranging the expressions again, we can get:

$$\frac{m_2^2\Big(1 + z_2h_n^{(1)'}(z_2)/h_n^{(1)}(z_2)\Big) + m_2z_2j_n'(m_2z_2)/j_n(m_2z_2) + 1}{y_n(m_2z_2)\Big[m_2^2\Big(1 + z_2h_n^{(1)'}(z_2)/h_n^{(1)}(z_2)\Big) - 1\Big] - m_2z_2y_n'(m_2z_2)} = \frac{N_{a_n}}{j_n(m_2z_2)D_{a_n}} \tag{C.13}$$

$$\frac{\Big(1 + z_2h_n^{(1)'}(z_2)/h_n^{(1)}(z_2)\Big) + m_2z_2j_n'(m_2z_2)/j_n(m_2z_2) + 1}{y_n(m_2z_2)\Big[\Big(1 + z_2h_n^{(1)'}(z_2)/h_n^{(1)}(z_2)\Big) - 1\Big] - m_2z_2y_n'(m_2z_2)} = \frac{N_{b_n}}{j_n(m_2z_2)D_{b_n}} \tag{C.14}$$

By combining two above eqautions, we can introduce a single expression for the resonance condition of the core-shell particle:

$$\begin{aligned} \frac{j_n(m_2z_1)\left(1 + m_1z_1j_n'(m_1z_1)/j_n(m_1z_1)\right) - q\left(j_n(m_2z_1) + m_2z_1j_n'(m_2z_1)\right)}{y_n(m_2z_1)\left(1 + m_1z_1j_n'(m_1z_1)/j_n(m_1z_1)\right) - q\left(y_n(m_2z_1) + m_2z_1y_n'(m_2z_1)\right)} &= \\ \frac{j_n(m_2z_2)\left(1 + z_2h_n^{(1)\prime}(z_2)/h_n^{(1)}(z_2)\right) - v\left(j_n(m_2z_2) + m_2z_2j_n'(m_2z_2)\right)}{y_n(m_2z_2)\left(1 + z_2h_n^{(1)\prime}(z_2)/h_n^{(1)}(z_2)\right) - v\left(y_n(m_2z_2) + m_2z_2y_n'(m_2z_2)\right)}&, \end{aligned} \tag{C.15}$$

where $q = 1$, $v = 1$ for a_n, and $q = m_1^2/m_2^2$, $v = 1/m_2^2$ for b_n.

Appendix D

Numerical Scheme for Mass Transport

D.1 Governing Equations

Fick's laws of diffusion[232] describe the water mass transport from/into a single particle. Using these laws, the fundamental diffusion equation in spherical coordinate system is derived.[233] Considering spherical symmetry, diffusion equation becomes

$$\frac{\partial n(r,t)}{\partial t} = \frac{1}{r^2}\frac{\partial}{\partial r}\left(r^2 D(n)\frac{\partial n(r,t)}{\partial r}\right), \tag{D.1}$$

where n is the number concentration of water, $D(n)$ is the concentration dependent of diffusion coefficient, r is radial coordinate and t is time. This equation is also assumes that the diffusion flux,

$$\vec{F_r} = -D(n)\frac{\partial n(r,t)}{\partial r}, \tag{D.2}$$

goes from region of high concentration to region of low concentration.

D.2 Finite Volume Scheme

Eq. D.1 is nonlinear in nature and the associated diffusion problem involves two nonlinear boundary conditions: (i) a moving boundary as the radius of the particle changes during water sorption and desorption and (ii) a nonlinear boundary condition at the liquid-vapor interface. There is likely no analytical solution to this boundary value problem and numerical evaluation is required.[100] Hence, most measurements in water sorption/desorption experiments have been modeled using the finite difference method outlined by Zobrist et al.[15]

To quantify the concentration of water during wetting or drying, the numerical scheme breaks the droplet into many concentric spherical shells. The amount of exchanged water between shells is then computed by calculating the number concentration of water for the shells, averaging weight fraction to calculate the diffusion coefficient of water between shells, and using the shell thickness. Fig. D.1 shows the coordinates used for the numerical differentiation. As depicted in this figure, the net number of water molecules crossing shell i in time interval Δt is defined as the difference in the concentration fluxes just on the left and the right sides of shell i.

The numerical differentiation of Eq. D.2 will be the concentration flux of water f_i into shell i:

$$f_{i-1/2} = 4\pi r_i^2 \left(-D_{i-1/2} \nabla n_i\right)$$

and the numerical differentiation of the number concentration gradient is

$$\nabla n_i = \frac{n_i - n_{i-1}}{r_{i+1/2} - r_{i-1/2}}.$$

where n_i and n_{i-1} are the number concentration of water molecules in shells i and $i-1$. The first shell ($i = 1$) is considered a core (i.e. shell thickness is zero) so there is no flux to a lower shell.

Since

$$r_{i+1/2} - r_{i-1/2} = \frac{r_{i+1} + r_i}{2} - \frac{r_i + r_{i-1}}{2},$$

and

$$d_i = r_{i+1} - r_i = \left(\frac{3V_i}{4\pi} + r_i^3\right)^{1/3} - r_i,$$

$$d_{i-1} = r_i - r_{i-1} = \left(\frac{3V_{i-1}}{4\pi} + r_{i-1}^3\right)^{1/3} - r_{i-1},$$

V_i is volume of shell i and the gradient can be re-written as

$$\nabla n_i = \frac{n_i - n_{i-1}}{\frac{1}{2}(d_i + d_{i-1})}.$$

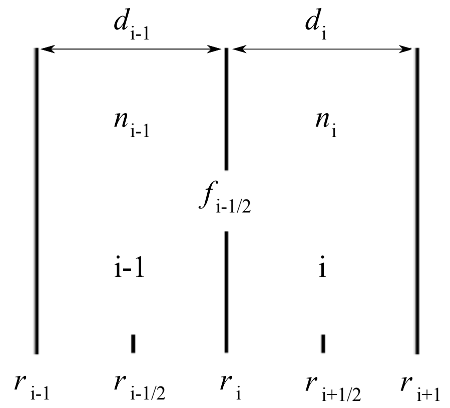

Figure D.1: Coordinates used for numerical differentiation.

Using these expressions, the flux between shells i and $i-1$ is then

$$f_{i-1/2} = -8\pi r_i^2 D_{i-1/2} \frac{n_i - n_{i-1}}{d_i + d_{i+1}}. \tag{D.3}$$

In this model, the number concentration of water and density of the aqueous sucrose solution are found using the water activity parameterization presented by Zobrist et al.[72].

To set the concentration gradient in the liquid phase, the very last shell on the surface of particle (called outermost shell) is always assumed to be in equilibrium with the surrounding vapor phase. Therefore, the water sorption/desorption of outermost shell, $f_{ns+1/2}$, is calculated based on the governing diffusion equation in the vapor phase:[2]

$$f_{ns+1/2} = 4\pi r D_g \frac{(a_w - \mathrm{RH}) p_w^{sat}}{k_B T} \tag{D.4}$$

where D_g is the vapor phase diffusion coefficient, a_w is the water activity, RH is the relative humidity, p_w^{sat} is the saturation vapor pressure of pure water, k_B is the Stefan-Boltzmann constant, T is the temperature, and ns is the index of outermost shell. The diffusivity of water vapor in air is calculated using Eqn. (13) in Hall and Pruppacher, 1976.[234] Under equilibrium assumption, p_w^{sat} is obtained using the temperature dependent expressions in Seinfeld and Pandis, 2005[4] when $T > 273K$ and in Zobrist et al. 2011 when $T < 273K$. $f_{ns+1/2}$ is also called Maxwellian flux and is derived from Eqn. D.1 based on the assumption that concentration profile in the vapor phase reaches its steady state value at larger time.[4] Note that D_g is not a function of concentration.

In this numerical model, Δt is chosen based on the maximum allowed change in the number of water molecules. To have a stable and time-efficient numerical scheme, this threshold is found to be less than 0.02.[15] To reach this goal, the number of water molecules in each shell for each time step is compared to the number of water molecules in each shell of the previous time step. Then, if the fractional change in number of water molecules, $(f_{i-1/2} - f_{i+1/2})\Delta t$, is larger than the threshold (Δt is too big), the water content is reset to the previous value and Δt is adjusted by a factor that helps to optimize the computation. Therefore, Δt is dynamic during the simulations. Care should be taken when using this scheme for RH value very close to either zero or one.

Mass convection is taken into account by changing the volume of shell each time in the model during the diffusion process. This will justify the absence of convection term in Eq. D.1.[100] At first, the model divides the particle into 1000 shells with the same shell thickness. All the essential diffusion parameters including the shell volume are then calculated for each shell based on the initial conditions. Taking the first time step, the scheme recalculates the shell thicknesses based on the new shell volumes. The shell thickness adjustment continues to the last time step and overall radius of particle is obtained by adding up all the new thicknesses to the initial radius. In addition, this model assumes that the accommodation coefficient of water vapor on the aqueous sucrose droplet during the diffusion process is one for the temperatures of interest.[15]